

Retrieval of Optical and Microphysical Cloud Properties Using Ship-based Spectral Solar Radiation Measurements over the Atlantic Ocean

Von der Fakultät für Physik und Geowissenschaften

der Universität Leipzig

genehmigte

DISSERTATION

zur Erlangung des akademischen Grades

Doktor der Naturwissenschaften

Dr. rer. nat.

vorgelegt

von Dipl.-Met. Marlen Brückner

geboren am 05.07.1985 in Schlema / Sachsen

Gutachter: Prof. Dr. Manfred Wendisch
Prof. Dr. Susanne Crewell

Tag der Verleihung: 31. März 2015

Bibliographische Beschreibung:

Brückner, Marlen

Retrieval of Optical and Microphysical Cloud Properties Using Ship-based Spectral Solar Radiation Measurements over the Atlantic Ocean

Universität Leipzig, Dissertation

133 S., 180 Lit., 66 Abb., 17 Tab.

Referat:

In der vorliegenden Arbeit werden abwärtsgerichtete spektrale Strahldichten analysiert, die mithilfe schiffsgebundener Beobachtungen über dem Atlantischen Ozean gemessen wurden. In Verbindung mit hochauflösenden Lidar und Mikrowellenradiometer Fernerkundungsverfahren werden optische und mikrophysikalische Wolkeneigenschaften aus spektralen Daten abgeleitet. Um Probleme bereits existierender Verfahren, die auf Transmissionen basieren, zu beseitigen, wird ein neuer Fernerkundungsalgorithmus vorgestellt, der nicht nur Zweideutigkeiten in der Bestimmung der Parameter umgeht, sondern auch den Einfluss von Messunsicherheiten verringert. Die Methode vergleicht gemessene spektrale Transmissionsverhältnisse bei sechs Wellenlängen mit modellierten Verhältnissen. Die neue Fernerkundungsmethode ist schnell und exakt, sodass sie für operative Zwecke geeignet ist. Sie wird für homogene und inhomogene Wasserwolken als auch für Cirren angewendet. Die Ergebnisse des neuen Ableitungsverfahrens werden mit Beobachtungen des Flüssigwasserpfades eines Mikrowellenradiometers verglichen. Daraus ergibt sich eine Überschätzung des Flüssigwasserpfades unter dicken Wolken, jedoch eine leichte Unterschätzung für dünne Wolken. Eine statistische Analyse der abgeleiteten Wolkeneigenschaften aus drei Atlantiküberfahrten wird vorgestellt. In den mittleren Breiten und nördlichen Subtropen wurden ähnliche Charakterisierungen von Wolkeneigenschaften gefunden, jedoch lässt die Variabilität der meridionalen Verteilung in den restlichen Regionen darauf schließen, dass der Einfluss von Wettersystemen auf typische Wolkenverteilungen überwiegt. Mit etwa 63% aller Daten stellen homogene Stratocumulus Wolken den vorherrschenden Wolkentyp über dem Ozean dar, während durchbrochene und inhomogene Bewölkung jeweils mit 16% und 21% vertreten sind. Durch den Einfluss von 3D Strahlungseffekten weisen alle analysierten Verteilungen von Wolkeneigenschaften eine erhöhte Anzahl an niedrigen Werten auf. Entlang eines Fahrtabschnittes zeigt der Vergleich zwischen Satelliten- und bodengebundenen Verfahren vergleichbare Ergebnisse für die optische Dicke von Wolken mit Einschränkungen für dicke Wasserwolken. Die meridionale Verteilung des effektiven Tropfenradius stimmt innerhalb der Unsicherheiten beider Methoden überein, jedoch sind die Mittelwerte vom Satelliten höher als die vom Boden aus bestimmten Werte.

Bibliographic Description:

Brückner, Marlen

Retrieval of Optical and Microphysical Cloud Properties Using Ship-based Spectral Solar Radiation Measurements over the Atlantic Ocean

Universität Leipzig, Dissertation

133 pp., 180 bilbiog., 66 fig., 17 tab.

Abstract:

In this thesis spectral solar zenith radiances are analyzed which were obtained from ship-based measurements over the Atlantic ocean. In combination with high-resolution lidar and microwave remote sensing optical and microphysical cloud properties were retrieved using spectral radiation data. To overcome problems of existing transmissivity-based cloud retrievals, a new retrieval algorithm is introduced which circumvents retrieval ambiguities and reduces the influence of measurement uncertainties. The method matches radiation measurements of ratios of spectral transmissivity at six wavelengths with modeled transmissivities. The new retrieval method is fast and accurate, and thus suitable for operational purposes. It is applied to homogeneous and inhomogeneous liquid water and cirrus clouds. The results from the new algorithm are compared to observations of liquid water path obtained from a microwave radiometer, yielding an overestimation for thick liquid water clouds but a slight underestimation for thin clouds. A statistical analysis of retrieved cloud properties during three Atlantic transects is introduced. Similar characteristics of cloud properties are found in the mid latitudes and northern subtropics but the large variability of meridional distribution in the remaining regions imply the prevailing influence of weather systems compared to typical cloud distributions. With about 63% homogeneous stratocumulus clouds are found to be the prevailing cloud type over ocean, while scattered and inhomogeneous liquid water clouds amount to 16% and 21%, respectively. All analyzed distributions are affected by an increased frequency of small values of cloud properties caused by 3D radiative effects. The comparison with satellite-based and ship-based cloud retrievals along the cruise track show comparable results for the cloud optical thickness with limitations for thick liquid water clouds. The meridional distribution of effective radius agreed within the uncertainties of both methods, however, the satellite-derived values are biased toward larger mean values.

Contents

1	Introduction	1
1.1	Marine Clouds	1
1.2	Radiative Cloud Effects	2
1.3	Remote Sensing of Clouds	5
1.4	Objectives	6
2	Definitions	8
2.1	Radiative Quantities	8
2.2	Optical Properties of Clouds	10
2.2.1	Individual Cloud Particles	10
2.2.2	Volumetric Properties of Clouds	14
2.3	Microphysical Properties of Clouds	15
2.4	Radiative Transfer Equation	16
3	Experimental	17
3.1	Atlantic Transfers on RV <i>Polarstern</i>	17
3.2	CORAS	21
3.2.1	Radiometric Calibration	23
3.2.2	Measurement Uncertainties	27
3.2.3	Horizontal Misalignment	28
3.3	Instrumentation of the OCEANET-Container	31
4	Remote Sensing and Multi-Wavelength Cloud Retrieval	36
4.1	Simulations	36
4.1.1	Radiative Transfer Model	36
4.1.2	Zenith Radiance	38
4.1.3	Transmissivity	39
4.2	Existing Transmissivity-Based Cloud Retrievals	41
4.2.1	Standard Two-Wavelength Retrieval	41
4.2.2	Spectral Slope Method	42
4.3	A New Multi-Wavelength Cloud Retrieval Method	45
4.3.1	Multi-Wavelength Approach	45
4.3.2	Retrieval Uncertainties	49
5	Case Studies	52
5.1	Liquid Water Clouds	53
5.1.1	Homogeneous Cloud Case	53

5.1.2	Inhomogeneous Cloud Case	55
5.1.3	Scattered Cloud Case	56
5.2	Cirrus	59
5.3	Comparison of Slope and Multi-Wavelength Method	64
5.4	Uncertainty Discussion	65
6	Statistical Cloud Analysis	68
6.1	Liquid Water Clouds	68
6.1.1	Meridional Distribution of Cloud Properties	68
6.1.2	Cloud Classification	71
6.1.3	Histograms of Cloud Properties	73
6.2	Cirrus Clouds	79
6.3	Comparison with Satellite Measurements	81
7	Summary, Conclusions and Outlook	87
7.1	Summary and Conclusions	87
7.1.1	Improved Multi-Wavelength Cloud Retrieval	88
7.1.2	Distributions of Cloud Properties	90
7.2	Outlook	92
A	Meridional Distributions of Cloud Properties	94
B	Histograms of Cloud Properties	99
	Bibliography	103
	List of Symbols	117
	List of Abbreviations	121
	List of Figures	123
	List of Tables	125
	Acknowledgements	127
	Curriculum Vitae	129

1 Introduction

Although clouds have been studied for several decades, they are still contributing to major uncertainties in estimating the Earth’s energy budget (Stocker et al., 2013). To infer macro- and microphysical properties from satellite, airborne or ground-based observation a multitude of cloud retrievals have been developed. The cloud properties vary for different cloud types and on temporal and spatial scales. Beside global observations of clouds from satellite measurements over the ocean, in contrast to land, ground-based observations of optical and microphysical cloud parameters are relatively sparse. The general objective of this work is to contribute to the improvement of retrieval techniques of marine cloud properties from ground-based observations in different climate zones. The presented data were collected over the Atlantic ocean and benefit from a combination of different active and passive remote sensing instruments with a high temporal and spatial resolution as compared to satellite observations to obtain optical and microphysical properties of marine clouds. This introduction, which is partly published by Brückner et al. (2014), gives a brief overview of marine clouds and their radiative effects on the Earth’s energy budget. The challenges in the remote sensing of optical and microphysical properties of clouds over the ocean are summarized. This chapter is concluded by presenting the main objectives of this work.

1.1 Marine Clouds

Diverse marine cloud regimes represent diverse meteorological environments and are organized by large-scale circulations. In Figure 1.1 a schematic meridional cross section of prevalent cloud regimes over the ocean is illustrated. In the tropics with intense solar radiation precipitating cumulonimbus develops over the warmer ocean (see Figure 1.1a). Those convective clouds with extensive cirrus anvils are associated with ascending air motions in the Intertropical Convergence Zone (ITCZ). From the tops of those thunderstorms, the air flows toward higher latitudes and often forms thin cirrus clouds. In the warm subsiding regions in the subtropics (around 30°N and 30°S) over the colder oceans shallow stratocumulus forms under a strong inversion. Within the surface trade winds to the equator typical shallow cumulus clouds are seen captured underneath the trade wind inversion. The schematic cross section from mid-latitudes to high latitudes in Figure 1.1b illustrates a typical extratropical cyclone system. In the warm sector turbulence-driven boundary layer stratus clouds evolve followed by a region of nimbostratus clouds on the frontal zone between cool polar air and the warm subtropical air. In the upper-tropospheric frontal outflow multiple layer clouds consisting of higher cirrus and mid-level altostratus occurs.

In Figure 1.2 the annual distribution of cloud amount over the ocean is illustrated. Averaged lidar profiles of *Calipso* (Winker et al., 2003) merged with data from *CloudSat* (Stephens et al.,

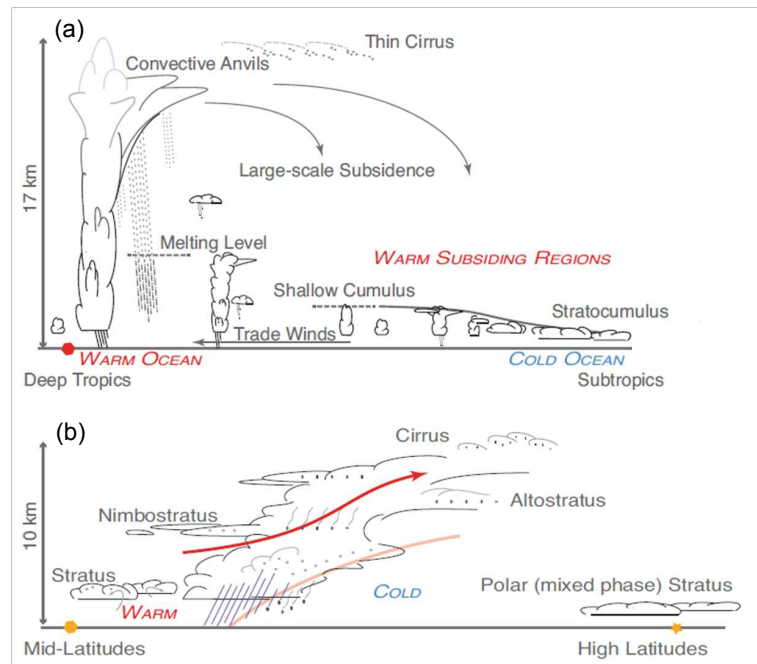


Figure 1.1: Schematic meridional cross section of cloud regimes over the ocean for (a) the tropics and subtropics and (b) for mid-latitudes and high latitudes. Graphic is adopted from Boucher et al. (2013).

2002) over a period from 2006–2011 are shown. Low-level marine stratocumulus clouds (Figure 1.2a) with a global mean amount of about 43% occur primarily along the the west coast of continents in the subsiding regions, while high clouds with a global mean amount of about 36% (Figure 1.2b) are located primarily in the tropics and the mid-latitudes (Christensen et al., 2013). The arid subtropics are characterized by fewer clouds (Figure 1.2c). The remaining cloud regimes consist of deep convective clouds or multi-layer clouds (Figure 1.2d).

Over the oceans, clouds are involved in the latent heat exchange between air and sea as well as in the moisture transport between ocean and land (Fowler and Randall, 1994). Due to condensation, precipitation and evaporation processes latent heat and fresh water are transported by clouds which determines the stability of marine boundary layer as well as the vegetation over land (Trenberth et al., 2011).

1.2 Radiative Cloud Effects

With a coverage of roughly two thirds of the globe clouds are an important component of the Earth’s radiation budget. They influence the radiative energy budget by scattering and absorption of solar radiation (dominant in the wavelength region $0.2 - 5 \mu\text{m}$) and emission and absorption of terrestrial radiation (dominant in $\lambda = 5 - 100 \mu\text{m}$) in the atmosphere. On average, globally and annually, clouds tend to cool the climate system (Wielicki et al., 1995) because the solar cooling due to the cloud albedo effect (by approximately -50 Wm^{-2}) dominates the greenhouse warming (by approximately $+30 \text{ Wm}^{-2}$) in the terrestrial spectral

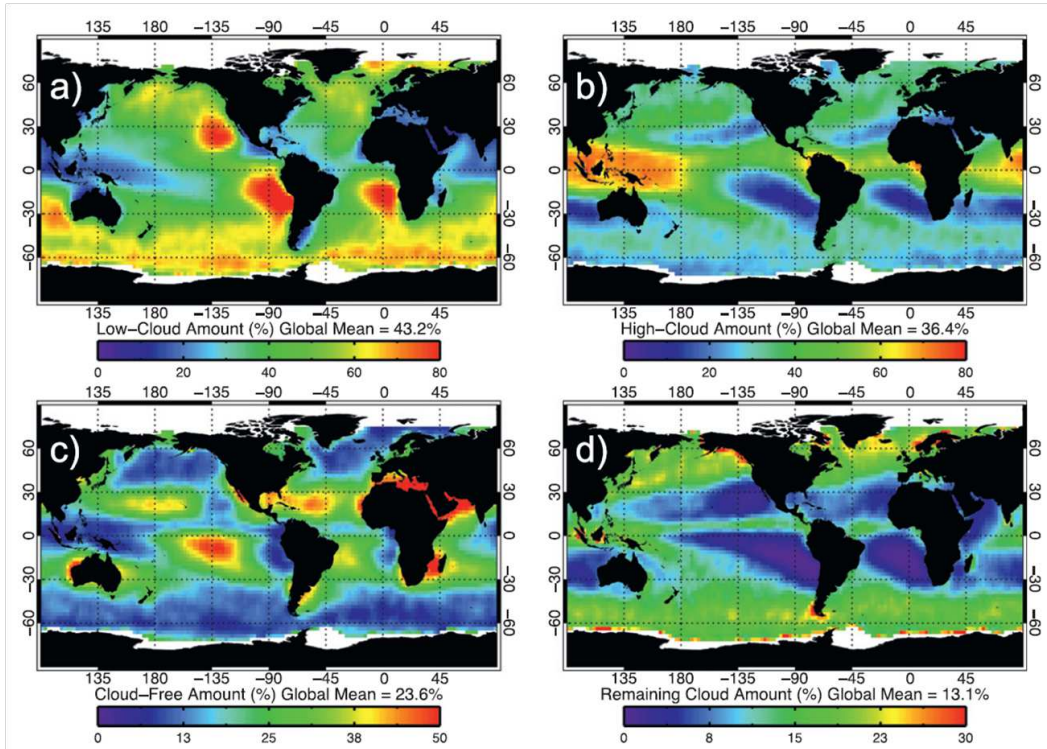


Figure 1.2: Annual global distribution of (a) low-level clouds below 3 km, (b) high clouds above 4 km, (c) cloud-free, and (d) remaining clouds including optically thick clouds and profiles of more than two cloud layers. Lidar profiles from *Calipso* were binned in $2.5^\circ \times 2.5^\circ$ areas and merged with *CloudSat* observations and averaged over a time period spanning from 2006–2011. Graphic is adopted from Christensen et al. (2013).

region with an uncertainty of less than 10% (Loeb et al., 2009). However, the variability of cloud properties among and in between diverse cloud types (vertical extent, thermodynamic phase, optical thickness and droplet size) is high. Depending on those properties they may effect both solar and terrestrial radiant flux densities (called irradiances) as much as changes in total cloud cover (Chen et al., 2000). On an annual average, the reflection of incoming solar radiation by clouds over the extratropical oceans exceeds the absorption of upwelling terrestrial radiation and thus strongly contributes to the net cooling effect of clouds on the Earth’s radiation budget (Harrison et al., 1990). In the terminology of the Earth Radiation Budget Experiment (ERBE) the cloud radiative forcing (CRF) at the top of the atmosphere (TOA) can be obtained from satellite data by comparing upwelling solar and terrestrial radiation in non-cloudy and cloudy conditions by $CRF = C_s + C_t$ (Ramanathan et al., 1989). According to these definitions, the solar cloud forcing C_s is generally negative because clouds reduce the amount of solar radiation, while the terrestrial cloud forcing C_t is generally positive because clouds increase the amount of terrestrial radiation. Harrison et al. (1990) found a clear difference in the seasonal warming of clouds over the Northern Hemisphere (NH) extratropical oceans. This means that the magnitude of net CRF , and particularly the individual components of C_s and C_t , is affected in a way that relatively small percentage changes in cloud properties and cloud cover result in abnormal climate forcing of several Wm^{-2} , comparable to the direct forcing due to a doubling of CO_2 (e.g., Ramanathan et al., 1995). Thus, over

the ocean with the associated relatively low surface albedo, it is important to quantify the physical mechanisms that affect CRF in these regions (Weaver and Ramanathan, 1997).

The annually averaged mean CRF at the TOA is strongly linked to the altitude –dependent cloud distribution. Regional patterns of C_t are dominated by high clouds. Cirrus clouds absorb more radiation emitted from the lower atmosphere and surface than they emit or reflect back to space. Depending on the microphysical and optical properties of ice clouds, the combined solar and terrestrial cloud forcing of high clouds may either warm or cool the atmosphere below these clouds (Stephens et al., 1990; McFarquhar et al., 2002). In contrast, regional patterns of C_s are sensitive to optically thick clouds at all altitudes. Particularly, thick low–level clouds, such as stratocumulus (Sc), cool the surface because the reflection of solar radiation dominates the emission of terrestrial radiation to the surface. These clouds are most common and energetically most important over the North Atlantic extratropical ocean and are characterized by geometrical thickness and cloud top heights less than 3 km (Hartmann et al., 1992; Mace, 2010). The reflectivity and transmissivity of low–level clouds in the marine boundary layer (MBL) is very sensitive to their liquid water content and microphysical parameters (Taylor and Ghan, 1992). Their development and life time is characterized by turbulent mixing due to strong infrared radiative and evaporative cooling near the cloud top (Christensen et al., 2013). The amount of the radiative cooling and entrainment can be affected by several factors. Various studies (e.g., Comstock et al., 2005; Caldwell and Bretherton, 2009; Wood, 2012) investigate the linking between properties of Sc and changes in net radiation due to the diurnal cycle. Generally, Sc thickness and amount are largest in the morning and decrease in the afternoon as absorption of solar radiation through upper cloud regions increases. Other studies focus on the influence of aerosols (Chen et al., 2011), wind shear (Wang et al., 2012), and overlying layers of aerosols (Wilcox, 2010) or cirrus clouds (Christensen et al., 2013) on radiative effects of Sc clouds. However, the simulation of MBL clouds, which are highly sensitive to changing environmental conditions, is currently the main sources of uncertainty of cloud feedbacks in general circulation models (Bony and Dufresne, 2005).

Numerous studies quantified the radiative effects of ice clouds from satellite and ground–based observations and numerical models (e.g., Liou, 1986; Lynch et al., 2002; Yang et al., 2007; Baran, 2012). However, ice clouds still remain one of the main source of uncertainty component in the atmospheric system. Beside the cloud altitude (temperature), the geometrical vertical and horizontal extent, microphysical properties, such as particle size distribution and ice water content (IWC), the ice crystal shape (habit) is an important factor affecting the radiative properties of cirrus (e.g., Macke et al., 1998; Wendisch et al., 2005, 2007; Eichler et al., 2009). Furthermore, optical properties such as extinction coefficient, phase matrix, single–scattering albedo and asymmetry factor of non–spherical ice crystals may differ substantially from spheres (Takano and Liou, 1989; Fu and Liou, 1993; Macke, 1993). More recently, progress in the parametrization of optical properties of ice crystals in general circulation models (GCM) has been made (e.g., Kristjansson et al., 2000; Edwards et al., 2007), which uses an ensemble of ice crystal shapes including roughened surfaces. Recent studies by Yang et al. (2012) and Yi et al. (2013) emphasize the parametrization of ice particle surface roughness, which results in a reduction of the asymmetry factor compared to

smooth particles of the same size. The cloud radiative effect of cirrus is highly sensitive to the cirrus optical thickness, whereas only a weak sensitivity is found to effective radius. For the tropical region Choi and Ho (2006) found a warming net radiative effect of cirrus with an optical thickness less than 10 but a cooling effect for optical thickness larger than 10 observed from satellite measurements. With an observed occurrence of 60% of optically thin cirrus in the tropics, the warming of cirrus dominates the cooling and the radiative energy budget is determined by the variations of optically thin cirrus in the tropics.

1.3 Remote Sensing of Clouds

The most important microphysical parameters describing the radiative energy effects of clouds are the cloud optical thickness τ and the droplet effective radius r_{eff} (ratio of the third moment of the cloud droplet size distribution to its second moment). To investigate cloud properties of marine clouds different remote sensing methods are used on the basis of satellite, airborne, and ship-based radiation measurements. The synergy of cloud radar and microwave radiometer measurements (e.g., Dong and Mace, 2003; Wang and Sassen, 2002; Wang et al., 2004) is of great advantage. Long-term global cloud data such as the International Satellite Cloud Climatology Project (ISCCP, Rossow and Schiffer, 1991; Rossow and Cairns, 1995; Rossow et al., 1996) are based on space-borne observations of cloud reflectivity. In non-absorbing water vapor wavelength regions (visible) cloud reflectivity primarily depends on τ , whereas due to the proportionality of the liquid/ice absorption coefficient and r_{eff} (in the solar spectral region) cloud reflectivity primarily depends on r_{eff} in liquid water/ice absorbing wavelength regions (near-infrared). This is the basis of most satellite-based cloud retrievals (e.g., Nakajima and King, 1990; Platnick and Twomey, 1994; Nakajima and Nakajima, 1995). Operational retrieval algorithms, such as the Moderate Resolution Imaging Spectroradiometer (MODIS) algorithm, additionally include emitted thermal radiation measurements (King et al., 1997, 2006). The cloud reflectivity is mostly determined by the upper cloud layers in these reflectivity-based retrievals (Platnick et al., 2003). Platnick (2000) modeled photon transport through cloud layers using vertical weighting functions to quantify the relative contributions of distinct cloud layers to the retrieval of r_{eff} . These simulations show that the upper part of the cloud is weighted stronger than lower cloud parts using reflectivity. In contrast, transmissivity is mostly determined by the center layers of the cloud.

However, transmissivity principally contains less information on r_{eff} as reflectivity. This is due to the competing effects of absorption and forward scattering. With increasing r_{eff} forward scattering increases; however, in this case also cloud droplet absorption increases in the near-infrared wavelength region. Furthermore, transmissivity has a non-monotonic behavior with regard to τ . This causes ambiguous retrieval results in contrast to using reflectivity, which is a monotonic function of τ (Kikuchi et al., 2006). For optically thin clouds ($\tau < 5$) an increase in τ results in an increased number of scattered water droplets in the upward looking sensor field-of-view and thus larger transmissivity. As the cloud becomes optically thicker, zenith radiance decreases and attenuation dominates which enhances the uncertainty of r_{eff} retrievals.

Different ground-based retrievals were developed to obtain τ and r_{eff} . A number of studies utilizes a combination of instruments. Min et al. (2003) and Feingold et al. (2006) used solar irradiance and microwave observations to retrieve τ and r_{eff} by a least-squared error minimization technique. Garrett and Zhao (2013) retrieved τ and r_{eff} based on cloud transmissivity at 1040 cm^{-1} and cloud emissivities in two other microwindows from interferometer measurements. Other studies obtain simultaneously τ and r_{eff} using zenith radiance measurements (Rawlins and Foot, 1990; Kikuchi et al., 2006; Schofield et al., 2007; Pandithurai et al., 2009; McBride et al., 2011, 2012; Chiu et al., 2012). The basic principle of these transmissivity-based methods is to combine a non-water absorbing wavelength with a liquid-water/ice absorbing wavelength. Rawlins and Foot (1990) used the spectral transmissivity at 1040 nm and the ratio of transmissivity at 1550 nm and 1040 nm to retrieve τ and r_{eff} . They demonstrate that τ can be retrieved from transmissivity measurements; however, the r_{eff} retrievals were not significant given their high uncertainties. Kikuchi et al. (2006) and Pandithurai et al. (2009) used transmissivity of liquid water clouds at 1020 nm to 1600 nm, or 2200 nm. For τ between 10 and 35 they found r_{eff} ranging from 1 – 6 μm for a single-layer stratocumulus cloud.

McBride et al. (2011) introduced a method for retrieving τ and r_{eff} with enhanced sensitivity to r_{eff} using the spectral slope of transmissivity between 1565 nm and 1634 nm in combination with transmissivity at a visible wavelength. This spectral method agreed with the common two-wavelength approach for τ retrievals but improved results for r_{eff} for $\tau > 25$. Furthermore, the comparison of retrieved τ , r_{eff} and liquid water path (*LWP*) agree well with satellite and ship-based microwave observations. The comparison of airborne in situ measurements of averaged vertical profiles of cloud droplet size distribution with ship-based transmissivity retrievals of r_{eff} reveal with retrieved mean values of 7.7 μm and 5.7 μm , respectively (McBride et al., 2012). Larger differences in retrieved r_{eff} for the analyzed stratocumulus scene were found for satellite observations and ship-based spectral irradiance observations with mean values of 11.5 μm and 9.5 μm , respectively. The different sampling volumes of these remote sensing techniques are reported as the most likely contributors to the observed variability in r_{eff} (McBride et al., 2012). More recently, almost parallel but independent from this work (Brückner et al., 2014), LeBlanc et al. (2014) introduced a new retrieval method for τ , r_{eff} , and additionally cloud phase using ground-based spectral transmissivity. Using multiple spectral variations in zenith radiance due to absorption and scattering of liquid water and ice clouds, they found a closer fit by a weighted least-squares retrieval between observed and modeled transmissivity compared to existing retrieval methods.

1.4 Objectives

This work is concerned with a ground-based retrieval of τ , r_{eff} and *LWP* of marine clouds by analyzing spectral zenith radiance measurements. A new retrieval technique is developed which is similar to LeBlanc et al. (2014). As shown above the microphysical properties of different cloud types are one essential parameter affecting the radiative effects of clouds and the Earth’s energy budget. Data used in this work are based on spectral zenith radiance measurements with the COmpact RAdiation measurement System (CORAS). The

measurements are complemented with data collected with different active and passive remote sensing instruments. The data set was gathered during three Atlantic ocean transfers of the Research Vessel (RV) *Polarstern* in the framework of the German Leibniz-network OCEANET-project (autonomous measurement platforms for material and energy exchange between ocean and atmosphere). The measurements benefit from the regular transfers of RV *Polarstern* between the polar regions on both hemispheres and provides the opportunity to observe clouds in three climate zones (tropics, subtropics, and mid-latitudes) which enables to obtain a statistic of cloud properties in a meridional cross section. The observations deliver high temporal and spatial resolution of atmospheric cloud properties. Thus, variability in cloud parameters and microphysical inhomogeneities can be resolved and quantified for different cloud types.

The outline of this thesis is as follows: The radiative and cloud optical quantities are introduced in Chapter 2. In Chapter 3 a detailed description of the radiation measurements and the calibration procedure of CORAS is given. The additional remote sensing instrumentation of the OCEANET-Atmosphere container is introduced and a brief overview of the three Atlantic transfers during the OCEANET-project that are used in this study is given. The radiative transfer model as well as existing ground-based retrievals are presented in Chapter 4. These common retrievals reveal some problems which are avoided with a new multi-wavelength cloud retrieval developed in this work to infer τ and r_{eff} using transmissivity measurements. The retrieval is applied to different cloud types in Chapter 5. A cloud statistics is given in Chapter 6. The thesis is completed with a summary and conclusion as well as an outlook in Chapter 7.

2 Definitions

In this chapter the terminology used in this work is introduced. The subsequent definitions follow the textbook on atmospheric radiative transfer by Wendisch and Yang (2012). The fundamental radiometric quantities (Section 2.1), the cloud optical quantities (Section 2.2), including the single-scattering properties of individual cloud particles (Section 2.2.1) and volumetric (bulk) optical properties of clouds (Section 2.2.2) are introduced. In Section 2.3 the microphysical properties of liquid water and ice clouds are presented. The radiative transfer equation is explained in Section 2.4.

2.1 Radiative Quantities

The radiant energy flux Φ_λ is the radiant energy E_{rad} (in units of $\text{W s} = \text{J}$) passing through a small area element within a time interval $t + dt$, for a wavelength range $\lambda + d\lambda$:

$$\Phi_\lambda = \frac{d^2 E_{\text{rad}}}{dt d\lambda}. \quad (2.1)$$

Φ_λ in units of W nm^{-1} defines the power of electromagnetic (EM) radiation at a certain position and time. By normalizing Φ_λ to the corresponding area element $d^2 A$, the spectral radiant energy flux density F_λ is derived by:

$$F_\lambda = \frac{d^2 \Phi_\lambda}{d^2 A} = \frac{d^4 E_{\text{rad}}}{d^2 A dt d\lambda}. \quad (2.2)$$

The unit of F_λ , also called spectral irradiance, is $\text{W m}^{-2} \text{nm}^{-1}$. F_λ is a measure of the spectral radiant energy flux transported through a unit area. The orientation of the unit area $d^2 A$ can be random but for radiative transfer in the atmosphere it is assumed horizontal. F_λ is weighted with the cosine of the angle of incidence θ (zenith angle) which defines the orientation of $d^2 A(\hat{n})$ and $d^2 A_\perp(\hat{n}_\perp)$ (see Figure 2.1). The spectral radiance $I_\lambda(\hat{s})$ in units of $\text{W m}^{-2} \text{nm}^{-1} \text{sr}^{-1}$ is defined as the radiant energy within a solid angle element $d^2 \Omega$ which is pointed along the direction of propagation \hat{s} :

$$I_\lambda(\hat{s}) = \frac{d^4 \Phi_\lambda}{\cos \theta d^2 A d^2 \Omega} = \frac{d^6 E_{\text{rad}}}{dt d\lambda \cos \theta d^2 A d^2 \Omega}. \quad (2.3)$$

The geometry for the definition of $I_\lambda(\hat{s})$ is illustrated in Figure 2.1. The solid angle element $d^2 \Omega$ is expressed in terms of the atmospheric zenith angle θ and the atmospheric azimuth

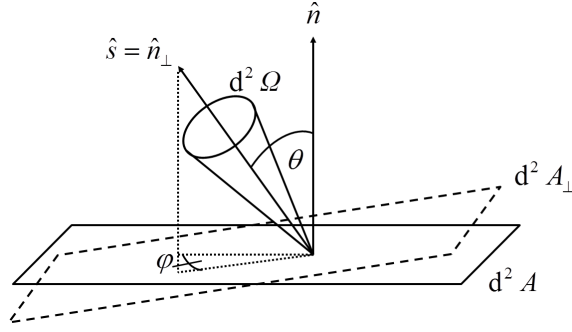


Figure 2.1: Geometry relevant for the definition of irradiance and radiance.

angle φ and defined as $d^2\Omega = \sin\theta d\theta d\varphi$ (in units of sr). In Eq. (2.3) the quantity $d^2A_\perp = \cos\theta \cdot d^2A$ is the projection of d^2A onto a perpendicular plane to the propagation direction \hat{s} .

The integration of $I_\lambda(\hat{s})$ over $d^2\Omega$ gives F_λ :

$$F_\lambda = \iint_{2\pi sr} I_\lambda(\hat{s}) \cdot \cos\theta d^2\Omega \quad (2.4)$$

$$= \int_0^{2\pi} \int_0^\pi I_\lambda(\theta, \varphi) \cdot \cos\theta \cdot \sin\theta d\theta d\varphi. \quad (2.5)$$

For atmospheric applications F_λ can be separated by integration over the lower [$\theta = (\pi/2 \dots \pi), \varphi = (0 \dots 2\pi)$] or the upper [$\theta = (0 \dots \pi/2), \varphi = (0 \dots 2\pi)$] hemisphere which yields the upward irradiance F_λ^\uparrow , or downward irradiance F_λ^\downarrow :

$$F_\lambda^\downarrow = \int_0^{2\pi} \int_0^{\pi/2} I_\lambda(\theta, \varphi) \cdot \cos\theta \cdot \sin\theta d\theta d\varphi \quad (2.6)$$

$$F_\lambda^\uparrow = - \int_0^{2\pi} \int_{\pi/2}^\pi I_\lambda(\theta, \varphi) \cdot \cos\theta \cdot \sin\theta d\theta d\varphi. \quad (2.7)$$

According to the specific direction \hat{s} , the upward radiance ($I_\lambda^\uparrow(\hat{s})$) or downward radiance ($I_\lambda^\downarrow(\hat{s})$) can be defined. In case of an anisotropic distribution of radiation, radiance is independent of the orientation ($I_\lambda(\hat{s}) = I_{\lambda, \text{iso}}$) which results in:

$$F_{\lambda, \text{iso}}^\uparrow = F_{\lambda, \text{iso}}^\downarrow = \pi \cdot I_{\lambda, \text{iso}}. \quad (2.8)$$

However, for atmospheric applications the radiation field is mostly anisotropic and F_λ^\downarrow consists of a direct and diffuse component. The upward irradiance F_λ^\uparrow is diffuse only.

2.2 Optical Properties of Clouds

Consider the solar radiation incident on a plane parallel atmosphere, the reflected radiation at the top of the atmosphere and the transmitted radiation at the bottom of the atmosphere is expressed by $I_\lambda^\uparrow(0, -\mu, \varphi)$ and $I_\lambda^\downarrow(\tau_c, \mu, \varphi)$, respectively. Here, μ is the cosine of zenith angle θ . The spectral reflectivity function $R_\lambda(\tau_c; \mu, \mu_0, \varphi)$ and the spectral transmissivity function $T_\lambda(\tau_c; \mu, \mu_0, \varphi)$ are defined as:

$$R_\lambda(\tau_c; \mu, \mu_0, \varphi) = \frac{\pi \cdot I_\lambda^\uparrow(0, -\mu, \varphi)}{\mu_0 \cdot F_{\lambda, \text{TOA}}} \quad (2.9)$$

$$T_\lambda(\tau_c; \mu, \mu_0, \varphi) = \frac{\pi \cdot I_\lambda^\downarrow(\tau_c, \mu, \varphi)}{\mu_0 \cdot F_{\lambda, \text{TOA}}}. \quad (2.10)$$

τ_c is the total optical thickness of the atmosphere (or the cloud), μ is the absolute value of the cosine of observation angle measured with respect to the positive direction of τ_c , μ_0 is the cosine of solar zenith angle θ_0 , φ is the atmospheric azimuth angle, and $F_{\lambda, \text{TOA}}$ is the spectral incident flux density at top of atmosphere (TOA).

The transmissivity function obtained from the ground viewing zenith, that is for $\mu = 1$, is defined as the spectral transmissivity $T_\lambda(\tau_c; \mu, \mu_0, \varphi)$. Accordingly, the reflectivity function obtained from nadir viewing is defined as the spectral reflectivity $R_\lambda(\tau_c; \mu, \mu_0, \varphi)$ with $\mu = -1$. T_λ and R_λ are independent of direction for an isotropic scattered radiation field. Throughout this thesis, a measurement-based definition of transmissivity is used. Here, the surface and the atmosphere below and above the cloud contributes to I_λ^\downarrow . Therefore, the transmissivity defined here is not solely determined by the cloud layer.

2.2.1 Individual Cloud Particles

EM radiation passing through the atmosphere is scattered, absorbed and emitted by gas molecules, aerosol particles and cloud particles. The interaction between EM radiation and individual particles in the atmosphere can be described by three single-scattering properties: the extinction cross section C_{ext} , the single-scattering albedo $\tilde{\omega}$ and the scattering phase function \mathcal{P} . These quantities depend on the mass/cross-section area, the spectral complex index of refraction and also on the particle shape, size and orientation of individual particles. For spherical liquid water droplets an analytic solution results from Mie-Theory (Mie, 1908; Bohren and Huffman, 1998). For irregular particles, such as ice particles or aerosol particles, an analytic solution does not exist. Therefore, numerical solutions have to be used with different computational methods, e.g., Yang and Liou (1996); Baum et al. (2005a,b, 2007); Yang et al. (2005, 2013).

The extinction cross section C_{ext} (in units of m^2) is a measure of how effective a single cloud particle interacts with incident EM radiation. It is defined by the attenuated radiant energy flux relative to the incident flux density F_λ :

$$C_{\text{ext}} = \frac{\Phi_\lambda}{F_\lambda}. \quad (2.11)$$

The sum of the absorption cross section C_{abs} and the scattering cross section C_{sca} (both in units of m^2) is equal to C_{ext} ,

$$C_{\text{ext}} = C_{\text{abs}} + C_{\text{sca}}. \quad (2.12)$$

The dimensionless single-scattering albedo $\tilde{\omega}$ is a relative measure of how much incident radiation is scattered or absorbed by a single cloud particle. It is defined by the ratio of C_{sca} and C_{ext} ,

$$\tilde{\omega} = \frac{C_{\text{sca}}}{C_{\text{ext}}} = \frac{C_{\text{sca}}}{C_{\text{abs}} + C_{\text{sca}}}, \quad (2.13)$$

and is closely related to the imaginary part of the refractive index \tilde{n}_i . The values of $\tilde{\omega}$ range from 0 (for non-scattering particles) to 1 (for non-absorbing particles).

In Figure 2.2 the imaginary part of the spectral refractive index \tilde{n}_i and the single-scattering albedo $\tilde{\omega}$ for liquid water droplets and solid column shaped ice crystals of different sizes are plotted as a function of wavelength. The spectral characteristics of $\tilde{\omega}$ are closely linked to \tilde{n}_i shown in Figure 2.2a. With increasing \tilde{n}_i absorption increases, which means a decrease of $\tilde{\omega}$. Figure 2.2b shows that $\tilde{\omega}$ is sensitive to the particle size (cross section). The larger the cloud particles the smaller $\tilde{\omega}$.

The dimensionless scattering phase function \mathcal{P} characterizes the angular probability of scattering radiation incident from direction $[\mu_i, \varphi_i]$ and scattered into direction $[\mu, \varphi]$. By normalization to 4π sr the scattering phase function \mathcal{P} is given by:

$$\int_0^{2\pi} \int_{-1}^1 \mathcal{P}([\mu_i, \varphi_i] \rightarrow [\mu, \varphi]) d\mu d\varphi = 4\pi \text{ sr}. \quad (2.14)$$

The scattering angle ϑ is defined by the relation between the incident and scattered radiation in the scattering plane as follows:

$$\cos\vartheta = \mu \cdot \mu_i + \sqrt{1 - \mu^2} \cdot \sqrt{1 - \mu_i^2}. \quad (2.15)$$

Scattering phase functions for single liquid water droplets and solid column shaped ice crystals for two different effective radii are illustrated in Figure 2.3. Differences in \mathcal{P} result from the different particle sizes and shapes. As indicated by the left close up panel for scattering angles $\vartheta = 0 - 5^\circ$, non-spherical ice particles exhibits a strong but narrow forward scattering peak, while the forward peak for liquid water droplets is weaker. The intensity of the forward peak increases with increasing particle diameter. Furthermore, the fluctuation in \mathcal{P} from the liquid water droplets compared to \mathcal{P} of solid columns results from resonances in the solution of Mie-Theory.

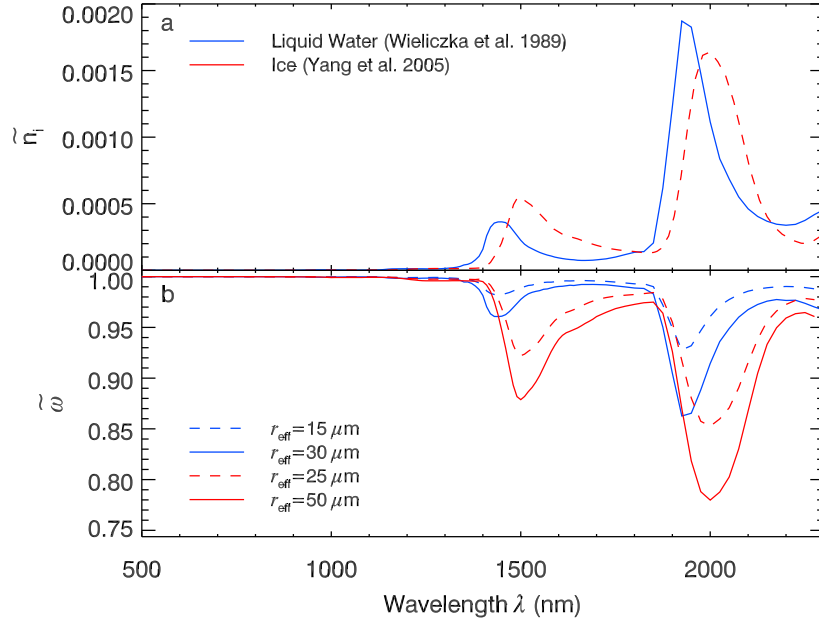


Figure 2.2: The imaginary part of the spectral refractive index \tilde{n}_i of liquid water (blue lines) and ice (red lines) over the wavelength region (panel a). Data were provided by Wieliczka et al. (1989); Yang et al. (2005). Spectral single-scattering albedo $\tilde{\omega}$ of different effective radii r_{eff} (see Sec. 2.3) for liquid water droplets and ice crystals (panel b). For an individual particle the effective radius can be described as the ratio of the volume of a particle to its cross-section.

\mathcal{P} can be expanded into a series of Legendre polynomials:

$$\mathcal{P}(\cos \vartheta) = \sum_{n=0}^{\infty} C_n \cdot P_n(\cos \theta). \quad (2.16)$$

The dimensionless Legendre polynomials $P_n(\cos \theta)$ are orthogonal basis functions given by:

$$P_n(\cos \theta) = \frac{1}{2^n n!} \frac{d^n}{d \cos^n \vartheta} (\cos^2 \vartheta - 1)^n, \quad \cos \vartheta \in [-1, 1] \quad n = 1, 2, \dots \quad (2.17)$$

The contribution of each Legendre polynomial to the Legendre expansion is given by the dimensionless Legendre coefficients C_n :

$$C_n = \frac{2n+1}{2} \int_{-1}^{+1} \mathcal{P}(\cos \vartheta) \cdot P_n \cos \theta \, d \cos \vartheta. \quad (2.18)$$

An infinite number of Legendre polynomials would be required to accurately represent the phase function $\mathcal{P}(\cos \vartheta)$. For practical applications, only a finite number Λ of Legendre polynomials $P_n(\cos \theta)$ is used. The computing time needed for the calculation of C_n increases with increasing number of C_n . The value of Λ is chosen on the basis of the required accuracy of phase function. The truncated phase function $\mathcal{P}^*(\cos \vartheta)$ at a certain degree of the series Λ is given as follows:

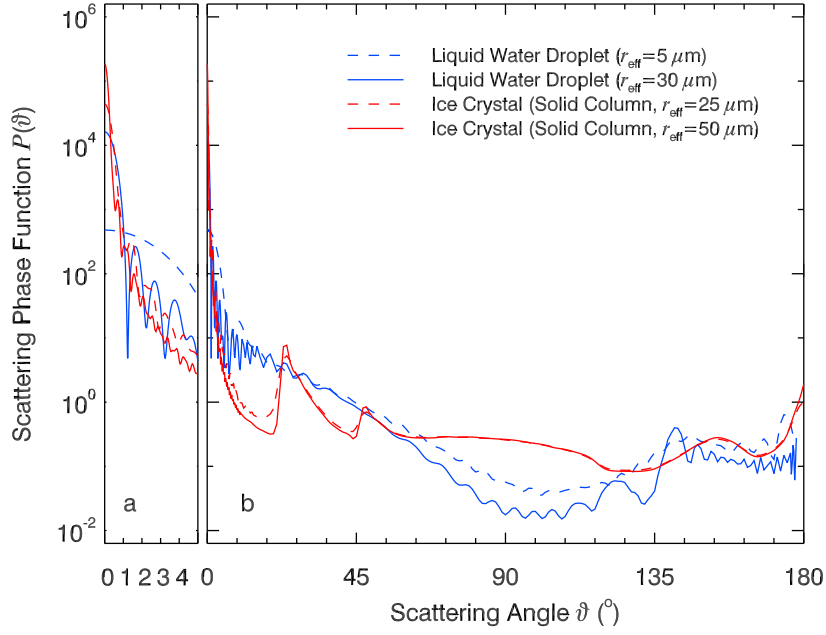


Figure 2.3: Scattering phase functions for individual particles at 530 nm wavelength (panel b). Blue lines refer to liquid water droplets with two different values of radii r_{eff} , red lines refer to solid column shaped ice crystals with two different values of radii r_{eff} . Panel a shows a close up for scattering angles $\vartheta = 0 - 5^\circ$. Data for ice crystals were provided by Yang et al. (2013).

$$\mathcal{P}^*(\cos \vartheta) = \sum_{n=0}^{\Lambda-1} C_n \cdot P_n(\cos \theta). \quad (2.19)$$

The truncation of the forward scattering peak (Wiscombe, 1977) minimizes the computational time. The truncation approximation proposed from Potter (1970), uses the fact, that in atmospheric applications, the forward scattering peak in scattering angles close to $\vartheta = 0^\circ$ is often considered as being unscattered and can be practically reallocated into the direct solar radiation. The truncated scattering phase function \mathcal{P}_{tr} results from the truncated forward scattering in the original \mathcal{P} :

$$\mathcal{P}_{\text{tr}} = \mathcal{P} - h_{\text{tr}}. \quad (2.20)$$

Here, h_{tr} is the truncated part of \mathcal{P} . The truncation increases the fraction of direct radiation and by the same amount reduces the fraction of scattered radiation. Accordingly, to maintain energy conservation, the single-scattering properties $(C_{\text{ext}}, \tilde{\omega}, \mathcal{P})$ have to be scaled with the fraction of energy f_{tr} within the truncated forward peak. With an unchanged absorption cross section $C'_{\text{abs}} = C_{\text{abs}}$ and the scaled scattering cross section C'_{sca} given by $C'_{\text{abs}} = (1 - f_{\text{tr}})$, the cross section C_{ext} and the single-scattering albedo $\tilde{\omega}$ are scaled accordingly by:

$$C'_{\text{ext}} = (1 - f_{\text{tr}} \cdot \tilde{\omega}) \cdot C_{\text{ext}}, \quad (2.21)$$

and,

$$\tilde{\omega}' = \frac{1 - f_{\text{tr}}}{1 - f_{\text{tr}} \cdot \tilde{\omega}} \cdot \tilde{\omega}. \quad (2.22)$$

Because of the normalization introduced in Eq. (2.14) the truncated phase function \mathcal{P}_{tr} has to be scaled too, with:

$$\mathcal{P}'_{\text{tr}} = \frac{\mathcal{P}_{\text{tr}}}{1 - f_{\text{tr}}}. \quad (2.23)$$

The Legendre coefficients of \mathcal{P}_{tr} are described by,

$$C'_n = \frac{C_n - D_n}{1 - f_{\text{tr}}}, \quad (2.24)$$

with D_n representing the Legendre coefficients of the truncated function h_{tr} .

The asymmetry factor g related with an individual particle is a measure of the angular distribution of scattered radiation by the particle. Using \mathcal{P} it is defined by:

$$g = \iint_{4\pi} p(\vartheta) \cdot \cos \vartheta \, d^2\Omega = \frac{1}{2} \int_{-1}^1 \cos \vartheta \cdot \mathcal{P}(\cos \vartheta) \, d \cos \vartheta, \quad (2.25)$$

where the phase function p represents the relative angular distribution of the scattered radiation and the assumption that $\mathcal{P}(\cos \vartheta)$ is independent of the scattering azimuthal angle. A value of $g = 1$ means pure forward scattering ($\vartheta = 0^\circ$, $\cos \vartheta = 1$), while $g = -1$ means specular reflection in the backward direction ($\vartheta = 180^\circ$, $\cos \vartheta = -1$). In general, $g = 0$ indicates scattering directions evenly distributed between forward and backward directions, i.e., isotropic scattering (e.g., Rayleigh scattering).

2.2.2 Volumetric Properties of Clouds

The volumetric (bulk) optical properties of a cloud particle volume are calculated by integration of the single-scattering properties. The properties are weighted by the number size distribution $\frac{dN}{d \log D}$ of the scattering cloud particles within a respective maximum dimension interval $D + \delta D$ (Wendisch et al., 2005), where D is the particle diameter in units of μm . The spectral volumetric extinction coefficient $\langle b_{\text{ext}}(\lambda) \rangle$ and the spectral volumetric scattering coefficient $\langle b_{\text{sca}}(\lambda) \rangle$ both in units of m^{-1} are defined as:

$$\langle b_{\text{ext}}(\lambda) \rangle = \int_0^\infty C_{\text{ext}}(\lambda, D') \cdot \frac{dN}{d \log D}(D') \, d \log D', \quad (2.26)$$

$$\langle b_{\text{sca}}(\lambda) \rangle = \int_0^\infty C_{\text{sca}}(\lambda, D') \cdot \frac{dN}{d \log D}(D') \, d \log D'. \quad (2.27)$$

The dimensionless cloud optical thickness τ is the integral of $\langle b_{\text{ext}}(\lambda) \rangle$ of a cloud between cloud base z_{base} and cloud top z_{top} .

$$\tau = \int_{z_{\text{base}}}^{z_{\text{top}}} \langle b_{\text{ext}}(\lambda) \rangle(z') dz'. \quad (2.28)$$

The dimensionless spectral volumetric single-scattering albedo $\langle \tilde{\omega}(\lambda) \rangle$ is derived by:

$$\langle \tilde{\omega}(\lambda) \rangle = \frac{1}{\langle b_{\text{ext}}(\lambda) \rangle} \int_0^\infty \tilde{\omega}(\lambda, D') \cdot C_{\text{ext}}(\lambda, D') \cdot \frac{dN}{d \log D}(D') d \log D'. \quad (2.29)$$

The volumetric phase function $\langle p(\lambda) \rangle$ in units of sr^{-1} , is obtained by:

$$\langle p(\lambda, \vartheta) \rangle = \frac{1}{\langle b_{\text{sca}}(\lambda) \rangle} \int_0^\infty p(\lambda, \vartheta, D') \cdot C_{\text{sca}}(D') \cdot \frac{dN}{d \log D}(D') d \log D'. \quad (2.30)$$

The relationship between the dimensionless phase function $\mathcal{P}(\vartheta)$ and the phase function $p(\vartheta)$ is given by $\mathcal{P}(\vartheta) = 4\pi \text{sr} \cdot p(\vartheta)$.

2.3 Microphysical Properties of Clouds

The effective droplet radius r_{eff} in units of μm is defined as an area-weighted mean radius calculated from the ratio of the third to the second moment of a droplet number size distribution $\frac{dN}{d \log D}(D)$ (Hansen and Travis, 1974).

$$r_{\text{eff}} = \frac{1}{2} \frac{\int_0^\infty D'^3 \frac{dN}{d \log D}(D') d \log D'}{\int_0^\infty D'^2 \frac{dN}{d \log D}(D') d \log D'}. \quad (2.31)$$

In general, r_{eff} is related to the ratio of the volume of a cloud particle to its cross-sectional area. For non-spherical particles, like ice crystals, r_{eff} is calculated as follows (Yang et al., 2000; Key et al., 2002):

$$r_{\text{eff}} = \frac{3}{4} \frac{\int V(D') \cdot \frac{dN}{d \log D}(D') d \log D'}{\int A(D') \cdot \frac{dN}{d \log D}(D') d \log D'}, \quad (2.32)$$

where V and A are the volume and the projected area of the particle with the maximum dimension D (μm) of an ice crystal. V and A are obtained from spherical diameter with equivalent V/A . This equivalent V/A refers to spheres with the same V/A as the ice crystal (Grenfell and Warren, 1999; Yang et al., 2000).

The liquid water content LWC in units of g m^{-3} is defined as the mass concentration of liquid water droplets in the cloud volume:

$$LWC = \frac{4\pi}{3} \cdot \rho_w \int_0^\infty \left(\frac{D'}{2}\right)^3 \cdot \frac{dN}{d \log D}(D') d \log D', \quad (2.33)$$

with the density of liquid water ρ_w . LWC can be parametrized using τ and r_{eff} for a vertically homogeneous cloud from cloud base z_{base} to cloud top z_{top} with,

$$LWC = \frac{2\rho_w}{3} \cdot \int_{z_{\text{base}}}^{z_{\text{top}}} \frac{r_{\text{eff}} \cdot \tau}{z'} dz'. \quad (2.34)$$

Replacing $\frac{2}{3}$ with $\frac{5}{9}$ parametrize the LWC for an adiabatic cloud (Wood and Hartmann, 2006). The liquid water path LWP in units of g m^{-2} is the vertical integral of LWC :

$$LWP = \int_{z_{\text{base}}}^{z_{\text{top}}} LWC(z') dz'. \quad (2.35)$$

2.4 Radiative Transfer Equation

The extinction (attenuation) of direct solar radiance I_{dir} along a path through the (cloudy) atmosphere, with τ as a vertical coordinate, can be described via the Beer–Lambert–Bouguer law (also called Beer’s law):

$$I_{\text{dir}}(\tau, \mu_0, \varphi_0) = \frac{S_0}{4\pi} \cdot \exp\left(-\frac{\tau}{\mu_0}\right). \quad (2.36)$$

Here, $\mu_0 = \cos\theta_0$ and φ_0 define the position of the sun, S_0 is the incident extraterrestrial irradiance at the top of atmosphere (solar constant). For the sake of completeness, the term sr^{-1} should be considered in the following definitions but here it is omitted. From Eq. (2.36) it follows, that I_{dir} is strongly attenuated in the presence of clouds because τ is large for clouds. Thus, solar radiative transfer through clouds can be described by the diffuse radiance I_{diff} . For the solar spectral region from $\lambda = 0.2 - 5 \mu\text{m}$, the thermal emission of radiation can be neglected. Assuming a plane–parallel, horizontally homogeneous atmosphere the one–dimensional (1D) radiative transfer equation (RTE) can be written as (Chandrasekhar, 1950):

$$\mu \frac{dI_{\text{diff}}(\tau, \mu, \varphi)}{d\tau} = I_{\text{diff}} - (J_{\text{dir}} + J_{\text{diff}}), \quad (2.37)$$

where J_{dir} and J_{diff} describe the radiance scattered into the viewing direction. The single–scattering term J_{dir} , quantifies the direct solar radiation, the multiple–scattering term J_{diff} specifies the diffuse solar radiation, which is scattered into the viewing direction, respectively. J_{dir} and J_{diff} depend on the absorption ($\tilde{\omega}$) and the scattering phase function \mathcal{P} . This result as:

$$J_{\text{dir}} = \frac{\tilde{\omega}(\tau)}{4\pi} \cdot S_0 \cdot \exp\left(-\frac{\tau}{\mu_0}\right) \cdot \mathcal{P}(\tau, [-\mu_0, \varphi_0] \longrightarrow [\mu, \varphi]), \quad (2.38)$$

$$J_{\text{diff}} = \frac{\tilde{\omega}(\tau)}{4\pi} \int_0^{2\pi} \int_{-1}^1 I_{\text{diff}}(\tau, \mu_i, \varphi_i) \cdot \mathcal{P}(\tau, [\mu_i, \varphi_i] \longrightarrow [\mu, \varphi]) d\mu_i d\varphi_i. \quad (2.39)$$

3 Experimental

Data presented in this work were collected during the OCEANET–project (autonomous measurement platforms for material and energy exchange between ocean and atmosphere). A container with several active and passive remote sensing instruments was operated on the German Research Vessel (RV) *Polarstern* (Alfred-Wegener Institute for Polar and Marine Research, AWI). The COmpact RADIation measurements System (CORAS) measured the spectral zenith radiance data. In Section 3.1 the Atlantic ocean transfer cruises are introduced. CORAS, the calibration procedure, measurement uncertainties and horizontal misalignment correction procedures are introduced in Section 3.2. Details of the instrumentation of the OCEANET-Atmosphere container are provided in Section 3.3.

3.1 Atlantic Transfers on RV *Polarstern*

RV *Polarstern* is a German polar research and supply vessel from the ice category Arctic/Antarctic Research Classification ARC3. Technical data of the ship are given in El Naggar and Fahrbach (2010). The main operational areas are the polar regions in the respective summer hemispheres. The ship is a platform for atmospheric, oceanographic, chemical, biological and geological experiments.

The regular Atlantic ocean transfers between the two hemispheres are a good opportunity to perform meridional atmospheric measurements in tropical, subtropical and mid-latitude climate zones. The data used in this work were collected during three Atlantic transfer cruises of RV *Polarstern* (ANT-XXVII/4 in Spring 2011, ANT-XXVIII/5 in Spring 2012 and ANT-XXIX/1 in Fall 2012) between Cape Town (South Africa), Bremerhaven (Germany), and Punta Arenas (Chile) back to Bremerhaven (Germany). Cruise plots are shown in Figure 3.1 and are listed in Table 3.1.

CORAS was installed on the ship on ANT-XXVII/4 from Cape Town to Bremerhaven in Spring 2011. The OCEANET-atmosphere container (see Section 3.3) was already tested and used on sea on previous cruises and was located on the higher-level monkey deck. In the first part of the cruise short phases of easterly winds with 7 Bft^a were observed. *Polarstern* reached the trade wind zone on April 23, where the typical trade wind cumuli were observed. While approaching the ITCZ on April 30, some rain showers occurred but thunderstorms did not cross the ship track. On May 4 *Polarstern* reached the northeast trade winds with prevailing 5 Bft. A short station (stop of the ship) was made on May 10 in Las Palmas (Gran Canaria). A high developed at 50° N/40° W moved southwest causing strong winds of

^aWind force is given in units of Bft according to the wind force scale. Here Beaufort Bft = $(v/0.8360 \text{ ms}^{-1})^{2/3}$, where v is the wind velocity in units of ms^{-1} .

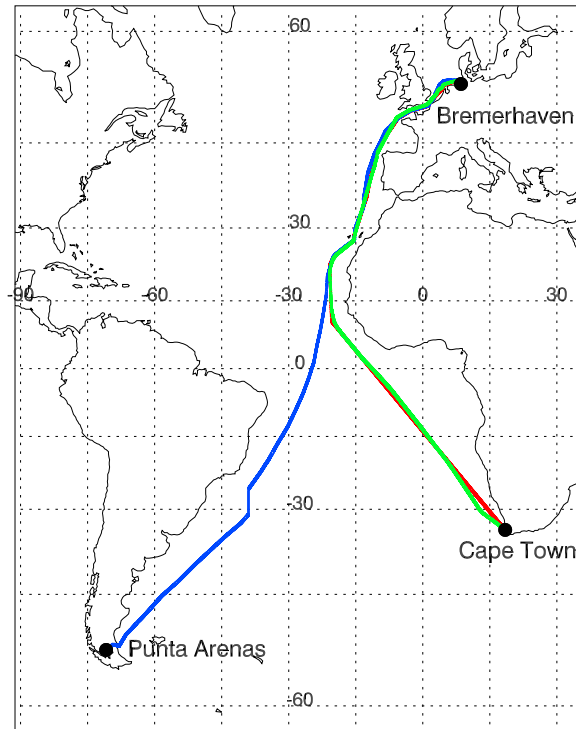


Figure 3.1: Cruise plots of ANT-XXVII/4 Cape Town back to Bremerhaven April/May 2011 (red), ANT-XXVIII/5 from Punta Arenas to Bremerhaven April/May 2012 (blue) and ANT-XXIX/1 from Bremerhaven back to Cape Town Oct/Nov 2012 (green). Numbers indicate geographic longitude and latitude (in degrees).

9 Bft off the Iberian Peninsula. A rough sea with swell between 4 – 5 m were observed and, therefore, no measurements were performed on May 14–15. After passing the high (May 16) in the Bay of Biscay the west wind zone was approached while entering the English Channel and during the remaining cruise 4 – 5 Bft dominated. The measurements were finished on May 18.

ANT-XXVIII/5 from Punta Arenas to Bremerhaven with the short station in Las Palmas (May 6) in Spring 2012 took place with the same measurement setup described before but without lidar (see Section 3.3). The OCEANET-container was located on the helicopter deck; CORAS was installed on the superior monkey deck to avoid the influence of sea spray.

Table 3.1: Overview of Atlantic transfers of RV *Polarstern* with respective periods, start and end harbors, and the detailed cruise reports. ANT refer to expeditions from or to Antarctic.

Cruise leg	Period	Start/end harbor	Cruise report
ANT-XXVII/4	April 20 – May 20, 2011	Cape Town – Bremerhaven	El Nagggar (2011)
ANT-XXVIII/5	April 10 – May 15, 2012	Punta Arenas – Bremerhaven	Bumke (2012)
ANT-XXIX/1	October 26 – November 27, 2012	Bremerhaven – Cape Town	Auel (2013)

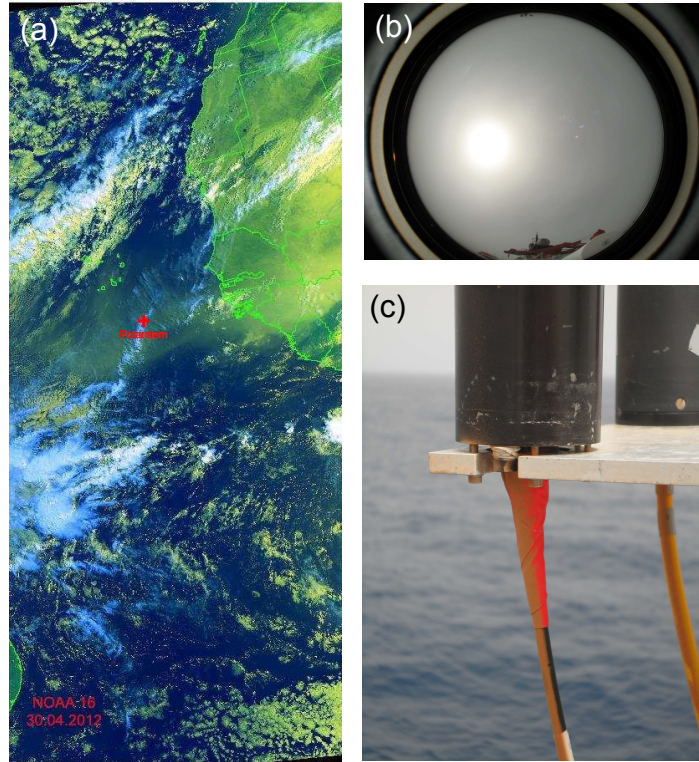


Figure 3.2: (a) Satellite Image from NOAA satellite on April 30, 2012. The red cross marks the position of RV *Polarstern*. (b) Typical clear sky photo during dust event from April 30, 2012. (c) Dust deposition on the optical inlets and fibers.

In the first part of the cruise the meteorological conditions were characterized by storms near the Drake Passage and the Strait of Magellan and winds up to 7 Bft. A high pressure system off Uruguay on April 17 caused mostly calm winds (4 Bft) and clear sky. *Polarstern* entered the trade wind zone on April 24. While approaching the ITCZ on April 27 showers and high sea surface temperatures of 30° C were observed. The northeasterly trade wind zone was reached on April 30 with gradually increasing wind up to 7 Bft.

During April 30 and May 3 (10° N – 20° N, 23° W – 20° W) Sahara dust was observed in the satellite image from NOAA in Figure 3.2a. The dust mobilization was forced some days before by synoptic-scale, mesoscale or local-scale winds and near surface turbulence processes (Schepanski et al., 2009). Topographic depressions like dry lake beds have been parametrized as preferential source areas for dust emissions (Tegen et al., 2002). A visibility less than 10km was measured temporarily. In Figure 3.2b a photo from the all sky imager from April 30 is shown. The strong scattering of radiation due to the dust can be seen, therefore, the sun became blurred to a fuzzy restricted spot. The brownish color can be seen at the horizon. Also dust deposition on the ground was observed, see Figure 3.2c. The influence of the dust is evident in the measured zenith radiances from CORAS. In Figure 3.3 $I_{\lambda, \text{obs}}^{\downarrow}$ over the CORAS wavelength region is plotted. The black spectrum refers to a clear sky observation with dust at 15.2 UTC on April 30, 2012 and the red line shows the spectrum corresponding to a clear sky observation without dust at 15.4 UTC on April 27, 2012. The solar zenith angle was $\theta_0 = 30^\circ$ for both cases. Due to the enhanced forward scattering the

diffuse zenith radiance at the surface is increased by up to 38% in the VIS region compared to clear conditions, while the direct zenith radiance is much reduced for dust. The influence from the dust due to increased aerosol optical depth (AOD) in the VIS is obvious. The Maritime Aerosol Network (MAN) component of AEROSOL ROBOTIC NETWORK (AERONET) provides ship-borne AOD measurements from the Microtops sun photometers (Smirnov et al., 2009). On April 30 an AOD of 1.79 at $\lambda = 500$ nm was measured. In comparison, the AOD on April 27 was only 0.17 under clear atmospheric conditions. The observations during the dust event are not part of this thesis. After passing the Canary Islands the dust vanished. However, dust events often come with dry and warm air layers that can be observed with the microwave radiometer. A high pressure system over the Atlantic has build a ridge toward the Bay of Biscay and, therefore, only light and variable winds were measured. While passing the English Channel on May 13 the measurements were finished. Generally, this cruise was characterized by a relatively calm sea with wave heights of 1 – 2 m (78%).

ANT-XXIX/1 from Bremerhaven to Cape Town started under the influence of an upper trough which brought cold air from the North Sea towards Europe and caused unstable stratification of the atmosphere. In the English Channel moist and cold air in connection with an upper trough and an intensive low pressure system which dominates the first part brought rain showers and winds up to 6 Bft, but later on October 29 when crossing the Biscay winds increased to 7 – 8 Bft. *Polarstern* reached Las Palmas on November 4 with air temperatures of 26° C. From November 5 to 8 the northeasterly trade winds with variable speeds of 3 – 6 Bft caused typical trade wind cumuli and clear sky conditions. On November 9 a thunderstorm cluster was predicted to become the center of a possible tropical depression. While approaching the ITCZ on November 10, strong convection caused cumulonimbus clouds, and some lightnings were often observed far away from the ship. On November 12 within the

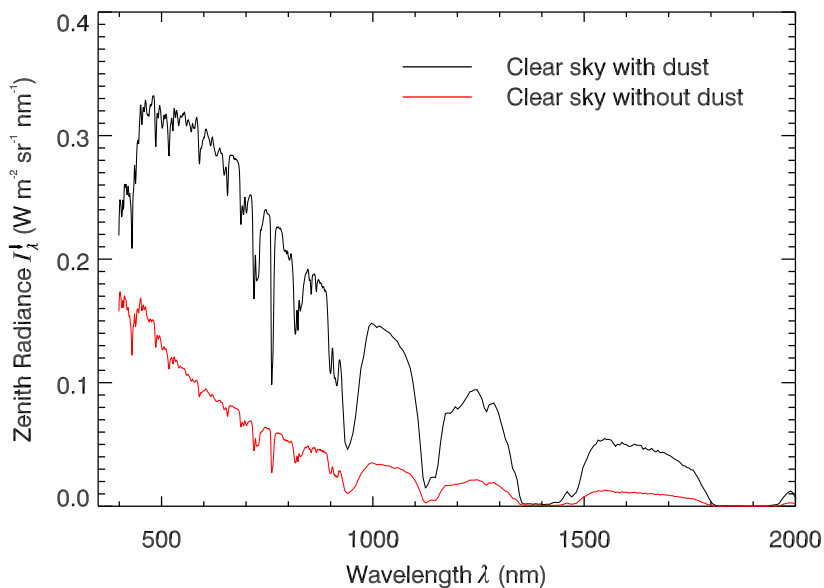


Figure 3.3: CORAS spectral zenith radiance across the wavelength region. Black solid line refers to measurements of clear sky with dust at 15.2 UTC on April 30, 2012. Red solid line refers to reference measurements of clear sky without dust at 15.4 UTC on April 27, 2012. Both measurements corresponds to a solar zenith angle $\theta_0 = 30^\circ$.

ITCZ convective processes caused by sea surface temperatures of 29° C thunderstorms were observed surrounding the ship, and a tropical shower in the afternoon caused a rain sum of 6.2 mm/h on *Polarstern*. The air temperatures dropped from 29° C to 23 – 24° C, the wind speed reached nearly 8 Bft for a short time. After passing the ITCZ, trade winds with typical cloudiness and stable conditions dominated. A strengthened inversion caused mostly a cloud-covered sky under stable stratification for the rest of the cruise. On November 24 the measurements were finished because of a passing cold front which brought maximum wave heights of up to 8 m.

3.2 CORAS

CORAS is a ground-based version of the albedometer introduced by Wendisch et al. (2001), which was designed as a modular system to measure spectral radiometric quantities from airborne platforms. Originally, the Spectral Modular Airborne Radiation measurement system (SMART-Albedometer) was used to measure upward and downward solar irradiances in the wavelength region $\lambda = 400 - 1000$ nm (e.g., Wendisch et al., 2001; Wendisch and Mayer, 2003; Wendisch et al., 2004). Several improvements of the original system were carried out over the years. Measurements of actinic flux densities (Jäkel et al., 2005) and spectral upward radiances (Ehrlich et al., 2008b) were added. The spectral region of the measurements were extended up to 2200 nm by Bierwirth (2008). The instrumentation setup and single components are illustrated in Figure 3.4.

Two upward-facing optical inlets collect downward radiance (I_{λ}^{\downarrow}) and irradiance (F_{λ}^{\downarrow}) data. Both optical inlets are sketched in Figure 3.5. The irradiance optical inlet collects photons from all directions of the (upper) hemisphere. The inlet is covered by a quartz-glass dome. A Spectralon[®] coated integrating sphere realizes the cosine-weighted collection of the photons (Bierwirth, 2008). A conical aperture in the center of the sphere circumvents that direct solar radiation reaches the outlet opening on the bottom of the integrating sphere. A detailed

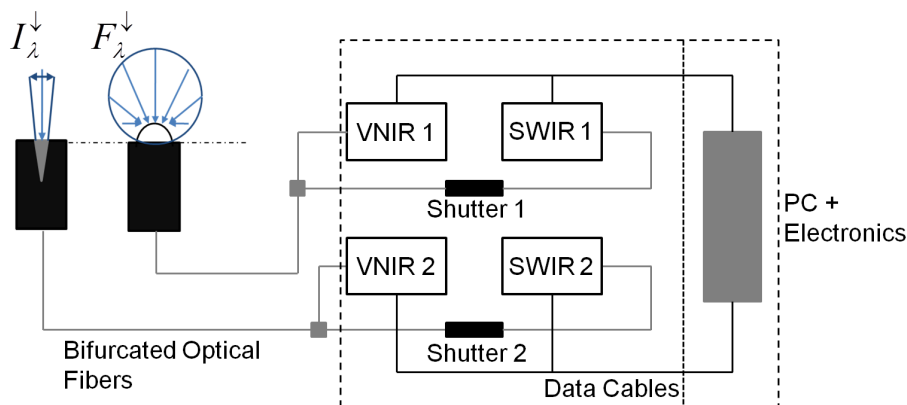


Figure 3.4: Instrumentation setup and single components of CORAS (see text for details). The two types of spectrometers are referred to as visible to near-infrared spectral wavelength region (VNIR) and shortwave-infrared spectral wavelength region (SWIR).

description of the design is given by Crowther (1997). The radiance inlet consists of a collimator lens (borosilicate crown (BK) 7 glass, *Carl Zeiss Jena, GmbH*) with a focal length of 31.6 mm (Ehrlich, 2009). The opening angle of different inlets were characterized and described by Ehrlich (2009). In this work, I_{λ}^{\downarrow} data are used with an opening angle of 2° .

The collected radiation from the inlets is transferred via two bifurcated optical fibers to the spectrometer system. The fibers are purchased from *CeramOptec, GmbH* and are isolated with a specific synthetic material adjusted to seaworthy conditions.

CORAS consists of four grating spectrometes (two for each optical inlet). The incoming radiation is spectrally dispersed by a grating and detected by a single-line photodiode array (PDA). Data acquisition from CORAS is realized with one computer (PC), in this way that the different measurement quantities are accessed in sequence and not simultaneously. The lower resulting temporal resolution (15 s per measurement quantity) is not a limiting factor for ground-based observations because either the system is fixed on the ground or, moves with a relatively slow velocity (usual ship velocity: 10 kn^b).

Different types of spectrometers manufactured by *Carl Zeiss Jena, GmbH* are used. The Multi Channel Spectrometer (MCS UV/NIR) cover the wavelength region $\lambda = 290 - 1000$ nm with a 1024 pixel PDA. The visible to near-infrared spectral wavelength region (VNIR) covers ultraviolet (UV) to near-infrared (NIR), but includes the entire visible (VIS) wavelength region from $\lambda = 380 - 700$ nm. The spectral resolution (Full Width at Half Maximum, *FWHM*) of VNIR is 2–3 nm. The Plane Grating Spectrometer (PGS) covers the shortwave-infrared spectral wavelength region (SWIR) $\lambda = 900 - 2200$ nm with a 256 pixel PDA with a *FWHM* = 8 – 10 nm. To obtain the radiation signal from the SWIR spectrometer it is necessary to real-time measure the dark signal (sum of electronic offset and thermally induced current) to derive the net signal (Bierwirth, 2008). The alternating measurements of radiation and dark signal is realized with an optical shutter purchased from *Ocean Optics*

^bThroughout this work the ship velocity is given in units of kn. It is 1 kn = 0.51 m s⁻¹.

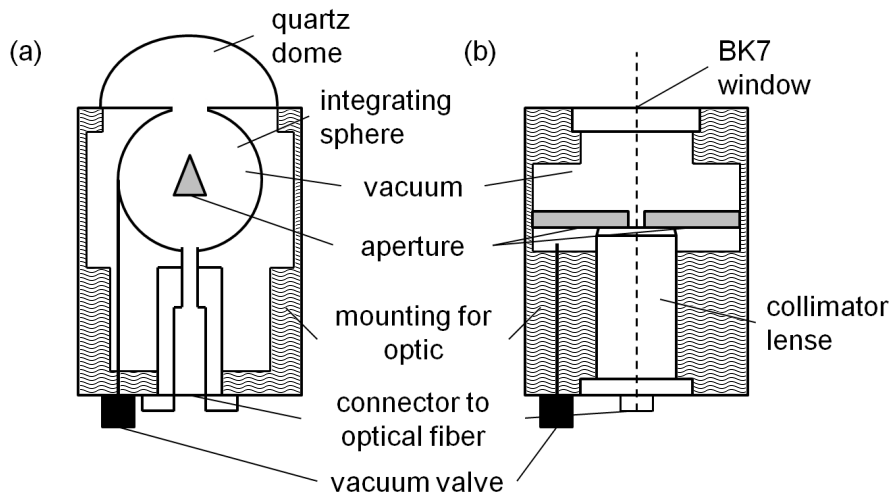


Figure 3.5: Sketch of (a) irradiance and (b) radiance inlet.

which is plugged between optical fiber and the SWIR spectrometer.

Because of limitations in the transmissivity of the optical fibers, the sensitivity of the PDA and the characteristics of the calibration lamp, reliable data can only be obtained in the wavelength region $\lambda = 350 - 2000$ nm. The spectrometer system and the computer are mounted in a rack which can be placed in a ventilated aluminum box to protect from rain and direct solar radiation.

The field-of-view of the radiance inlet, the integration time t_{int} , the speed over ground (SOG) of the ship and the distance between optical inlet and cloud determines the footprint of the radiance measurements. As a result different footprints are obtained for different cross-track (d_c) and along-track (d_a) orientations. The viewing geometry of the radiance inlet is illustrated in Figure 3.6a. Using basic trigonometry the diameter of the cross-track footprint d_c can be calculated with:

$$d_c = 2 \cdot h_c \cdot \arctan \frac{\Delta}{2}. \quad (3.1)$$

d_c is calculated for typical configurations during OCEANET with an opening angle $\Delta = 2^\circ$ and for different cloud altitudes h_c (Figure 3.6b). d_c increases linearly with altitude. For typical marine boundary layer clouds in 1000 – 2000 m altitude, d_c varies between 30 – 70 m, whereas for an altitude of a cirrus cloud in 10 km d_c reaches values up to 365 m. For a moving ship, additionally the along-track footprint d_a have to be considered, which results from the SOG and t_{int} of the radiance measurements. d_a was calculated and illustrated in Figure 3.6c for different (typical) measurements. The resulting range of d_a values varies between 2.5 – 23 m.

3.2.1 Radiometric Calibration

A number of calibration procedures are required and applied to the raw signal to derive physical radiation quantities from the CORAS measurements.

A wavelength calibration is necessary to assign the PDA-pixels to respective wavelengths. The wavelength is determined by the grating of EM radiation of the spectrometer. For calibration noble-gas emission lamps (Neon, Argon, Krypton, Mercury, Mercury-Argon) with a well-defined spectrum of emission lines are used. These emission lines are assigned to a pixel number which corresponds to the maximum of a fourth-order Gauss fit. The width of these Gauss curves determines the *FWHM* of each emission line. To cover the entire spectrometer wavelength/pixel region each pixel is assigned to corresponding wavelengths using a polynomial fit over all relevant wavelengths. An overview of the emission lines of the various lamps is given in Table 3.2.

To transfer the measured digital signal $G(\lambda)$ of CORAS into quantitative values of spectral radiance and irradiance a spectral calibration with a certified source of diffuse radiation is required. A certified 1000 W irradiance standard in combination with a certified reflectance panel was applied to calibrate the radiance inlet for wavelengths $\lambda \leq 380$ nm. The calibration setup is illustrated in Figure 3.7a. To reduce stray light (resulting from reflections on other

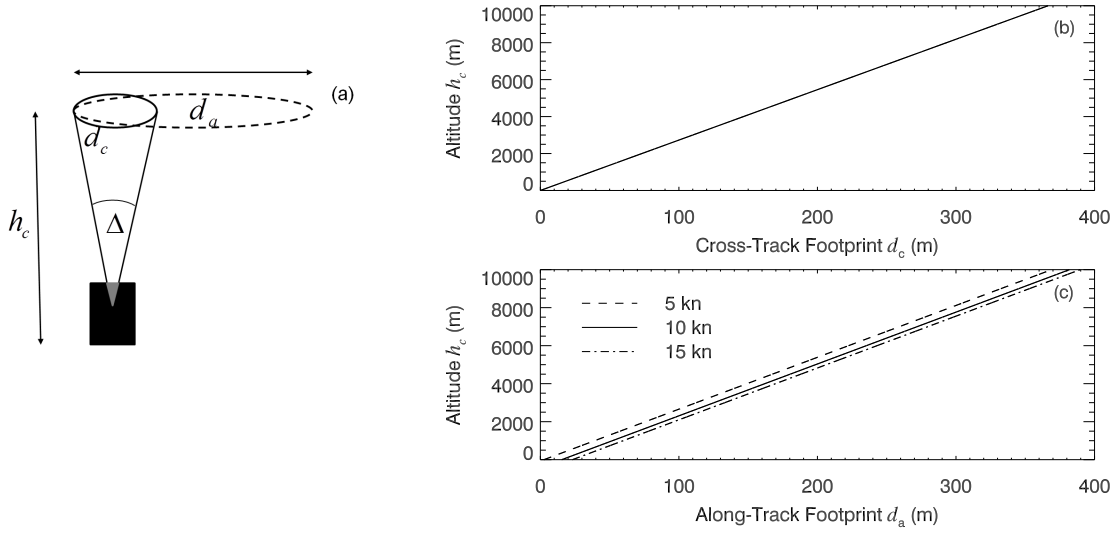


Figure 3.6: (a) Illustration of the viewing geometry of the radiance inlet. (b) Cross-track footprint diameter d_c in dependence of the cloud altitude h_c for the radiance measurements with an opening angle of 2° . (c) Along-track footprint diameter $d_a + d_c$ in dependence of the cloud altitude h_c for the radiance measurements for different measurement cases which are representative for the OCEANET-transects. Cases 1–3 corresponds to measurements with ship speeds over ground (SOG) of SOG=5, 10, 15 kn and maximum integration time $t_{\text{int}} = 1000, 3000, 3000$ ms, respectively. Case 2 was the prevailing measurement situation.

surfaces), the measurement setup was placed inside a ventilated, black metallic box. The 1000 W irradiance standard emits defined irradiance $F_{\lambda,L}$ which is reflected by a reflectance panel (manufactured by *Gigahertz-Optik, GmbH*) made of Spectralon[®]. The panel reflectivity $R_P(\lambda)$ is certified by an independent calibration traceable to the US National Institute of Standards and Technology (NIST) standards. According to the calibration certificate, an angle between the panel surface and the incident $F_{\lambda,L}$ normal of 8° is required. $F_{\lambda,L}$ is certificated for the distance $l_0 = 50$ cm but for practical reasons the distance between the lamp and the panel was set to $l = 53.9$ cm. The reflected radiation from the panel is measured from the radiance inlet. The absolute calibration factor $C_{\lambda,P}$ from this setup is determined by:

Table 3.2: Spectral emission lines (nm) of different noble-gas lamps used for the wavelength calibration. Lamps used are Neon (Ne), Argon (Ar), Krypton (Kr), Mercury (Hg) and Mercury-Argon (HgAr).

Element	Emission Line (nm)
Ne	621.73; 692.95; 1291.20; 1321.92; 1523.07
Ar	727.29; 763.51; 826.45; 866.79; 922.45; 965.78; 1694.52; 1782.89
Kr	1125.80; 1286.19; 1442.68; 1568.10; 1582.01; 1709.88; 1761.69; 1800.22; 2116.55
Hg	350.02; 404.66; 435.83
HgAr	1014.25; 1530.00

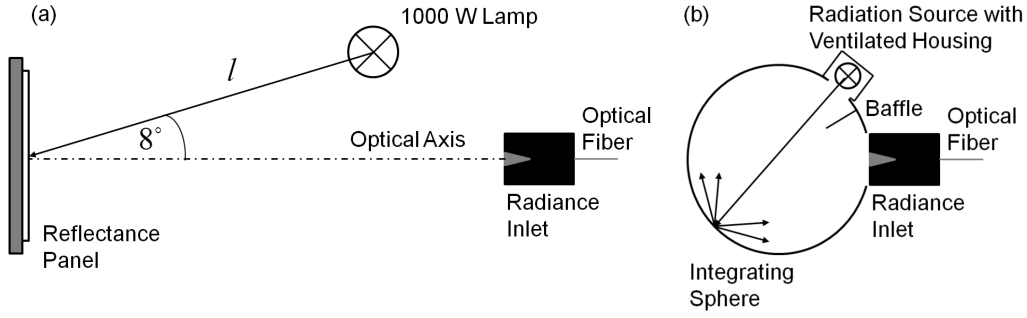


Figure 3.7: Absolute radiometric calibration setup for the radiance inlet using (a) reflectance panel and (b) an integrating sphere.

$$C_{\lambda,P} = \frac{l^2}{l_0^2} \cdot \frac{F_{\lambda,L} \cdot R_P(\lambda)}{\pi} \cdot \frac{1}{G(\lambda)}. \quad (3.2)$$

The calibration setup for wavelengths $\lambda \geq 380$ nm is illustrated in Figure 3.7b. A certified integrating sphere (manufactured by *Gigahertz-Optik, GmbH*; model UMBB-500) which emits defined diffuse radiances $I_{\lambda,S}$ was used for the calibration. Within the integrating sphere the spectral radiation of a source lamp is reflected on the inside of the sphere. This is coated with barium sulfate acting as Lambertian reflector. The radiance inlet is placed in front of the exit aperture of the sphere and measures the spectral diffuse radiance $I_{\lambda,S}$. To avoid the contribution of direct (non-diffuse) radiance, a baffle is placed inside the sphere. $I_{\lambda,S}$ is certified by external calibration traceable to standards of the German Calibration Service (DKD). The absolute calibration factor $C_{\lambda,S}$ using the integrating sphere is given as follows:

$$C_{\lambda,S} = \frac{I_{\lambda,S}}{G(\lambda)}. \quad (3.3)$$

The comparison of $C_{\lambda,P}$ and $C_{\lambda,S}$ obtained from the VNIR spectrometer for OCEANET is presented in Figure 3.8a. Both calibration factors have a strong spectral dependence resulting from the spectrometer characteristics, the spectral pattern of the radiation sources, as well as radiation absorption within the optical fibers and the BK 7 glass implemented in the radiance inlet. Because the integrating sphere emits radiation at wavelengths $\lambda \geq 380$ nm only, $C_{\lambda,S}$ increases significantly for short wavelengths. A discrepancy of $C_{\lambda,P}$ and $C_{\lambda,S}$ is obvious for wavelengths $\lambda > 700$ nm due to the influence of stray light in the calibration setup with the panel. For that reason, $C_{\lambda,P}$ was not used for wavelengths $\lambda > 700$ nm. Both calibration factors agree within 4% in the wavelength region $\lambda = 400 - 700$ nm. For the stated reasons, the absolute calibration factor for the VNIR spectrometer was merged from both methods using $C_{\lambda,P}$ for $\lambda \leq 420$ nm and $C_{\lambda,S}$ for $\lambda > 420$ nm.

The absolute calibration factor $C_{\lambda,S}$ for the SWIR spectrometer obtained from two different integration times t_{int} used during OCEANET is shown in Figure 3.8b. In contrast to the VNIR spectrometer, $C_{\lambda,S}$ depends on t_{int} , which is illustrated in the lower panel of Figure 3.8b. Here, the ratio of derived $C_{\lambda,S}$ at $t_{\text{int}} = 300$ ms (black line) and $C_{\lambda,S}$ at $t_{\text{int}} = 500$ ms

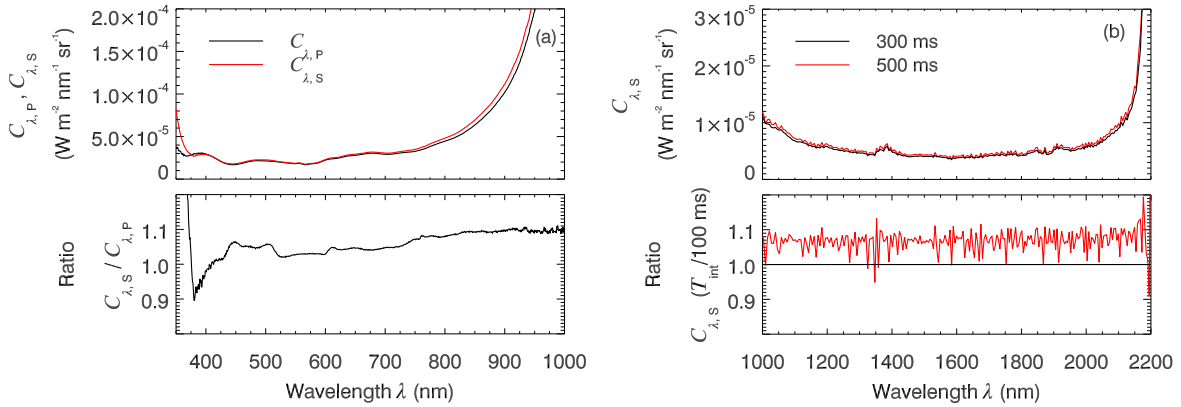


Figure 3.8: Absolute calibration factors for the radiance measurements for (a) the VNIR spectrometer obtained from the calibration setup using the reflectance panel $C_{\lambda,P}$ and the calibration setup using the integrating sphere $C_{\lambda,S}$, and (b) the SWIR spectrometer obtained from different integration time measurements ($t_{\text{int}} = 300$ ms, 500 ms) using $C_{\lambda,S}$ from the integrating sphere.

(red line) to $C_{\lambda,S}$ at $t_{\text{int}} = 300$ ms is plotted. With increasing t_{int} this ratio increases and results in more pronounced peaks due to the non-linear dark signal dependence on t_{int} in the SWIR spectrometer (Bierwirth, 2008). For that purpose it is necessary to determine a calibration factor $C_{\lambda,S}$ using Eq. (3.3) for each t_{int} used in the field experiment.

When CORAS is transported and installed on the ship it is necessary to disconnect the optical fibers from the spectrometer and the optical inlets. With each reconnection the transmission properties between the spectrometer and the optical fibers change compared to the calibration in the laboratory. The identical connection and alignment of the optical fibers is not perfectly reproducible. To consider these changes in the sensitivity of the CORAS system a transfer calibration with a small portable barium-sulfate coated integrating sphere (made by *LOT-Oriel GmbH*) has to be performed. The sphere provides a constant source of radiation. The transfer calibration with the portable integrating sphere was performed in the laboratory during the absolute calibration to measure the output of the sphere (G_{lab}), and after the reconnection of the fibers in the field during OCEANET (G_{field}) to determine the spectral differences during both calibrations. The transfer calibration factor $C_{\lambda,T}$ is defined as the ratio of the net signal during absolute laboratory calibration to the net signal in the field by:

$$C_{\lambda,T} = \frac{G_{\text{lab}}(\lambda)}{G_{\text{field}}(\lambda)}. \quad (3.4)$$

The field calibration with the portable integrating sphere was performed as often as possible during OCEANET. Examples of $C_{\lambda,T}$ during ANT-XXVIII/5 are presented in Figure 3.9 for the VNIR and SWIR spectrometer. $C_{\lambda,T}$ for the VNIR spectrometer reveals a significant spectral behavior over the wavelength region. For most measurement examples $C_{\lambda,T}$ is lower than unity which means that the transmission and thus $G_{\text{field}}(\lambda)$, was larger than the digital signal in the laboratory $G_{\text{lab}}(\lambda)$. But especially near the tropics (see example from April 27 and May 1 2012), where temperatures and relative humidity increases, the opposite is true,

which emphasizes a frequently determination of transfer calibration factors. The reason for this are the variable meteorological conditions in different climate zones. The spectrometer signal $G_{\text{field}}(\lambda)$ and the dark current signal (which has to be subtracted to obtain the net signal) are temperature–dependent. For example, the dark current obtained from dark field calibration measurements in the tropics reveals on average 950 counts whereas in the mid–latitudes (comparable to laboratory conditions) 400 counts were measured. In the VNIR $C_{\lambda,T}$ varies dependent on wavelength between 0.95 and 1.15. Whereas for the SWIR spectrometer the temporal variability of $C_{\lambda,T}$ is reduced and values range between 0.98 and 1.05. Here, absorption bands of water vapor are removed and $C_{\lambda,T}$ is set to a constant value around these bands.

Finally, the measured digital signal $G_{\text{meas}}(\lambda)$ during OCEANET is converted into values of I_{λ}^{\downarrow} by multiplying the absolute and transfer calibration factors obtained from different calibration setups as follows:

$$I_{\lambda}^{\downarrow} = G_{\text{meas}}(\lambda) \cdot C_{\lambda,P/S} \cdot C_{\lambda,T}. \quad (3.5)$$

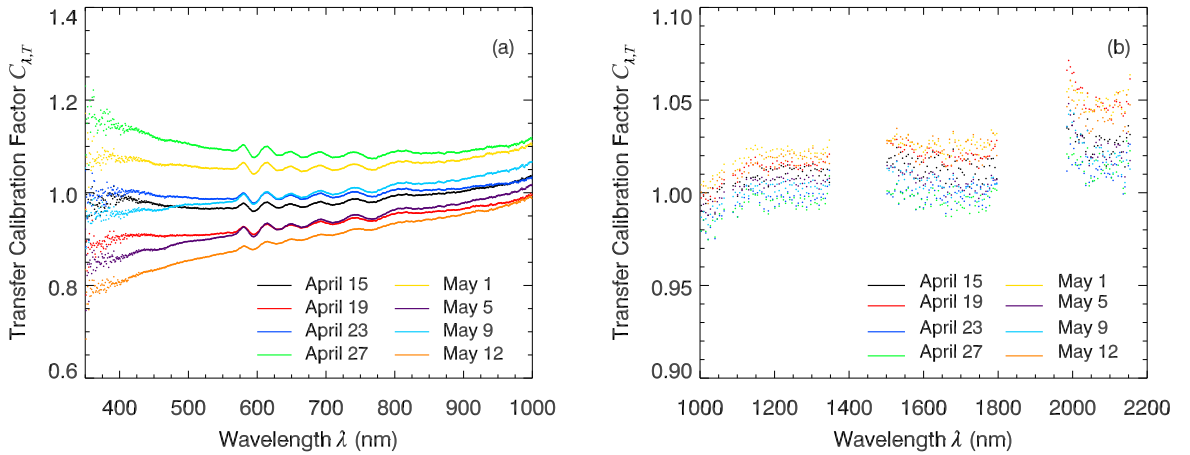


Figure 3.9: Transfer calibration factors $C_{\lambda,T}$ for the radiance measurements for (a) the VNIR spectrometer, and (b) the SWIR spectrometer obtained from the portable integrating sphere for different measurement examples during ANT–XXVIII/5.

3.2.2 Measurement Uncertainties

The uncertainty of the CORAS measurements is dominated by the contribution of the different calibrations. The relevant measurement uncertainties are the uncertainties in the spectrometer signal, the absolute calibration and transfer calibration. The composite relative uncertainty is determined with Gaussian error propagation with the assumption that the individual measurement assumptions are random and, therefore, independent of each other.

The wavelength–dependent measurement uncertainties, as well as the uncertainty of the ratios used in this work, are given in Table 3.3. The uncertainty of the spectrometer signal

Table 3.3: Measurement uncertainty in certain spectral wavelength regions and ratios.

Wavelength (nm)	Spectrometer signal	Absolute calibration	Transfer calibration	Total
350–420	5.7%	5.1%	11.5%	13.8%
420–800	0.5%	5%	0.7%	5.1%
800–1550	1.8%	8%	0.5%	8.2%
1550–1800	2.2%	9%	1.1%	9.3%
1800–2200	18.7%	10%	1.9%	21.3%
450/680	0.5%	–	–	0.5%
1050/1250	1.8%	–	–	1.8%
1670/1560	2.2%	–	–	2.2%

includes the signal-to-noise ratio of the spectrometers and the uncertainties in the wavelength calibration (Bierwirth, 2008). The uncertainty of the wavelength accuracy of $< 1\%$ is determined by the *FWHM*. The standard deviation of the dark signal in the VNIR and SWIR spectrometer determines the signal-to-noise ratio. Usually, the measured digital signal in the wavelength region $\lambda = 200 - 300$ nm (no photons should be detected) is used as an estimate of the dark signal in the VNIR spectrometer wavelength region. The wavelength dependence of the dark signal in the SWIR spectrometer is known, since the dark signal of the spectrometer is the digital signal with the plugged shutter in the optical path. For most wavelengths covered from the spectrometers the uncertainty in the spectrometer signal amounts to 0.5–2.2%, but for wavelengths $\lambda \leq 420$ nm and $\lambda \geq 2000$ nm the uncertainty increases due to the reduced sensitivity of the spectrometers. For wavelengths $\lambda \leq 420$ nm absolute calibration uncertainties results from the reflectance panel and the 1000 W irradiance standards with calibration uncertainties certified by the manufacturer with 0.8% and 5%, respectively. The uncertainty in the transfer calibration is obtained from the standard deviation of the calibration factors obtained in the field or the respective cruise transects. The uncertainty of the transfer calibration is about 1%, except for wavelengths $\lambda \leq 420$ nm, where the low output of the integrating sphere is related with larger uncertainties (11.5%). Using ratios of spectral radiance (or transmissivity) in certain wavelength regions reduces the measurement uncertainty. Only the statistical uncertainty of the spectrometer signal of 0.5%, 1.8%, and 2.2% of the three ratios used for the new retrieval method contributes to the overall measurement uncertainty. The ratio wavelength combinations are 450 nm/680 nm, 1050 nm/1250 nm, and 1670 nm/1560 nm, which are introduced in Section 4.3.2 in detail. The contribution of the wavelength accuracy of $< 1\%$ was neglected in this work.

3.2.3 Horizontal Misalignment

Since the ship movements do not allow for perfect zenith observations an active horizontal stabilization platform would be desirable (Brückner et al., 2014). The movement of the ship causes deviations of the sensor detection plane from the horizontal reference plane of the Earth-fixed coordinate plane. The geometry for the relation between the Earth-fixed plane and the sensor reference plane is illustrated in Figure 3.10a. This is crucial for irradiance

measurements but less crucial for radiance observations (Wendisch et al., 2001). Therefore, it is reasonable to just exclude all radiance data with a horizontal misalignment larger than 5° and to avoid a leveling platform. To separate the measurements, according to the respective horizontal misalignment $\Delta\theta = \theta_0 - \theta'_0$, the ship solar zenith angle θ'_0 was calculated using the solar azimuth angle ϕ_0 and the heading h of the ship (Saunders et al., 1992):

$$\begin{aligned} \cos \theta'_0 = & -\cos \alpha \cdot \sin \beta \cdot \sin \theta_0 \cdot \cos(\phi_0 - h) \\ & -\sin \alpha \cdot \sin \theta_0 \cdot \sin(\phi_0 - h) \\ & +\cos \alpha \cdot \cos \beta \cdot \cos \theta_0, \end{aligned} \quad (3.6)$$

with the solar zenith angle θ_0 and the roll α and pitch β angles of the ship. An example of the measured roll/pitch and heading angles from the ship inertial navigation system (INS) from 17 April 2012 is presented in Figure 3.10b. According to the time resolution of the CORAS measurements the data were low-pass filtered to a time resolution of 15 s. This example illustrates a relatively calm sea, as the roll/pitch angles ranges between $-1.5-1^\circ$ and $0-0.5^\circ$. For a rough sea these deviations can be up to $\pm 3^\circ$ which results in a horizontal misalignment $\Delta\theta = \theta_0 - \theta'_0$ of up to 9.3° . Those data were excluded from the data analysis presented in this work. The laser navigation platform (Marine Inertial Navigation System MINS) provides data of headings as well as roll/pitch. The ship's center is the reference position. Data are provided with a 1 s resolution and an accuracy of currently ± 5 m. The deviation from the zenith direction was originally introduced to airborne pyranometer measurements (e.g., Bannehr and Glover, 1991; Saunders et al., 1992; Boers et al., 1998b); it is applied to ship measurements here.

Bannehr and Schwiesow (1993) found that, in addition to the attitude deviation considering the above maintained horizontal misalignment resulting from the ship movement, it is important to determine the precise angles between the optical inlets reference plane and the INS reference plane. Eq. (3.7) holds when roll/pitch from the sensor plane equals the roll/pitch from the ship INS. The basic idea of this retrieval algorithm is that the irradiance incident on the sensor is kept constant under clear skies and at fixed altitudes. Therefore, it is independent of the direction of the course of the ship and only trends are expected due to changes in solar altitude. Applying a correction factor g_{corr} , which is valid under clear sky conditions (direct component only) to the radiation data only accounts for the geometrical not for physical misalignment. The correction factor g_{corr} is given as follows (Bannehr and Schwiesow, 1993):

$$g_{\text{corr}} = \frac{\sin h_0}{\cos h_0 \sin \alpha \sin(\phi_0 - h) - \cos h_0 \sin \beta \cos \alpha \cos(\phi_0 - h) + \sin h_0 \cos \beta \cos \alpha}, \quad (3.7)$$

where h_0 is the solar altitude. Here, the observed irradiance data were used to obtain the deviation from the sensor plane.

The retrieval of the offset angles $\Delta\alpha$ and $\Delta\beta$ of the sensor plane (due to installation require-

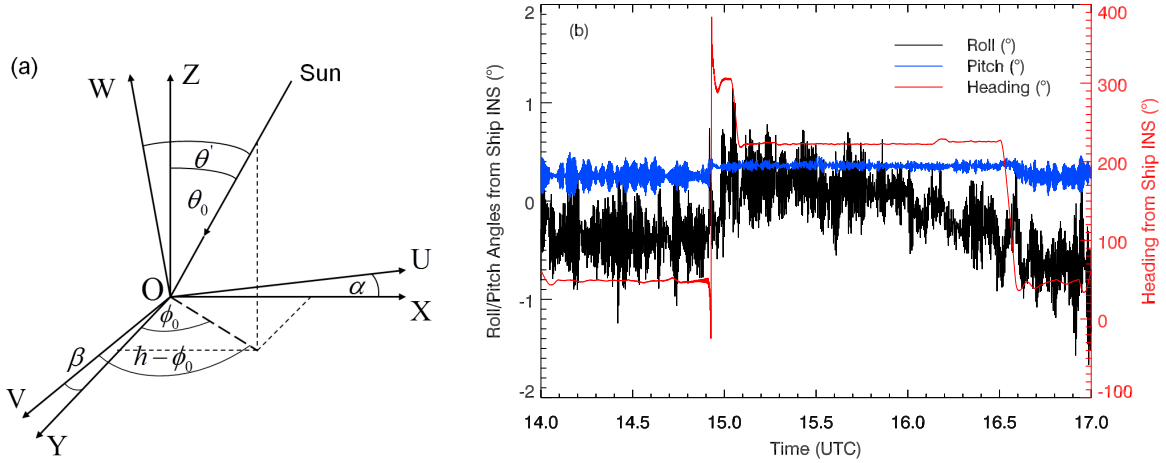


Figure 3.10: (a) Geometry for the relation between the Earth-fixed coordinate plane and the sensor reference coordinate plane. (b) Time series of roll/pitch and heading angles from the ship inertial navigation system (INS) from April 17 2012 from ANT-XXVIII/5. Data are low-pass filtered to a time resolution of 15 s.

ments) were retrieved with an algorithm by Bannehr and Schwiesow (1993) as follows: in the beginning of the iteration, $n = 0$, no installation errors, that is $\Delta\alpha/\Delta\beta = 0$, are assumed. First, the correction factor $g_{\text{corr}}(n)$ using Eq. (3.7) including the offset angles $\alpha + \Delta\alpha$ and $\beta + \Delta\beta$ is derived and applied to the calibrated irradiance data from CORAS. Second, the corrected time series is low-pass filtered to determine trends caused by changing h_0 . This removes high frequently fluctuations in the time series. In a third step, the residual is determined while subtracting the low-pass filtered time series from the unfiltered time series. Forth, the standard deviation of the residual time series is calculated. While keeping $\Delta\beta(n)$ constant, $\Delta\alpha(n)$ is found by searching iteratively for the minimum standard deviation of the residual time series. In a last step, the new $\Delta\alpha_{\text{new}}(n) = \alpha_{\text{old}} + \Delta\alpha(n)$ is used as a new input parameter in step $n = 1$. Steps $n = 1 - 5$ are repeated until $|\Delta\alpha_n - \Delta\alpha_{n+1}| < 0.05^\circ$. The same procedure is used to determine $\Delta\beta_{\text{new}}$, while applying the retrieved $\Delta\alpha_{\text{new}}$. The offset angles were added to the roll and pitch angles in Eq. (3.7).

Usually, the convergence criteria is achieved after a few iteration steps. The result of the retrieved $\Delta\alpha$ and $\Delta\beta$ offset angles for the three Atlantic cruises are listed in Table 3.4. The procedure was applied to a few time series (under clear sky conditions) of one cruise but the results varies only in the range of 0.05° and thus are considered to be constant for the respective cruise leg.

Table 3.4: Retrieved sensor offset angles $\Delta\alpha$ and $\Delta\beta$ for the three Atlantic transfer cruises.

Cruise leg	offset angles	
	$\Delta\alpha$	$\Delta\beta$
ANT-XXVII/4	2.1°	0.3°
ANT-XXVIII/5	1.8°	0.5°
ANT-XXIX/1	1.6°	0.7°

3.3 Instrumentation of the OCEANET-Container

OCEANET–Atmosphere is a collaborative project in the framework of the German Leibniz–program which investigates the mass and energy exchange between the ocean and the atmosphere (Macke et al., 2010). A measurement container was designed to operate on research and freight vessels and which covers a wide range of atmospheric measurements.

A sketch of the OCEANET–Atmosphere container is illustrated in Figure 3.11a. Figure 3.11b shows the container on the monkey deck of RV *Polarstern* with the installed instruments on the roof of the container during ANT–XXVII/4. The measurement container combines latest measurement techniques and records the data with an internal computer network. It represents an autonomous platform for atmospheric profiling which can operate on ships and land. After the loading only a few hours are required to install all instruments for operation usage. The frontal part contains the microwave radiometer with a hatch on the roof and additional upward looking devices. A lidar and data acquisition devices are placed in the weather protected back part of the container.

To obtain standard meteorological data a Scalable Automatic Weather Station SCAWS (El Nagggar and Macke, 2010) was developed at the German Weather Service (DWD). Data of wind, pressure, temperature, humidity, position as well as solar and terrestrial downward

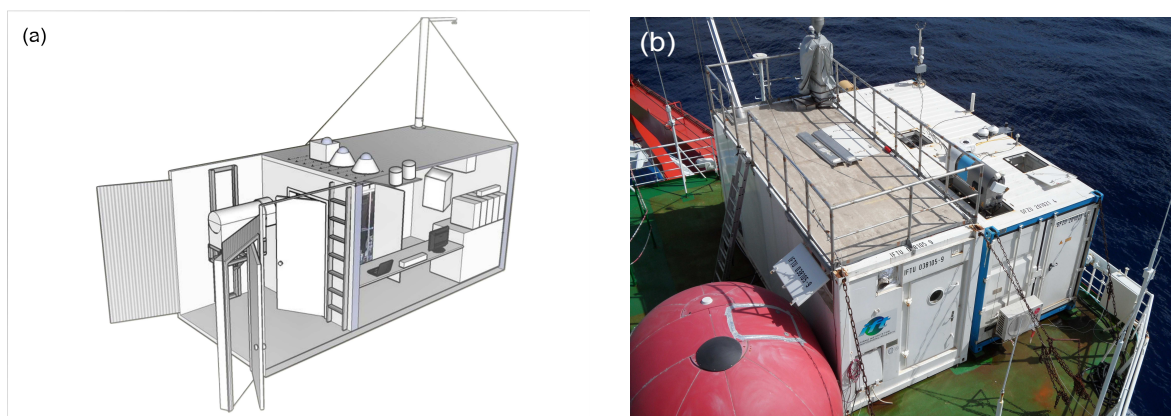


Figure 3.11: (a) Sketch of the OCEANET–Atmosphere container and (b) photograph of the container (right: OCEANET–Atmosphere, left: Aerosol container from TROPOS) with installed instruments on the roof on the 20 m high monkey deck of RV *Polarstern* during ANT–XXVII/4.

radiation (SDR, TDR) are taken every second. Via telemetry selected packets are transmitted to a satellite as a *FM-13 Ship-Message*. These standard measurements are realized according to DIN (Deutsches Institut für Normung) standards for certified measurement devices from DWD. Since ANT-XXVI/1 (2007) OCEANET-Atmosphere is an officially listed sea weather station, it is subject to regular service and quality management of standard measurements by DWD.

SDR and TDR are measured with a *Kipp & Zonen CM21* pyranometer and a *Kipp & Zonen CG4* pyrgeometer. The *Kipp & Zonen CM21* is a secondary standard pyranometer according to ISO 9060 (International Organization for Standardization). It covers the spectral region $\lambda = 305 - 2800$ nm with a response time (95%) of 5 s. The manufacturer estimate a maximum error of 2% for hourly sums and due to the movement of the ship a negative bias of 2% for daily sums of incoming solar radiation (Kipp & Zonen, 2004). The pyrgeometer covers the spectral region $\lambda = 4.5 - 42$ μm measuring the broadband terrestrial radiation with a response time (95%) of 25 s (Kipp & Zonen, 2001). The manufacturer expects, due to solar heating of the instruments silicon window, a maximum error of $+4$ Wm^{-2} during an isolation of 1000 Wm^{-2} which results in an accuracy of 3% for daily sums of TDR (Kipp & Zonen, 2001). Both instruments measure the upper hemisphere with a 180° viewing angle; the angular response corresponds to cosine response (Kipp & Zonen, 2004).

A full-sky imager developed at the Helmholtz Centre for Ocean Research Kiel GEOMAR (Kalisch and Macke, 2008) determines cloud cover as well as cloud type (Heinle et al., 2010). During day time one picture of the upper hemisphere is taken every 15 seconds. A digital charged-coupled device (CCD) camera equipped with a fish eye lens is the main component. The full-sky imager operates without a shading of the lens. From the full sky images the total cloud cover was deduced. An automatic classification of the images introduced by Heinle et al. (2010) discriminates between seven categories based on the synoptic cloud key for weather observations as well as visual properties of the pictures.

Turbulent fluxes of latent and sensible heat are measured with an Ultrasonic-Anemometer (METEK USA-1) for wind measurements with 10 Hz in combination with a fast responding hygrometer (LICOR 7500) for humidity measurements with 30 Hz temporal resolution (Bumke et al., 2014). Furthermore, additional data are measured outside of the container. The aerosol optical thickness is derived from MICROTOPS sun photometer (see Section 3.1). The cloud base height is determined with a ceilometer. Until October 2011 the cloud ceilometer LD-WHX05 manufactured by *Impulsphysik Germany* with a maximum range of up to 12,000 ft was used. For clear sky above the vertically pointing instrument a larger constant value is set. Since October 2011 a ceilometer CL51 manufactured by *Vaisala Finland* with a higher range up to 43,000 ft operates on the ship which enables also the detection of cirrus clouds. The manufacturer reports that the ceilometer is able to detect three cloud layers simultaneously and provides backscatter profiles over the full measurement range (Vaisala, 2010).

Inside of the container a portable multi-wavelength Raman and polarization lidar system Polly^{XT} developed at TROPOS is placed. It was designed to perform automated and remote lidar measurements (Althausen et al., 2009). Three wavelength laser pulses ($\lambda = 355, 532, 1064$ nm) are used to obtain vertical profiles of particle backscatter and ex-

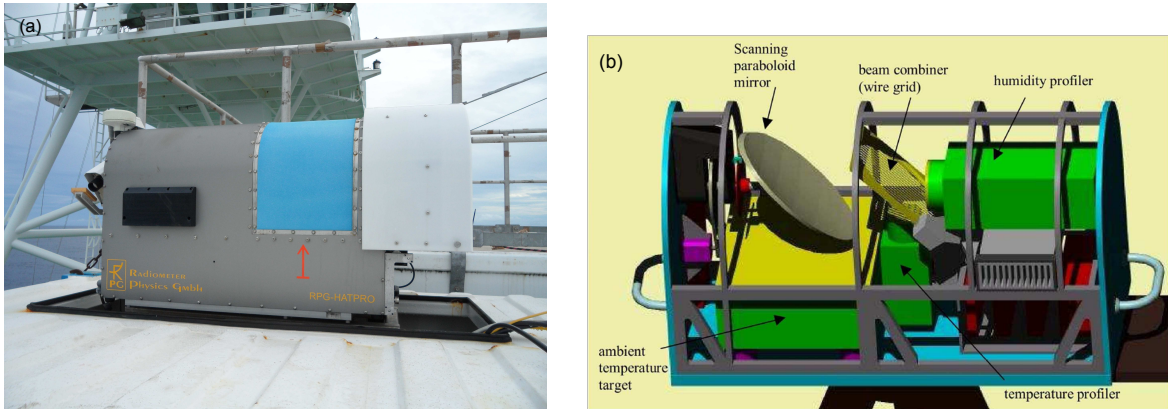


Figure 3.12: (a) RPG–HATPRO on the roof of the OCEANET–Atmosphere container on RV *Polarstern*. (b) Sketch of schematic setup of HATPRO adopted from Rose and Czekala (2008).

inction coefficients. Additionally, the volume depolarization ratio is determined and used to discriminate cloud layers with ice crystal backscattering (Seifert et al., 2010). To avoid specular reflection caused by horizontally oriented ice plates the laser beams are tilted by 5° off zenith angle. Cloud observation with a lidar are limited to clouds with $\tau < 2.5$ in the VIS wavelength region (Kanitz et al., 2011). Therefore, lidar data can only be used for those clouds which are optically thin. In this case, in addition to the cloud base height, also the cloud top height can be measured. The lidar provides high temporal and spatial vertical profiles of aerosol particle distribution in the atmosphere.

The microwave radiometer Humidity And Temperature PROfiler (RPG–HATPRO) was developed by *Radiometer Physics Germany* (see Figure 3.12). With 14 frequency channels it enables to continuously measure vertical profiles of temperature and humidity as well as column amounts of integrated water vapor (*IWV*) and *LWP* (Rose et al., 2005). Figure 3.12b illustrates the schematic setup of HATPRO (Rose and Czekala, 2008). A pivoted parabolic mirror bundles the incoming radiation and is transmitted to a wire grid. From that, one part is horizontally polarized for the humidity profiler while the other part is vertically polarized for the temperature profiler. Czekala et al. (2001) found that both profiler receive the same portion of radiation when there is no precipitation in the viewing angle of the radiometer. When precipitation wets the HATPRO radome the emission by liquid water droplets prevents meaningful observations. A rain sensor (as follows named rain flag) is used to separate the rain data from non–precipitating clouds. In an ideal case, rain sensor and radiometer cover panel dry likewise fast, so that these data can be easily sorted out. For calibration purpose an ambient temperature target is installed underneath the mirror. The opening angle of the system for the water vapor and oxygen frequencies is 3.5° and 2.5° , respectively. Thus, the resulting spatial resolution depends on cloud height and varies between 60 m up to several hundred meter.

Figure 3.13 presents the spectral extinction coefficients in the microwave region for a cloudy atmosphere with the single contribution from liquid cloud droplets, water vapor and oxygen (Crewell et al., 2001). Because scattering can be neglected absorption equals extinction. The

transition from different rotational states of gas molecules cause two pronounced absorption features which results in two main well defined absorptions lines in certain frequency regions. Absorption bands of water vapor (22.235 GHz) and oxygen (around 60 GHz) have a direct impact on the extinction profile of the cloudy atmosphere. HATPRO measures in these regions which are indicated with A and B in Figure 3.13. The *IWV* is obtained from the strength of the absorption line A, while water vapor profiles are derived from the broadening along the absorption line A and *LWP* from the increased absorption with increasing frequency. Temperature is profiled from multi-channel measurements along the oxygen absorption region B.

A modified version (Zoll, 2008) of the algorithm introduced by Crewell and Löhnert (2003) is used to determine vertical profiles of *IWV* and *LWP* from brightness temperatures (BT). The algorithms are based on synthetic observations generated from a representative long-term radiosonde data set (Löhnert and Crewell, 2003). The input radiosonde data set consists of profiles of temperature, humidity and pressure. Based on this data set, the liquid water content (*LWC*) is calculated using a modified adiabatic cloud model, while the cloud boundaries are determined by a 95% humidity threshold (Karstens et al., 1994). For the statistical retrieval algorithm, the radiosonde data set is divided into a training and test data set. From the training data set, synthetic BTs at the ground are calculated with a radiative transfer model. The statistical retrieval algorithm is derived with a multi-linear regression. Applying this algorithm to the test data set yields the retrieval quality and theoretical retrieval error. The accuracy of the *LWP* retrievals is about 25 g m^{-2} (Löhnert and Crewell, 2003). The most frequent source of radiometer uncertainties are calibration errors. Therefore, HATPRO applies several calibration methods. An absolute calibration is performed by a cooled liquid nitrogen target in combination with a temperature stabilized target inside the radiometer. A secondary calibration include a noise-diode which can be shifted to the receiver inputs and a gain calibration. Additionally, a tipping curve calibration is used for channels with low opacity. This method is valid for homogenous clear sky conditions. Except the absolute calibration, which has to be done manually in the harbor before the OCEANET campaigns, all calibration methods are performed automatically.

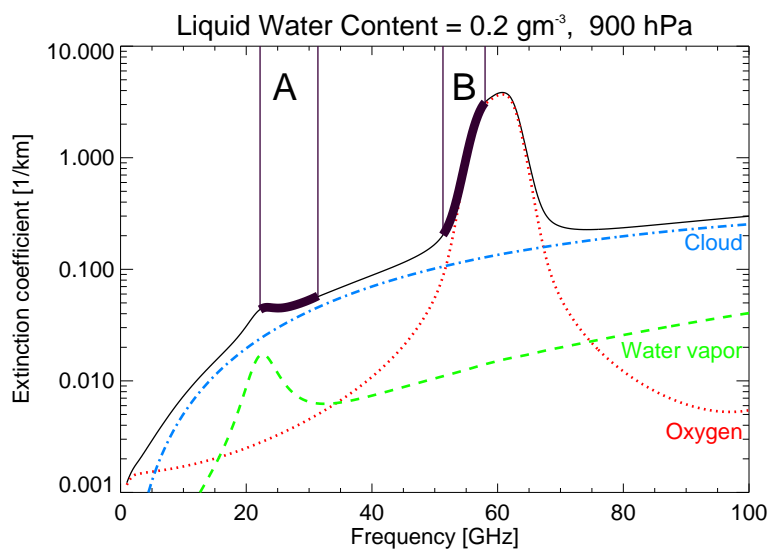


Figure 3.13: Spectral extinction coefficients over the microwave region for cloudy atmosphere with single contributions from liquid water cloud droplets assuming a liquid water content (LWC) of 0.2 g m^{-3} (blue line), water vapor (green line), and oxygen (red line). The black lines represents the contributions of all components. HATPRO frequency regions are illustrated with A and B. Graphic was adopted from Pospichal (2009).

4 Remote Sensing and Multi-Wavelength Cloud Retrieval

In this chapter a new methodology to retrieve optical and microphysical properties of marine clouds over the ocean is introduced. A description of the radiative transfer simulations in combination with the measurements is introduced in Section 4.1. In Section 4.2 it is explained how τ and r_{eff} of marine clouds are derived from these simulations by existing standard two-wavelength (2-WL) retrievals (Section 4.2.1) and a spectral slope retrieval (Section 4.2.2). To overcome problems of those retrieval methods a new multi-wavelength cloud retrieval method is presented in Section 4.3. Parts of this chapter were published by Brückner et al. (2014).

4.1 Simulations

4.1.1 Radiative Transfer Model

To retrieve microphysical properties from spectral radiation measurements simulated radiances are required over ranges of τ , r_{eff} and solar zenith angles θ_0 to calculate lookup tables (LUT). The plane-parallel radiative transfer model package *libRadtran* version 1.6beta (Mayer and Kylling, 2005; Mayer, 2009) was used to calculate the zenith radiance $I_{\lambda, \text{mod}}^{\downarrow}$ at sea level z_0 . The simulations were performed with the discrete ordinate radiative transfer solver (DISORT version 2.0) by Stamnes et al. (1988) with 16 streams. The molecular absorption parametrization was adopted from LOWTRAN/SBDART^a by Ricchiazzi et al. (1998). The intensity-correction method described by Buras et al. (2011) was used which employs the scattering phase function directly. This method is faster as the intensity-correction method introduced by Nakajima and Tanaka (1988) and represents strong forward-scattering by large hydrometeors with high accuracy (Buras et al., 2011). The vertical profiles of meteorological parameters were adopted from standard profiles of Anderson et al. (1986) (either tropical, mid-latitude summer or mid-latitude winter), modified with daily temperature and relative humidity measurements obtained from radio sounding made on RV *Polarstern*. The extraterrestrial spectral irradiance data $F^{\downarrow}(\text{TOA})$ were taken from Gueymard (2004). The radiative transfer calculations assumed a spectral ocean surface albedo (Loveland and Belward, 1997, type ocean-water). A maritime aerosol type from Shettle (1989) was chosen. A liquid water (situated in 2 – 4 km) or ice cloud (situated in 7 – 8 km) with different values of τ and r_{eff} was introduced into the model input. The liquid water content LWC in g m^{-3} was approximated with a formula proposed by Chylek (1977):

^aLow-Resolution Spectral Transmission/Santa Barbara DISORT Atmospheric Radiative Transfer

$$LWC = \frac{2\rho}{3} \cdot b_{\text{ext}} \cdot r_{\text{eff,input}}, \quad (4.1)$$

where ρ is the water density. The extinction coefficient was approximated with $b_{\text{ext}} = \tau_{\text{input}}/dz(z_1, z_2)$. dz is the sum of z_1 (cloud base height) and z_2 (assumed geometrical thickness of the cloud).

For the water cloud τ was varied from 1 to 80 with $\Delta\tau = 1$; for the ice cloud τ varied from 0.1 to 10 in steps of 0.1, respectively. r_{eff} was varied from $1 \mu\text{m}$ to $30 \mu\text{m}$ in steps of $1 \mu\text{m}$ for water clouds, from $1 \mu\text{m}$ to $60 \mu\text{m}$ in steps of $1 \mu\text{m}$ for ice clouds, respectively. The simulated zenith radiances were interpolated with a resolution of 0.1 in τ and $0.1 \mu\text{m}$ in r_{eff} to reduce the computational time. The calculations used in Section 4.1.2 and Section 4.1.3 were performed over the full wavelength region covered by CORAS. Here, the *FWHM* of CORAS spectrometers was considered in the simulations. Single-scattering properties based on Mie theory, according to Wiscombe (1980), were used for liquid water clouds; for ice clouds a parametrization of ice single-scattering properties from Baum et al. (2005a,b, 2007) was applied.

For the retrieval results presented in Section 5 the model input for calculating the LUT is adjusted to the measurement conditions during the OCEANET-transects. Usually, the ship speed is around 10 kn. In Figure 4.1a-b an exemplary time series of the differences in ship solar zenith angle θ'_0 (including the ships roll/pitch/heading angles) and in solar azimuth angle φ_0 for a 1 minute data resolution is shown. Differences between 1 minute increments of θ'_0 and φ_0 are mostly within $\pm 0.2^\circ$ and $\pm 0.3^\circ$. During local noon differences are smallest. But taking also the heading of the ship into account (Figure 4.1c), it is crucial to calculate the LUT with this time resolution. Course changes, especially during stations, yield a constantly altered sensor geometry. To determine the cloud base for a certain measurement day, data from ceilometer were interpolated to the observation time of CORAS measurements. Furthermore, cloud base heights from ceilometer, in combination with sky images and atmospheric soundings from the ship, were used as an estimate of cloud phase. Clouds with a base height $< 2 \text{ km}$ and a cloud top height below the freezing level obtained from radiosonde data, were classified as liquid water clouds. Accordingly, clouds were classified as ice clouds with base heights $> 5 \text{ km}$ and top heights above the freezing level. The geometrical thickness of the cloud (and cloud top height) was assumed using temperature and relative humidity profiles from the daily atmospheric soundings on RV *Polarstern* (Seidel et al., 2010). Within the cloud, relative humidity reaches values of up to 80%, while the decrease in temperature with altitude is reduced or even rises due to latent heat from condensation. The associated uncertainty of assuming a wrong geometrical cloud thickness is less than 2 – 4% for both retrieved parameters and can be neglected. Thermodynamic phase is the largest contributor to variability in zenith radiance due to differences in absorption and scattering from liquid water droplets and ice crystals. Cloud phase misclassification (mixed-phase clouds or cirrus above low-level liquid water clouds) lead to an overestimation of retrieved τ of up to 76%, while r_{eff} is biased by up to 114%. To parametrize the bidirectional reflectance distribution function (*BRDF*) for water surfaces which mainly depends on the wind speed a Cox and Munk parametrization (Cox and Munk, 1954; Mayer and Kylling, 2005) was implemented. The mean wind speed from ship observations was used for the parametrization. The results

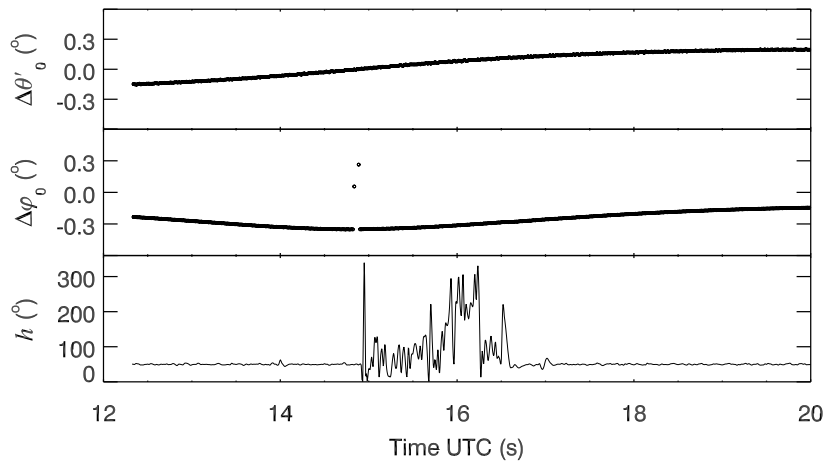


Figure 4.1: Time series of observed differences in (a) ship solar zenith angle θ'_0 and (b) solar azimuth angle φ_0 for a 1 Minute data resolution; (c) observed heading from ship INS. Data are from April 28, 2011, ANT-XXVII/4.

in Section 5 were performed with a 1 minute resolution of all input parameters for the wavelengths 450 nm, 680 nm, 1050 nm, 1250 nm, 1560 nm and 1670 nm used for the new retrieval method (see Section 4.3). For this configuration the computing time for 1 hour measurements is 45 minutes. By adjusting the model input parameters to every minute averaged observations for each day, the associated model uncertainties are mostly reduced.

4.1.2 Zenith Radiance

Figure 4.2 presents modeled zenith radiances over the ocean for different θ_0 as a function of τ . The calculations were carried out for a non-water absorbing wavelength at 532 nm and a liquid-water absorbing wavelength at 1560 nm and for two values of r_{eff} (solid lines: $r_{\text{eff}} = 5 \mu\text{m}$; dashed lines: $r_{\text{eff}} = 25 \mu\text{m}$). At 532 nm wavelength (Figure 4.2a) almost no sensitivity of $I_{\lambda, \text{mod}}^\downarrow$ with respect to r_{eff} is revealed. Both lines for different values of r_{eff} coincide. Zenith radiance increases with increasing τ up to a value of $4 < \tau < 5$ and decreases for $\tau > 5$. This non-monotonic behavior of zenith radiance leads to an ambiguous retrieval of τ . For example, zenith radiance $I_{\lambda, \text{mod}}^\downarrow = 0.3 \text{ W m}^{-2} \text{ nm}^{-1} \text{ sr}^{-1}$ at $\theta_0 = 40^\circ$ belongs to an optical thickness of either 4 or 15.

At the liquid-water absorbing wavelength of 1560 nm the sensitivity to r_{eff} is enhanced (see Figure 2.2), because of increased cloud droplet absorption (Figure 4.2b). Largest sensitivities to r_{eff} occur for $\tau > 20$ and at small values of θ_0 . Zenith radiances approach zero for large values of τ and thus decrease the sensitivity to retrieve r_{eff} . Two opposite effects lead to ambiguous retrieval results. With increasing r_{eff} forward scattering increases (see Figure 2.3) and thus the zenith radiance increases too. As shown in Figure 2.3a, the forward peak of the scattering phase function for scattering angles $\vartheta = 0 - 5^\circ$ increases with increasing r_{eff} . On the other hand, the larger the droplets, the larger the cloud droplet absorption (Rawlins and Foot, 1990) which decreases the zenith radiance.

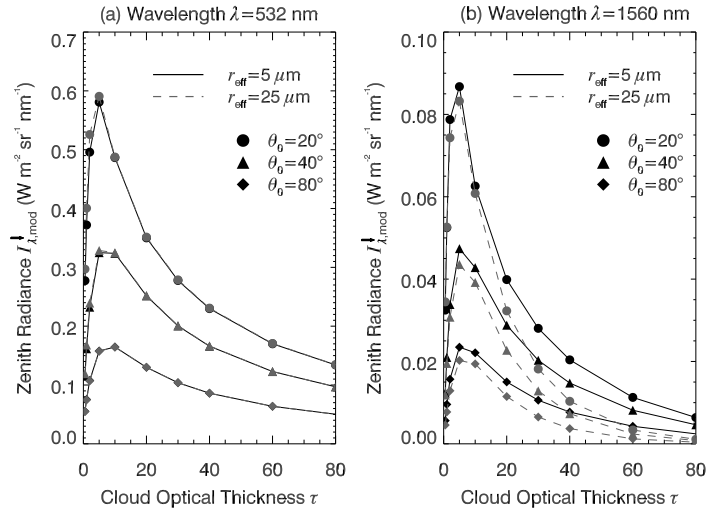


Figure 4.2: Modeled zenith radiance at the surface as a function of cloud optical thickness τ for a liquid water cloud with effective radii of $r_{\text{eff}} = 5 \mu\text{m}$ (solid lines) and $r_{\text{eff}} = 25 \mu\text{m}$ (dashed lines). Different symbols refer to θ_0 of 20° , 40° and 60° . Calculations were performed assuming an ocean surface albedo.

4.1.3 Transmissivity

Examples of modeled spectral transmissivity derived with Eq. (2.10) are shown in Figure 4.3a assuming a liquid water cloud based on McBride et al. (2011), and in Figure 4.3b for an ice cloud, both for different values of τ and two values of r_{eff} ($5 \mu\text{m}$: solid lines and $25 \mu\text{m}$: dashed lines). The shaded areas illustrate constant values of τ . The calculations were performed for $\theta_0 = 40^\circ$ and a surface albedo typical for ocean. Absorption bands of different atmospheric gases (O_3 : 470 nm; O_2 : 760 nm; H_2O : 720 nm, 820 nm, 940 nm, 1100 nm, 1380 nm, 1870 nm; and CO_2 : 1400 nm, 1600 nm, 2000 nm; Wendisch and Yang, 2012) are represented in the modeled spectral transmissivity. For the liquid water cloud largest transmissivity occurs at values of $4 < \tau < 5$ (in accordance with the radiances plotted in Figure 4.2) and decreases with increasing τ . At wavelengths shorter than about 1100 nm scattering dominates (see Figure 2.2b). Larger droplets with larger asymmetry factor result in enhanced forward scattering and thus in larger transmissivity. However, with increasing r_{eff} transmissivity decreases because of increasing cloud droplet absorption at wavelengths larger than about 1400 nm. The crossover between these competing effects occurs at wavelengths between 1100 nm and 1400 nm depending on the magnitude of cloud droplet absorption (McBride et al., 2011). Especially in the wavelength region between 1560 nm and 1670 nm the differences between $5 \mu\text{m}$ and $25 \mu\text{m}$ are largest and result in an enhanced sensitivity with respect to r_{eff} . Transmissivity values are more sensitive to the solar zenith angle, especially for smaller τ , since transmitted radiation is affected by fewer scattering interactions. Furthermore, the effect of a vertical gradient in r_{eff} on calculated zenith radiance is larger (Rawlins and Foot, 1990).

For the ice cloud larger values of r_{eff} cause increased transmissivity because the forward scattering peak is much more pronounced than for water droplets and depends on the sensor/solar geometry. Differences in the scattering phase function of non-spherical ice particles (see Figure 2.3a) result from different particle sizes and shapes. But additionally, enhanced

cloud droplet absorption decreases transmissivity (see Figure 4.3b). For example, at 1600 nm wavelength, because of the spectral shape of the imaginary part of the refractive index for ice, the absorption by an ice cloud is about twice the absorption by a liquid water cloud. The dashed lines ($r_{\text{eff}} = 25 \mu\text{m}$) always lie beneath the solid lines for smaller values of r_{eff} . Largest differences (and sensitivities) between simulations for two values of r_{eff} occur in the wavelength region between 1550 nm and 1700 nm. The slope of transmissivity becomes steeper in this wavelength region for increasing τ and r_{eff} . For optically thin ice clouds (e.g., $\tau = 0.1$) in the VIS wavelength region a high ratio of Rayleigh scattering (molecular) is transmitted through the cloud and dominates cloud scattering (Wen et al., 2008). This effect is later used to discriminate between thin and thick cirrus clouds in the VIS wavelength region.

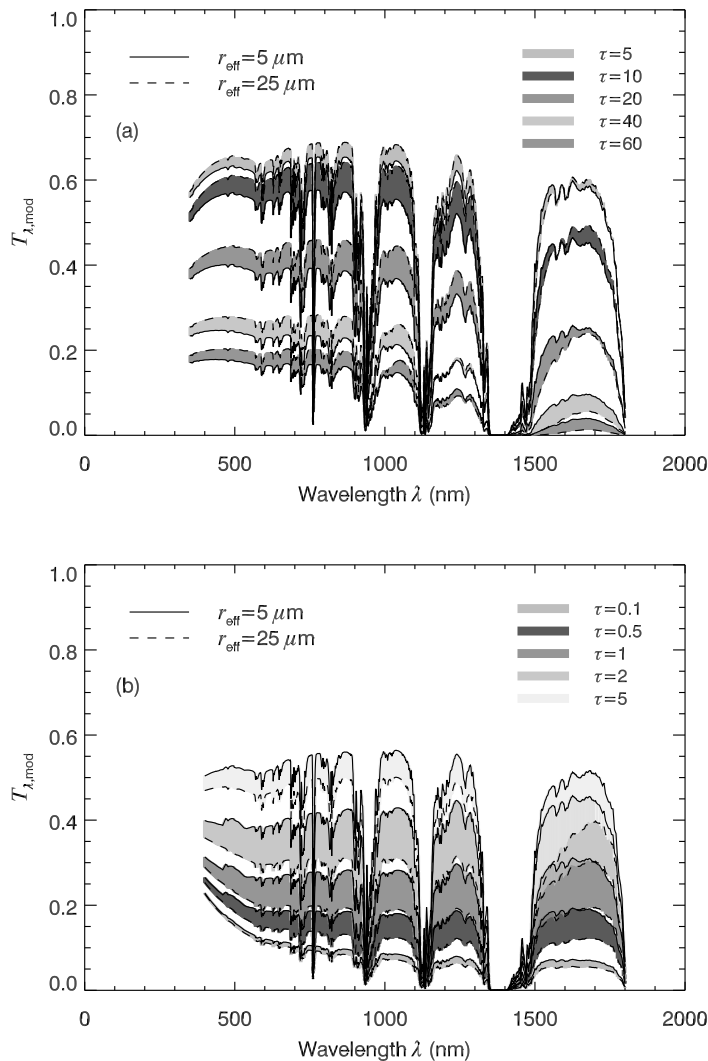


Figure 4.3: Modeled spectral transmissivity for different values of r_{eff} (solid lines for $r_{\text{eff}} = 5 \mu\text{m}$, dashed lines for $r_{\text{eff}} = 25 \mu\text{m}$) and τ (gray shaded areas) at $\theta_0 = 40^\circ$ and assuming an ocean surface albedo (a) for a liquid water cloud according to McBride et al. (2011), (b) for an ice cloud. Note the different values of τ for liquid water and ice cloud.

4.2 Existing Transmissivity-Based Cloud Retrievals

4.2.1 Standard Two-Wavelength Retrieval

Nakajima and King (1990) introduced a method to retrieve τ and r_{eff} from reflected radiance measurements. To emphasize the differences between reflectivity-based and transmissivity-based standard two-wavelength (2-WL) retrievals, Figure 4.4 shows the graphical representation of LUTs for reflectivity (a) and transmissivity (b). The underlying principle of the standard 2-WL retrieval is to combine reflectivity or transmissivity at a non-absorbing wavelength in the VIS (532 nm) with an absorbing wavelength in the NIR (1670 nm) for a range of values of τ and r_{eff} . These wavelengths have to be outside of water vapor and oxygen bands and should have substantially different water droplet (ice crystal) absorption characteristics (Nakajima and King, 1990).

The modeled spectral reflectivity in Figure 4.4a were derived using Eq. (2.9) assuming a liquid water cloud. The minimum of reflectivity at each wavelength correlates with the reflectivity of the underlying surface at these wavelengths without an atmosphere (Nakajima and King, 1990). The underlying surface corresponds to an ocean surface, which can be assumed as Lambertian. τ is determined by the reflectivity at a non-absorbing wavelength at 532 nm with less sensitivity to r_{eff} . Reflectivity monotonically increases with increasing τ and approaches a value of about 1 for thick clouds. r_{eff} is determined by the reflectivity at an absorbing wavelength at 1670 nm with largest values for small particles sizes. As r_{eff} increases also absorption monotonically increases for all values of r_{eff} . These characteristics of reflectivity enables a clear defined discrimination of r_{eff} . The sensitivity to τ and r_{eff} of non-absorbing against absorbing wavelength is nearly orthogonal as τ increases ($\tau > 20$). This means that measurements uncertainties in one wavelength have little impact on the properties determined primarily by the other wavelength.

Platnick (2000) showed that using modeled vertical weighting functions for transmissivity yields a more symmetric weighting throughout the center layer of a cloud. Whereas reflectivity weighting functions are more determined by the upper layer of the cloud. Applying the standard 2-WL retrieval method to transmissivity (see Figure 4.4b) reveals clear differences to a reflectivity-based method. The overall problem of transmissivity is the non-monotonic behavior toward τ , and additionally, the competing effects of scattering and absorption with increasing r_{eff} . Furthermore, zenith radiance is almost completely attenuated for optically thick clouds. Isolines of different values of r_{eff} in the LUT are nearly indistinguishable for clouds with $\tau > 10$ and $r_{\text{eff}} > 5 \mu\text{m}$ because of the lack of sensitivity to r_{eff} . Slightly better is the separation between values of τ ranging from 20 – 40 due to increasing cloud droplet absorption with increasing r_{eff} . For thick clouds ($\tau > 60$) zenith radiance approaches zero due to attenuation and thus transmissivity is less sensitive to both microphysical parameters. The isolines for constant τ are clear to separate compared to r_{eff} isolines. The ambiguity regarding clouds with τ between 3 and 7 makes the retrieval difficult. Here, measurement uncertainties in one wavelength exert a huge impact on the properties and complicates the retrieval. This 2-WL approach using transmissivity implies that it is possible to retrieve τ for clouds with $\tau > 10$, which corresponds to results found by e.g., Rawlins and Foot (1990),

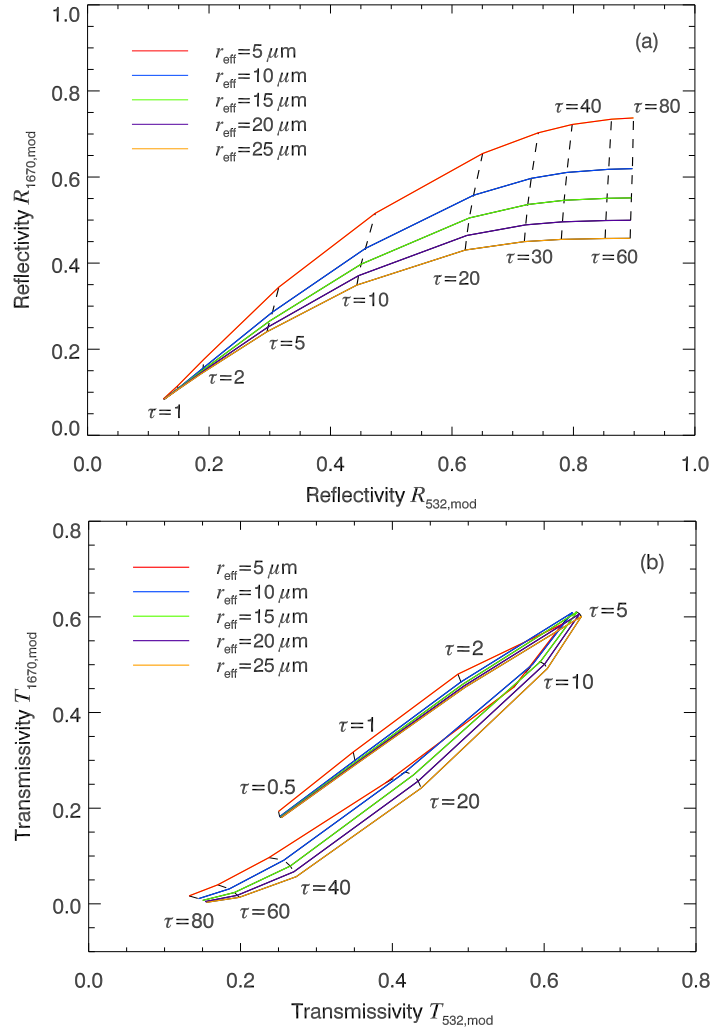


Figure 4.4: Standard 2-WL retrieval grid for a liquid water cloud using (a) modeled reflectivity and (b) modeled transmissivity for a solar zenith angle of $\theta_0 = 40^\circ$ and an assuming ocean surface albedo. Dashed isolines represent different values of τ and colored lines indicate different values of r_{eff} .

but the sensitivity to r_{eff} is not satisfactory. The retrieval uncertainties of a liquid water cloud for the standard 2-WL method is presented in Table 4.1. The uncertainties in τ and r_{eff} were calculated by propagating the measurement VIS uncertainty $\sigma_{532} = 5.1\%$ and the NIR uncertainty $\sigma_{1670} = 9.4\%$. Here, for a cloud with model input $\tau = 5$ and $r_{eff} = 5 \mu m$ the resulting τ is biased by up to 26%, while r_{eff} is biased by up to 248%. These errors emphasize that the 2-WL method is not suitable for transmissivity.

4.2.2 Spectral Slope Method

McBride et al. (2011) introduced a method to retrieve τ and r_{eff} using the spectral slope fit through normalized transmissivity between 1565 nm and 1634 nm in combination with transmissivity at 515 nm wavelength. The method was introduced for reflectivity observations to determine the cloud thermodynamic phase by Pilewskie and Twomey (1987) and Ehrlich et al. (2008a). They emphasize the spectral shape of basic optical properties which

Table 4.1: Uncertainties of cloud optical thickness τ and effective radius r_{eff} calculated from transmissivity retrievals for a liquid water cloud, see Fig. 4.4b. The uncertainties were calculated by propagating the measurement VIS uncertainty $\sigma_{532} = 5.1\%$, and NIR uncertainty $\sigma_{1670} = 9.4\%$ through the standard 2-WL retrieval.

τ	$r_{\text{eff}} (\mu\text{m})$	$(\tau)_{\text{retr}} \pm \delta(\tau)$	$(r_{\text{eff}})_{\text{retr}} \pm \delta(r_{\text{eff}}) (\mu\text{m})$
5	5	5.0 ± 1.3	5.0 ± 12.4
20	10	20.0 ± 2.2	10.0 ± 8.2
40	20	40.0 ± 2.5	20.0 ± 5.7

have a direct impact on transmissivity. Figure 4.5 presents the droplet coalbedo ($1 - \tilde{\omega}_0$, with single scattering albedo $\tilde{\omega}_0$; measure for absorption), the asymmetry factor g and the extinction coefficient b_{ext} across the spectral region for four different values of r_{eff} . The coalbedo increases with increasing r_{eff} , because cloud droplet absorption increases. The asymmetry factor and the extinction coefficient increase with increasing r_{eff} as forward scattering increases with cloud droplet size.

For the retrieval the slope of transmissivity over a certain spectral wavelength region is used. The selected wavelength region should reveal a linear characteristic of transmissivity over a wide range of τ and r_{eff} , and should be outside of bands with strong absorption (McBride et al., 2011). The linear regression of transmissivity in this spectral range has the advantage of reducing measurement and retrieval errors. Based on these criteria the spectral region between 1570 – 1630 nm (1565 – 1634 nm in McBride et al., 2011) was chosen for the regression. Figure 4.6 shows the modeled spectral transmissivity normalized with transmissivity T_{1570} at $\lambda = 1570$ nm for $\tau = 20$ and two values of r_{eff} ($5 \mu\text{m}$ and $25 \mu\text{m}$) over the NIR spectral region. Normalizing transmissivity to T_{1570} removes the effect of spectrally correlated errors (radiometric uncertainty, McBride et al., 2011). Due to largest cloud droplet

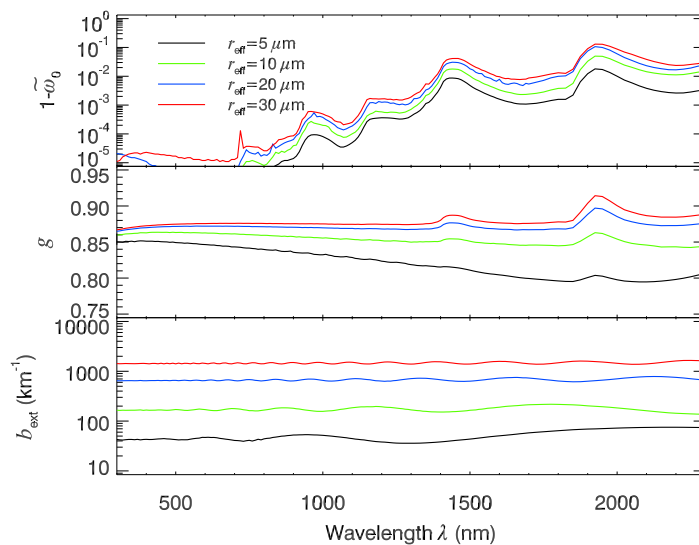


Figure 4.5: Spectral coalbedo $1 - \tilde{\omega}_0$, asymmetry factor g , and extinction coefficient b_{ext} of liquid water droplets for different values of r_{eff} over the spectral wavelength region.

absorption at $\lambda = 1570$ nm, normalized transmissivity increases with wavelength over the spectral region for both values of r_{eff} . Larger cloud droplet sizes ($25 \mu\text{m}$) with larger values of coalbedo always have a steeper slope than smaller droplet sizes ($5 \mu\text{m}$). This characteristic of the spectral slope provides the information on τ and r_{eff} .

The slope s was determined from a least-square linear regression between model results and the measured spectra as follows:

$$s = \frac{\sum_{n=1}^N \lambda_n \cdot \frac{T_n}{T_{1570}} - \frac{1}{N} \sum_{i=1}^N \lambda_i \sum_{n=1}^N \frac{T_n}{T_{1570}}}{\sum_{n=1}^N \lambda_n^2 - \frac{1}{N} \left(\sum_{n=1}^N \lambda_n \right)^2}. \quad (4.2)$$

Here, N is the number of points used in the fit (CORAS observations: 13 wavelengths; model: 61 wavelengths) and T is the transmissivity at each λ points.

Figure 4.7 presents the LUT for the spectral slope method. Modeled transmissivity at $\lambda = 532$ nm ($T_{532,\text{mod}}$) is plotted against the modeled spectral slope s for the same range of τ and r_{eff} as in Figure 4.4. Here, the slope axis is shown on a logarithmic scale. The isolines of constant r_{eff} are clearly separated for $\tau > 10$ compared to the standard 2-WL method in Figure 4.4b. Due to the increased sensitivity to r_{eff} from the spectral shape of the slope in the NIR region, a clear distinction of r_{eff} isolines is obvious. Largest spectral slopes refer to largest values of r_{eff} and for optically thick clouds. Similar to the standard 2-WL retrieval, sensitivity to τ with values of $\tau > 10$ is obvious. The ambiguity problem regarding thin clouds still remains. Isolines of τ ranging from 3 – 7 are less well separated and not distinct. Furthermore, a r_{eff} retrieval for thin clouds is also ambiguous because of the competing effects of forward scattering and absorption. Taking the measurement uncertainties of 5.1% at 532 nm and 2.2% for the normalized transmissivity T_n/T_{1570} into account, retrieval errors

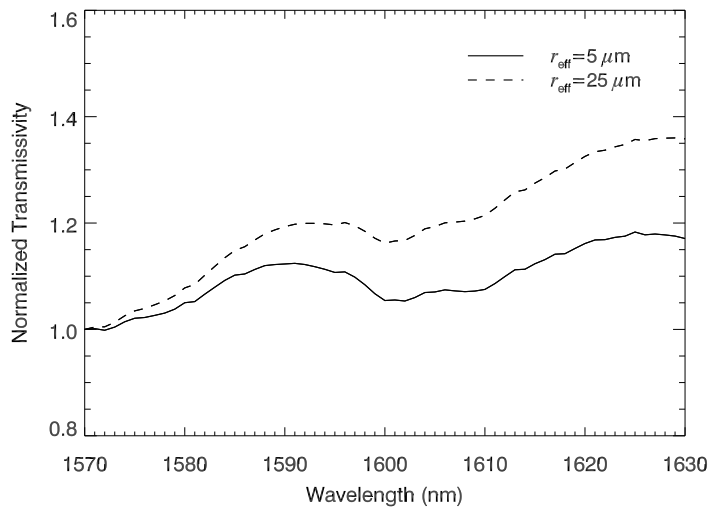


Figure 4.6: Normalized transmissivity for a liquid water cloud with $\tau = 20$ and two different values of r_{eff} (solid lines for $r_{\text{eff}} = 5 \mu\text{m}$, dashed lines for $r_{\text{eff}} = 25 \mu\text{m}$) across the NIR wavelength region of 1570 – 1630 nm.

of liquid water clouds are reduced but still relatively high, see Table 4.2. Compared to the standard 2-WL retrieval, the results for r_{eff} for $\tau > 20$ are significantly improved ($10 \pm 8.2 \mu\text{m}$ vs. $10 \pm 1.6 \mu\text{m}$). McBride et al. (2011) propagate a radiometric uncertainty in the VIS region of 3%. Due to the normalization of transmissivity, the spectrally uncorrelated error from the spectrometer signal of 0.1% (Pilewski et al., 2003) is given for their spectrometer system.

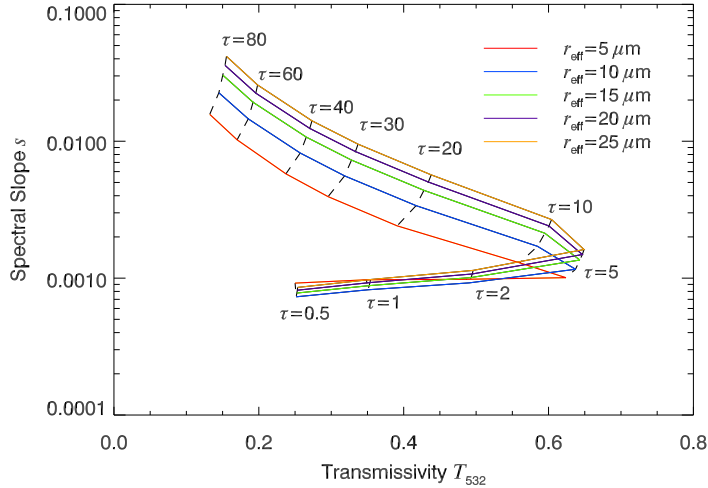


Figure 4.7: Spectral slope retrieval grid for a liquid water cloud using modeled transmissivity for a solar zenith angle of $\theta_0 = 40^\circ$ and an assuming ocean surface albedo. Dashed isolines represent different values of τ and colored lines indicate different values of r_{eff} .

Table 4.2: Uncertainties of cloud optical thickness τ and effective radius r_{eff} calculated from retrievals for a liquid water cloud, see Fig. 4.7. The uncertainties were calculated by propagating the measurement VIS uncertainty $\sigma_{532} = 5.1\%$, and NIR ratio uncertainty $\sigma_{T_n/T_{1570}} = 2.2\%$ through the spectral slope retrieval.

τ	$r_{\text{eff}} (\mu\text{m})$	$(\tau)_{\text{retr}} \pm \delta(\tau)$	$(r_{\text{eff}})_{\text{retr}} \pm \delta(r_{\text{eff}}) (\mu\text{m})$
5	5	5.0 ± 0.2	5.0 ± 2.2
20	10	20.0 ± 1.6	10.0 ± 1.6
40	20	40.0 ± 2.5	20.0 ± 3.3

4.3 A New Multi-Wavelength Cloud Retrieval Method

4.3.1 Multi-Wavelength Approach

Coddington et al. (2012) quantified the information content of spectral irradiance reflected by water clouds with the Shannon information content approach. This method delivers a quantitative measure of retrieval information, which can be used to identify wavelengths with enhanced retrieval sensitivity. There are certain wavelength regions where the information on individually τ or r_{eff} is amplified. In VIS wavelength regions, the signal of reflected (or transmitted) radiation is mainly influenced by τ , whereas in the NIR wavelength region the individually information content in r_{eff} increases with increasing droplet absorption (and

size), while it is minimal in VIS regions. However, when cloud droplet absorption dominates, cloud scattering in the NIR wavelength region, the joint information content to retrieve both τ and r_{eff} decreases. In this case the joint information content of τ and r_{eff} can not be used to completely separate the two variables in cloud retrievals.

In this thesis a new spectral cloud retrieval is proposed that uses the information of ratios of transmissivity at different wavelengths. A similar approach using ratios of reflected spectral radiances was reported for airborne measurements (Werner et al., 2013). Obviously, the wavelengths for the retrieval should exclude regions with significant molecular absorption. The systematic search for suitable wavelengths for the ratios of transmissivity was done separately for the VIS and NIR wavelength region to avoid a mixture of the two CORAS spectrometers and resulting systematic measurement uncertainties. Furthermore, the retrieval sensitivity affected by measurement uncertainties is reduced (see Section 4.3.2). Not each wavelength combination is useful to provide an optimum of information to retrieve τ and r_{eff} (Coddington et al., 2012).

To investigate the suitable wavelength combinations a sensitivity study for τ and r_{eff} was performed. To quantify the sensitivity of transmissivity ratios to both parameters, the percentage increase p of two transmissivity ratios $\mathcal{T}_A = T_{\lambda_1}/T_{\lambda_1}$ and $\mathcal{T}_B = T_{\lambda_2}/T_{\lambda_2}$ was calculated as follows:

$$p_{\tau} = \left[\left(\frac{T_{\lambda_1}(\tau = 20)}{T_{\lambda_2}(\tau = 20)} \bigg/ \frac{T_{\lambda_1}(\tau = 5)}{T_{\lambda_2}(\tau = 5)} \right) - 1 \right] \cdot 100\%, \quad (4.3)$$

$$p_{r_{\text{eff}}} = \left[\left(\frac{T_{\lambda_1}(r_{\text{eff}} = 25 \mu\text{m})}{T_{\lambda_2}(r_{\text{eff}} = 25 \mu\text{m})} \bigg/ \frac{T_{\lambda_1}(r_{\text{eff}} = 5 \mu\text{m})}{T_{\lambda_2}(r_{\text{eff}} = 5 \mu\text{m})} \right) - 1 \right] \cdot 100\%, \quad (4.4)$$

with λ_1 and λ_2 ranging from 350 – 1800 nm. The results are plotted in Figure 4.8. The black solid line is the one-to-one line. According to Eqs. (4.3) and (4.4) all values left from this line, that is $\lambda_1 < \lambda_2$, it is a percentage increase in the difference between two ratios of transmissivity. Accordingly, the same holds true for all values right from the one-to-one line when $\lambda_1 > \lambda_2$. The larger the percentage increase p the larger is the sensitivity of ratios of transmissivity toward τ and r_{eff} . All wavelengths from gas absorption bands are removed.

Figure 4.8a–b presents the sensitivity to τ for the VIS (a) and NIR region (b). For ratio \mathcal{T}_A and \mathcal{T}_B , τ is 5 and 20, respectively, while $r_{\text{eff}} = 10 \mu\text{m}$ is constant for both ratios. In the VIS region a general sensitivity to τ is obvious. Almost all ratios with $\lambda_1 < \lambda_2$ show $p_{\tau} > 3\%$. Largest sensitivities occur for combinations of λ_1 between 400 – 600 nm with λ_2 ranging from 600 – 900 nm. The percentage increase p_{τ} in the NIR region achieves largest values (up to 10%) for wavelengths between 1500 – 1700 nm, but also for wavelength combinations of λ_1 around 1000 – 1100 nm with λ_2 around 1150 – 1300 nm, which results from enhanced attenuation for thicker clouds. In general, the sensitivity to τ is given in a number of possible wavelength combinations.

This is different for the r_{eff} sensitivity presented in Figure 4.8c–d. Here, the optical thickness is constant ($\tau = 20$), and r_{eff} for ratio \mathcal{T}_A and \mathcal{T}_B is 5 μm and 25 μm respectively. In the VIS region (c) no percentage increase of sensitivity to r_{eff} for $\lambda_1 < \lambda_2$ is obvious. Increased cloud

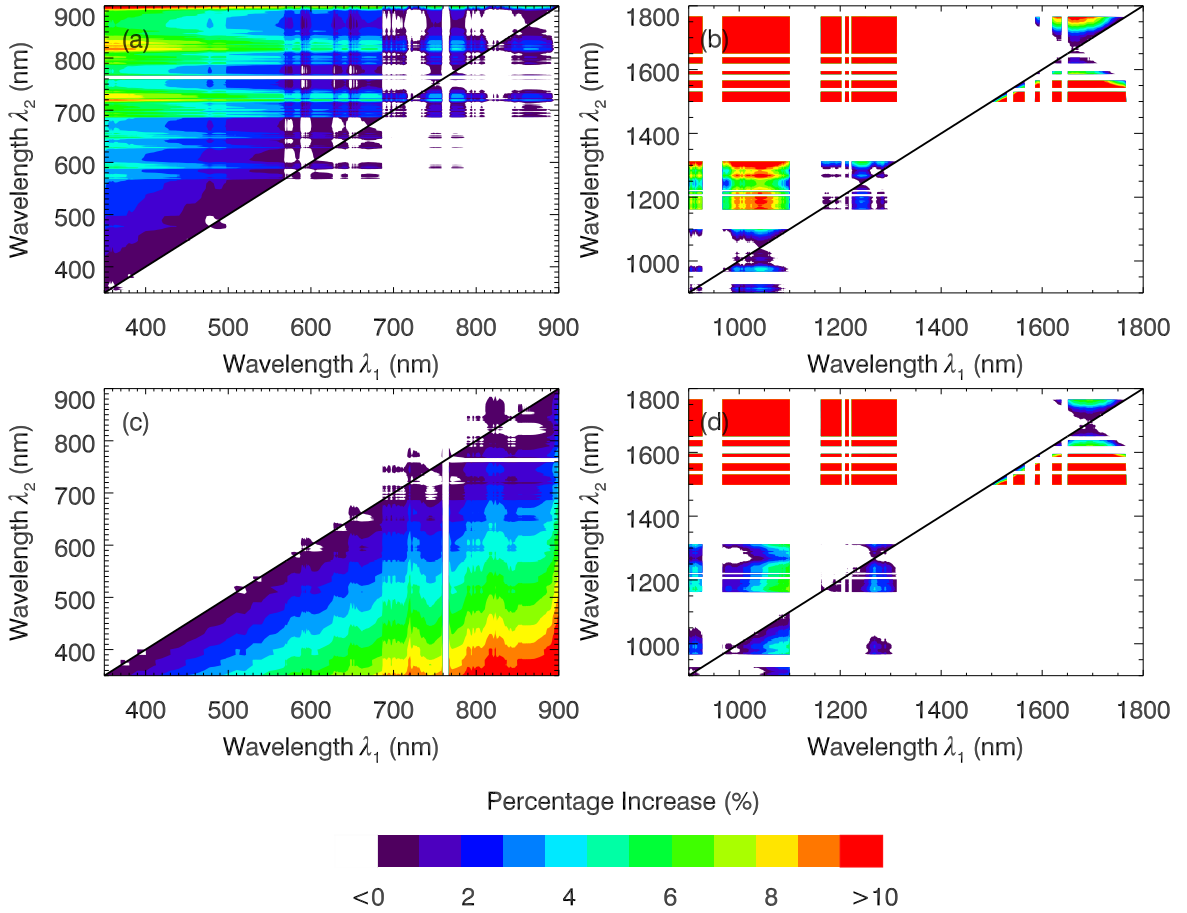


Figure 4.8: Spectral percentage increase of sensitivity to either τ (a-b) or r_{eff} (c-d). For detailed information see text.

droplet sizes cause decreased transmissivity ratios. Largest sensitivities are apparent for $\lambda_1 > 750$ nm in combination with $\lambda_2 < 450$ nm. However, with respect to the τ sensitivity in Figure 4.8a, the r_{eff} sensitivity shows an opposite behavior. Therefore, a wavelength combination with $\lambda_1 < \lambda_2$ is inappropriate to obtain information of both parameters. Whereas, in the NIR region (d) the same spectral sensitivity as for τ is found for r_{eff} . Largest percentage increase $p_{r_{\text{eff}}}$ can be found for wavelengths between 1500 – 1700 nm, because of increased cloud droplet absorption with increasing cloud droplet size. Also increased sensitivity for combinations of λ_1 around 1000 – 1100 nm with λ_2 around 1150 – 1300 nm is evident, but $p_{r_{\text{eff}}}$ reaches compared to p_{τ} smaller percentage (4-7%). In conclusion, suitable wavelength combinations for r_{eff} sensitivity are fewer compared to τ , favoring the NIR wavelength region.

To retrieve τ and r_{eff} , and, additionally dealing with the ambiguity problem for transmissivity, at least three independent measurement points are required, which are sensitive to these parameters.

The ratio $\mathcal{T}_1 = T_{450}/T_{680}$ discriminates between thin and thick clouds (thin clouds transmissivity increases with τ , thick clouds vice versa). For values of $\tau < 5$ the portion of Rayleigh scattering in the VIS spectral region is larger. Similar results were found by LeBlanc et al. (2014). In Figure 4.9a the ratio of $I_{\lambda, \text{mod}}^{\downarrow}$ for clear sky to cloudy conditions ($\tau = 0.5$) over

the VIS wavelength region is plotted. Even in the presence of thin clouds, zenith radiance is larger than that with no cloud and thus $T_{450,\text{mod}}$ is larger than $T_{680,\text{mod}}$ and provides the information on τ and r_{eff} . These wavelengths are illustrated with vertical dashed lines in Figure 4.9a. Other combinations from $T_{450,\text{mod}}$ to transmissivity around $\lambda = 790$ nm are also possible (see Figure 4.8a), but the correspondence between measured and modeled radiances in this region is slightly better for $\lambda = 680$ nm. Ratios of transmissivity including wavelengths below 400 nm were not included because the sensitivity of the spectrometer decreases towards the UV.

In Figure 4.9b the coalbedo across the NIR spectral region for different values of r_{eff} is plotted.

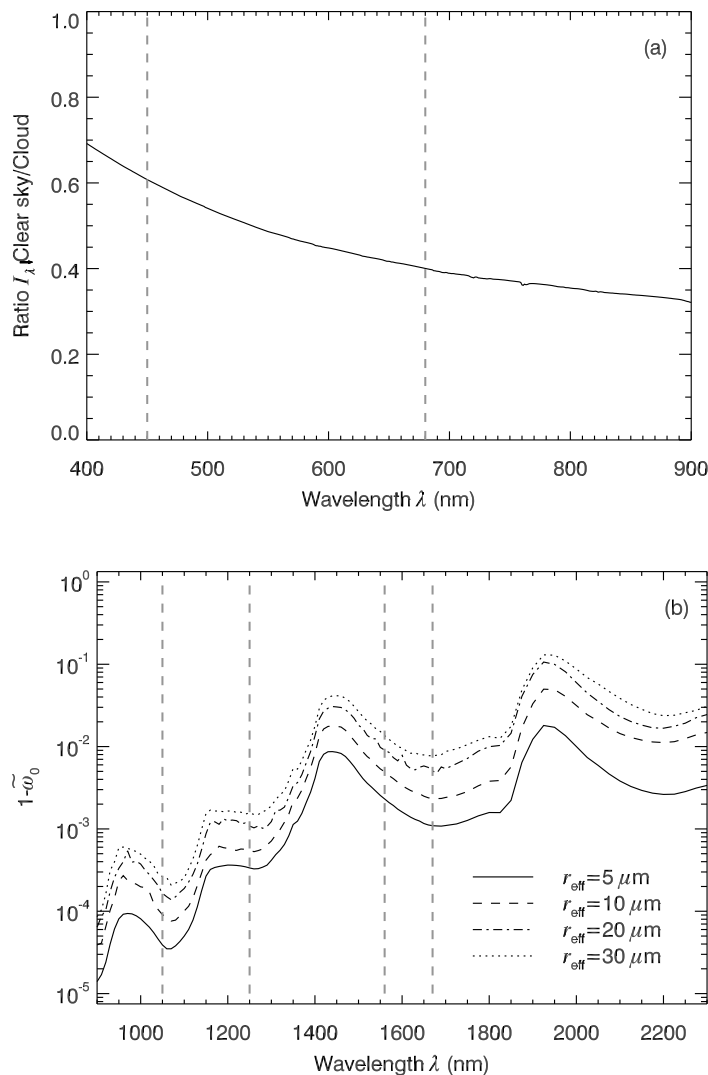


Figure 4.9: (a) Ratio of modeled spectral radiances $I_{\lambda,\text{mod}}^{\downarrow}$ for a clear sky relative to cloudy ($\tau = 0.5$) conditions over the VIS wavelength region. Retrieval wavelengths of 450 nm and 680 nm are indicated with vertical dashed lines. (b) Spectral coalbedo $1 - \tilde{\omega}_0$ for different values of r_{eff} over the NIR wavelength region. Retrieval wavelengths of 1050 nm and 1250 nm, and 1670 nm and 1560 nm are marked with vertical dashed lines.

It increases with increasing r_{eff} , while cloud droplet absorption increases. Based on the results of McBride et al. (2011) and the sensitivity study in Figure 4.8d, the ratio of transmissivity $\mathcal{T}_2 = T_{1670}/T_{1560}$ is sensitive to r_{eff} because absorption distinctions are largest. To enhance the sensitivity to this parameter, a second ratio in the NIR of transmissivity with $\mathcal{T}_3 = T_{1050}/T_{1250}$ was considered. These wavelengths are equidistant from water vapor absorption bands, and the sensitivity of the coalbedo to r_{eff} with $\tau > 10$ is high. Furthermore, \mathcal{T}_3 contains the information on τ and circumvents the ambiguity in τ . The retrieval wavelengths in the NIR region are illustrated with vertical dashed lines in Figure 4.9b.

Figures 4.10a and 4.10b show the results of simulated ratios of transmissivity for different combinations of τ and r_{eff} for a liquid water cloud situated in 2 – 4 km (a), and an ice cloud in 7 – 8 km (b). Isolines of constant r_{eff} (solid lines) and τ (dashed lines) are plotted. The new multi-wavelength approach circumvents the ambiguity regarding τ . The combination of three transmissivity ratios allows to ambiguously retrieve τ and r_{eff} . Adding the ratio $T_{450,\text{mod}}/T_{680,\text{mod}}$ provides improved sensitivity to thin clouds. The two branches of the surface represent thick clouds, where \mathcal{T}_2 and \mathcal{T}_3 dominates ($\tau > 10$), and thin clouds, where \mathcal{T}_1 reaches values larger than 1 with decreasing τ (insert in Figures 4.10a), while the other two ratios vary only slightly. The knee of the surface, where the two branches separate, conforms to the largest values of transmissivity and depends only slightly on θ_0 .

To retrieve microphysical properties from observations the best match between the modeled and observed transmissivity is inferred by finding the minimum of a cost function $f(\tau, r_{\text{eff}})$:

$$(\tau_{\text{retr}}, r_{\text{eff, retr}}) = \min [f(\tau, r_{\text{eff}})], \quad (4.5)$$

with:

$$f(\tau, r_{\text{eff}}) = \sqrt{\sum_{n=1}^3 [\mathcal{T}_{n,\text{obs}} - \mathcal{T}_{n,\text{mod}}(\tau, r_{\text{eff}})]^2}, \quad (4.6)$$

where

$$\mathcal{T}_1 = \frac{T_{450}}{T_{680}}; \mathcal{T}_2 = \frac{T_{1670}}{T_{1560}}; \mathcal{T}_3 = \frac{T_{1050}}{T_{1250}}, \quad (4.7)$$

which is the sum of the difference between the three observed and modeled transmissivity ratio $\mathcal{T}_{n,\text{obs}/\text{mod}}$ for the entire range of τ and r_{eff} .

4.3.2 Retrieval Uncertainties

Uncertainties in the retrieval are caused by misclassification of thermodynamic phase, multi-layer clouds, geometrical thickness of the cloud or uncertainties of the model input parameters, which is discussed in Section 5.4. This section discusses only measurement uncertainties. Due to the use of ratios of transmissivity either in the VIS or NIR region most of the measurement uncertainties described in Section 3.2.2 cancel. Only statistical uncertainties of the spectrometer signal of $\sigma_{\mathcal{T}_1} = 0.5\%$, $\sigma_{\mathcal{T}_2} = 2.2\%$, and $\sigma_{\mathcal{T}_3} = 1.8\%$ contributes to the retrieval uncertainty, respectively. The spectral dependent changes of the response function from different calibrations, which may also contributes to the overall uncertainty, were determined by comparing absolute and field calibration ratios for the three

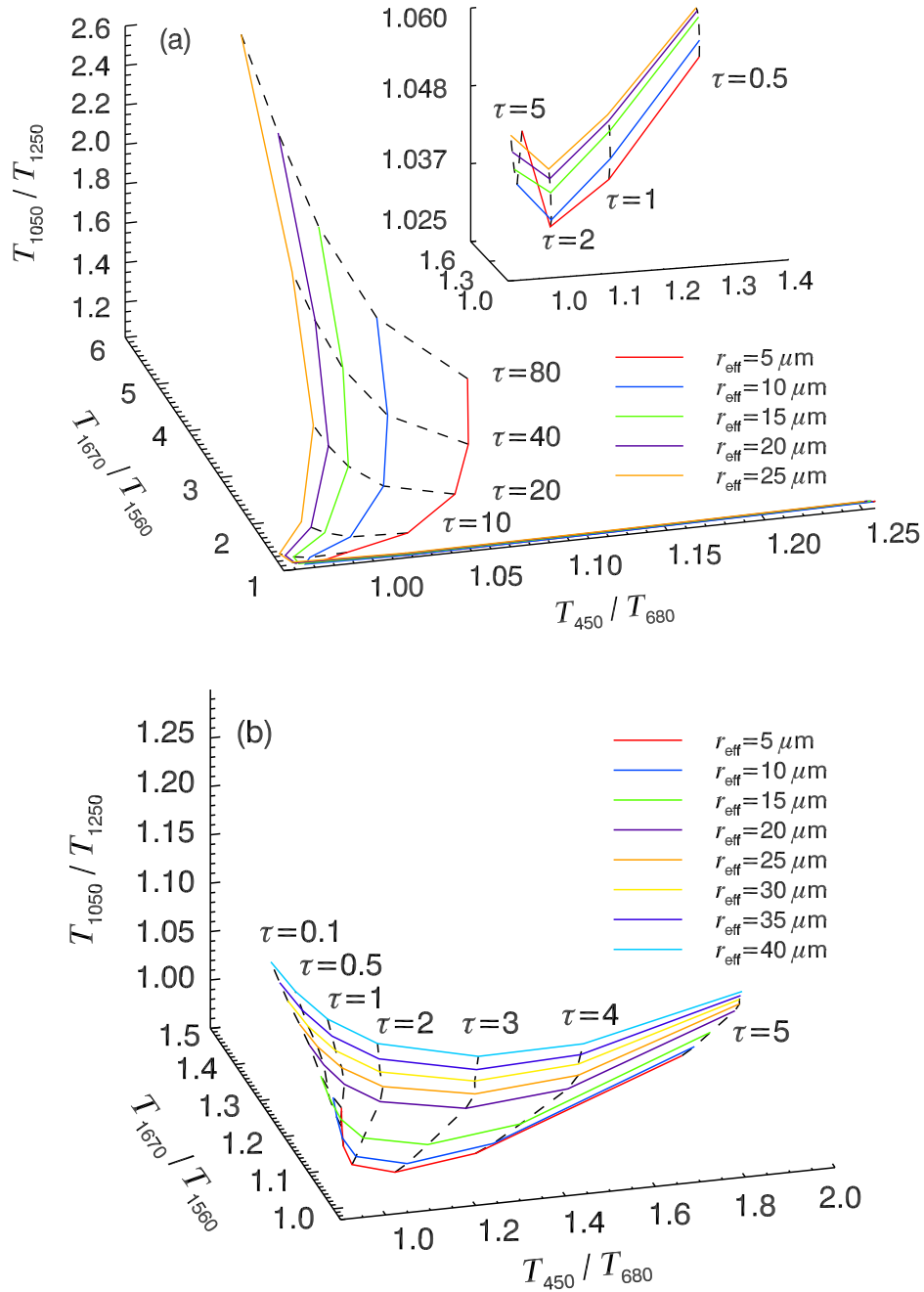


Figure 4.10: Retrieval grid using modeled ratios of transmissivity for a solar zenith angle of $\theta_0 = 40^\circ$ and an assuming ocean surface albedo. Dashed isolines represent different values of τ and colored lines indicate different values of r_{eff} (a) for a liquid water cloud for $\tau > 10$ with zoom into axis for thin clouds with $\tau < 5$ in the upper right part, and (b) for an ice cloud.

wavelengths ratios. These calibration ratios were almost spectral constant and lie within the range of the statistical uncertainties of the spectrometers. Therefore, spectral dependent changes were negligible. For the retrieval Eq. (4.5) 64 different combinations from $T_{450} \pm \sigma_{\mathcal{T}_1}$, $T_{680} \pm \sigma_{\mathcal{T}_1}$, $T_{1050} \pm \sigma_{\mathcal{T}_3}$, $T_{1250} \pm \sigma_{\mathcal{T}_3}$, $T_{1560} \pm \sigma_{\mathcal{T}_2}$, $T_{1670} \pm \sigma_{\mathcal{T}_2}$ of the cost function $f(\tau, r_{\text{eff}})$ are possible by propagating the uncertainty of the spectrometer signal. Eq. (4.6) writes:

$$f(\tau_N, r_{\text{eff},N}) = \sqrt{\sum_{n=1}^3 [(\mathcal{T}_{n,\text{obs}})_N - \mathcal{T}_{n,\text{mod}}(\tau, r_{\text{eff}})]^2}, \quad (4.8)$$

with $N = 1, \dots, 64$. Often a solution appears twice or four times. Here, for example, even for the ratio $T_{450} + \sigma_{\mathcal{T}_1}$ to $T_{680} + \sigma_{\mathcal{T}_1}$ the spectrometer signal uncertainty cancel out, when $\sigma_{\mathcal{T}_1}$ propagates in the same direction. This results in a solution set $(\tau_N, r_{\text{eff},N})$ with $N = 1, \dots, 64$ including the measurement uncertainties of the ratios. The median of this solution set is used as the final retrieval result for τ_{retr} and $r_{\text{eff,ret}}$. The resulting retrieval uncertainty is the standard deviation of all 64 solutions. The uncertainties for the retrieval of liquid water clouds and ice clouds are presented in Table 4.3 and Table 4.4, respectively. Small changes in the NIR ratios, which correspond to a steeper slope of transmissivity in the wavelength region between 1560 nm and 1670 nm, cause a shift towards larger cloud droplets in the LUT. The errors depend on the position of the measurements on the solution surface in the three-dimensional ratio coordinates as the distance between different isolines of τ and r_{eff} .

Table 4.3: Uncertainties of cloud optical thickness τ and effective radius r_{eff} calculated from retrievals for a liquid water cloud, see Fig. 4.10a. The uncertainties were calculated by propagating the ratio uncertainty $\sigma_{\mathcal{T}_1} = 0.5\%$, $\sigma_{\mathcal{T}_2} = 2.2\%$, and $\sigma_{\mathcal{T}_3} = 1.8\%$ through $N = 1, \dots, 64$ possible solutions of the cost function.

τ	$r_{\text{eff}} (\mu\text{m})$	$(\tau_N)_{\text{med}} \pm \delta(\tau_N)$	$(r_{\text{eff},N})_{\text{med}} \pm \delta(r_{\text{eff},N}) (\mu\text{m})$
5	5	5.0 ± 1.7	5.0 ± 3.6
20	10	20.0 ± 2.1	10.0 ± 2.1
40	20	40.0 ± 1.5	20.0 ± 1.2

Table 4.4: The same as Table 4.3 but for an ice cloud, see Fig. 4.10b.

τ	$r_{\text{eff}} (\mu\text{m})$	$(\tau_N)_{\text{med}} \pm \delta(\tau_N)$	$(r_{\text{eff},N})_{\text{med}} \pm \delta(r_{\text{eff},N}) (\mu\text{m})$
0.5	30	0.50 ± 0.04	30.0 ± 6.8
1	20	1.0 ± 0.1	20.0 ± 1.9
1	40	1.0 ± 0.1	39.6 ± 2.8
5	20	5.0 ± 0.7	20.0 ± 2.0

5 Case Studies

Individual case studies from the OCEANET–transects are presented to exemplify the new multi–wavelength cloud retrieval. The geographic positions of the chosen cloud situations are illustrated in Figure 5.1 with colored squares. Case analysis concentrates on four cloud types which are used in Chapter 6. Section 5.1 focuses on liquid water clouds and is divided into three cloud scene classes; Section 5.1.1 and Section 5.1.2 investigate homogeneous and inhomogeneous clouds, while Section 5.1.3 shows results for scattered clouds. Different cirrus cloud scenes are discussed in Section 5.2. A comparison of the spectral slope method with the new multi–wavelength method is presented in Section 5.3. A detailed uncertainty discussion is given in Section 5.4. Parts of this chapter were published by Brückner et al. (2014).

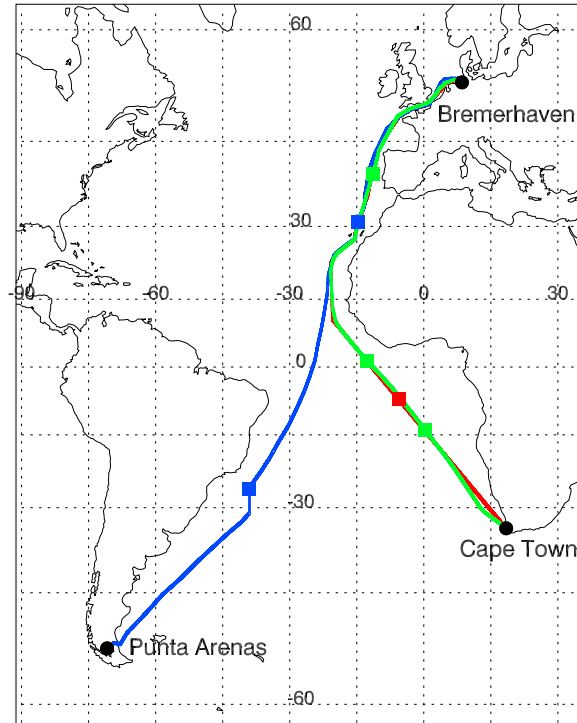


Figure 5.1: Cruise plots of ANT-XXVII/4 in spring 2011 (red), ANT-XXVIII/5 in spring 2012 (blue) and ANT-XXIX/1 in autumn Oct/Nov 2012 (green). Coordinates from the presented case studies are plotted with colored square symbols. Numbers indicate geographic longitude and latitude (in degrees).

5.1 Liquid Water Clouds

5.1.1 Homogeneous Cloud Case

A liquid water cloud was observed on November 19, 2012 around 15°S and 0°E during ANT-XXIX/1. Figure 5.2a shows the time series of the observed ratios at $T_{450,\text{obs}}/T_{680,\text{obs}}$, $T_{1670,\text{obs}}/T_{1560,\text{obs}}$, and $T_{1050,\text{obs}}/T_{1250,\text{obs}}$. The cloud base height derived from ceilometer data was around 800 m. The full-sky imager characterized the cloud as almost homogeneous. This coincides with almost constant ratios of observed transmissivity. The ratio $T_{450,\text{obs}}/T_{680,\text{obs}}$ and $T_{1050,\text{obs}}/T_{1250,\text{obs}}$ were divided by the ratio at $T_{1670,\text{obs}}/T_{1560,\text{obs}}$, to enhance the sensitivity to r_{eff} . This normalization accounts for the reduced information on r_{eff} because the ratio $T_{1670,\text{obs}}/T_{1560,\text{obs}}$ is influenced by the enhanced cloud droplet absorption in the NIR range. When the cloud becomes optically thicker and cloud droplets become larger this ratio increases. For example, around 12.2 UTC, the ratio $T_{1670,\text{obs}}/T_{1560,\text{obs}}$ reaches values up to 1.7 which means that cloud droplets and τ increase according to the LUT in Section 4.3. On the other hand, when the ratio in the VIS range becomes largest, which indicates a high ratio of Rayleigh scattering, the cloud is getting optically thinner and the other two remaining ratios become small.

In Figure 5.2b retrieval results of τ and r_{eff} are shown. The mean retrieved cloud optical thickness is 9.1 ± 0.5 . The mean effective radius is $16.1 \pm 1.7 \mu\text{m}$. The retrieved r_{eff} is more variable with values ranging between $2 - 30 \mu\text{m}$ and shows higher uncertainties with up to $\pm 7.1 \mu\text{m}$ compared to τ . Using Eq. (4.8) uncertainties of τ and r_{eff} were calculated along the time series. Considering a threshold of an uncertainty of ± 1 in τ , and according to the suggested one from McBride et al. (2011), an uncertainty of $\pm 2 \mu\text{m}$ in r_{eff} , the new retrieval results in 87% and 78% valid retrievals for τ and r_{eff} , respectively. The uncertainty of the measurements increases for thicker clouds because the attenuation of the spectral radiance

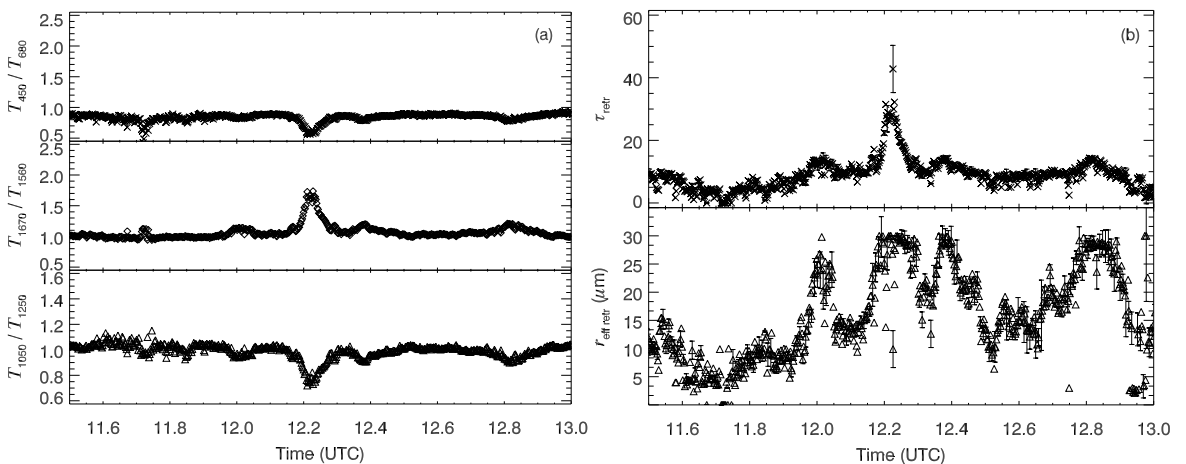


Figure 5.2: (a) Time series of observed transmissivity ratios at $T_{450,\text{obs}}/T_{680,\text{obs}}$, $T_{1670,\text{obs}}/T_{1560,\text{obs}}$, and $T_{1050,\text{obs}}/T_{1250,\text{obs}}$ at 11.5 - 13.0 UTC on November 19, 2012 around 15°S and 0°E from ANT-XXIX/1. (b) Time series of τ (upper panel) and r_{eff} (lower panel), based on retrievals using data from CORAS. The distance covered in the depicted times series is about 2.8 km.

is stronger and, therefore, the contribution of the signal-to-noise ratio to the uncertainty increases. For selected time periods (e.g., between 12.2–12.3 UTC) r_{eff} reaches values up to $30\ \mu\text{m}$. Unfortunately, the simulations were limited to $r_{\text{eff}} < 30\ \mu\text{m}$ because this suffices for most non-precipitating liquid water clouds and more specifically measurement uncertainties are too high for $r_{\text{eff}} > 30\ \mu\text{m}$. Obviously r_{eff} is larger than $30\ \mu\text{m}$ but the extrapolation to larger r_{eff} is not a suitable method for these complex LUTs. Possible reasons for $r_{\text{eff}} > 30\ \mu\text{m}$ could be the presence of overlying cirrus above the low-level stratocumulus or precipitating clouds. The former can be excluded since there was no evidence of high cirrus in satellite images or atmospheric soundings for that measurements example (not shown). While the HATPRO rain sensor did not detect precipitation at the surface during the time period, it is possible that evaporating drizzle in the atmosphere cause these large r_{eff} values. Wood (2000) and Chen et al. (2008) suggest, based on theoretical analysis and synergetic ship-based observations of low-level liquid water clouds, that drizzle droplets near the cloud base can significantly increase r_{eff} . The high variability is caused by entrainment of thermal energy and water vapor into the cloud from the sublayer below, cloud droplets can grow in updrafts or evaporate in the downdrafts and thus causes the variability in the droplet effective radius.

Using the retrieved values of τ and r_{eff} , the liquid water path (*LWP*) is calculated. *LWP* is approximated using the following equation:

$$LWP = \frac{2}{3} \varrho \cdot \tau \cdot r_{\text{eff}}, \quad (5.1)$$

where ϱ is the water density. Here, the liquid water content and r_{eff} is constant with height (e.g., Han et al., 1994). Wood and Hartmann (2006) determined the *LWP* for adiabatic clouds where the liquid water content increases linearly with altitude above cloud height with:

$$LWP = \frac{5}{9} \varrho \cdot \tau \cdot r_{\text{eff}}. \quad (5.2)$$

Deriving *LWP* using Eq. (5.1) results in values of 20% larger than those using Eq. (5.2). In general, the comparison of the *LWP* obtained from microwave radiometer HATPRO and the *LWP* retrieved from transmissivity measurements exhibits a better agreement of results using Eq. (5.2) as shown.

A comparison between the retrieved *LWP* from the microwave radiometer HATPRO and the *LWP* retrieved from the spectral transmissivity measurements is presented in Figure 5.3a for November 19, 2012. For the analyzed time period the mean *LWP* and standard deviation was $87 \pm 49\ \text{g m}^{-2}$ for HATPRO and $97 \pm 11\ \text{g m}^{-2}$ for the spectral cloud retrieval. CORAS overestimates the *LWP* for values $> 80\ \text{g m}^{-2}$ but underestimates the *LWP* for values $< 80\ \text{g m}^{-2}$ compared to HATPRO which is shown in the scatter plot in Figure 5.3b. The black dashed line is the one-to-one line. The uncertainty of the spectral radiance measurements increases in thicker clouds and, therefore, the number of valid retrievals decreases. Larger values of retrieved r_{eff} cause an overestimation of CORAS derived *LWP*. However, drizzle-sized droplets can lead to a wrong estimate of the liquid water distribution and, therefore, lead to an overestimation of *LWC* in the microwave radiometer retrievals

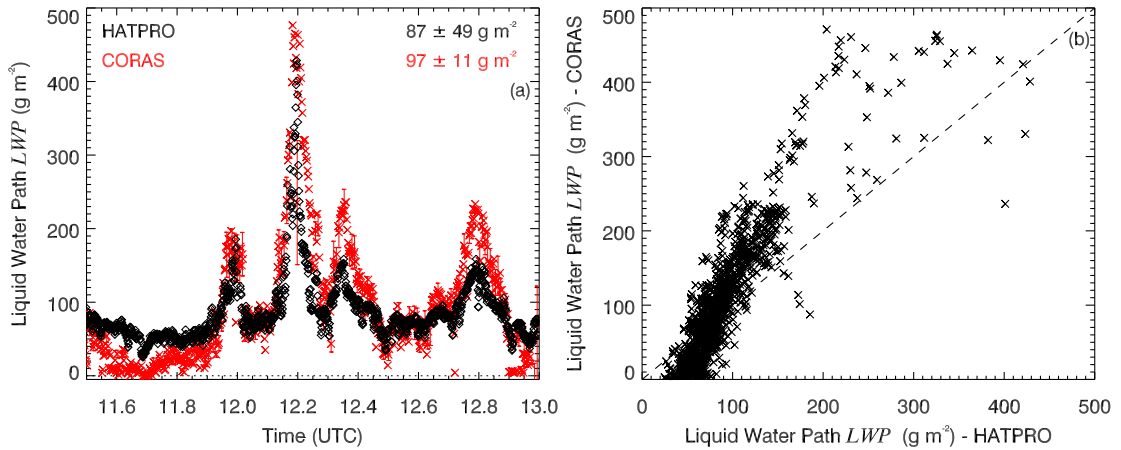


Figure 5.3: (a) Time series of LWP as retrieved from HATPRO (black diamonds) and CORAS (red crosses) data at 11.5 - 13.0 UTC on November 19, 2012 around 15°S and 0°E from ANT-XXIX/1. (b) Scatter plot of the retrieved LWP from HATPRO and CORAS.

(Löhnert et al., 2001). Furthermore, deviations in the CORAS LWP retrieval might come from the approximation of the plane-parallel cloud model in the radiative transfer model. Boers et al. (2006) suggested a sub-adiabatic cloud model which parametrizes the vertical variation of cloud optical and microphysical properties. In this cloud model τ and r_{eff} are explicit functions of the geometrical thickness z and the droplet number concentration N of the cloud. The major source of uncertainty in the LWP retrieval is the sub-adiabatic behavior of the cloud, which is described as the sub-adiabatic fraction Fr . Due to turbulent entrainment and mixing processes in the cloud, Fr typically ranges between 0.3 – 0.9 (Boers et al., 2006). For oceanic clouds Boers et al. (1998a) found a typical value of $Fr = 0.6$. The shape of the vertical LWC profile varies between a linear and a C-shaped profile and is characterized by factor α , which determines the vertical weight of the liquid water distribution for a given value of Fr (Boers et al., 2006). The smaller the value of α , the closer the LWC profile approaches linearity. For a given τ and r_{eff} the deviation from adiabatic clouds ($Fr = 1$) lead to an increase of geometrical thickness of the cloud but a decrease in cloud base droplet number concentration. To quantify the influence of different cloud models on the retrieved cloud properties, further investigations based on satellite or synergetic observations are needed.

5.1.2 Inhomogeneous Cloud Case

A time series of the retrieved LWP from HATPRO and CORAS of an inhomogeneous liquid water cloud is shown in Figure 5.4a for May 6, 2012 around 28°N and 15°W during ANT-XXVIII/5 at 7.45-12.0 UTC. Periods of precipitation are shaded based on HATPRO rain sensor data, since both instruments do not provide reliable data during precipitation. The mean LWP and standard deviation was $170 \pm 216 \text{ g m}^{-2}$ for the microwave and $146 \pm 124 \text{ g m}^{-2}$ for the result of the spectral cloud retrieval. While 76% and 72% of all retrievals passed the uncertainty threshold in τ and r_{eff} for the entire time series of an inhomogeneous cloud, only 52% of τ and 42% of r_{eff} valid retrievals under thick clouds ($\tau > 40$) were obtained. The microwave radiometer retrieves larger LWP with higher uncertainties during and also

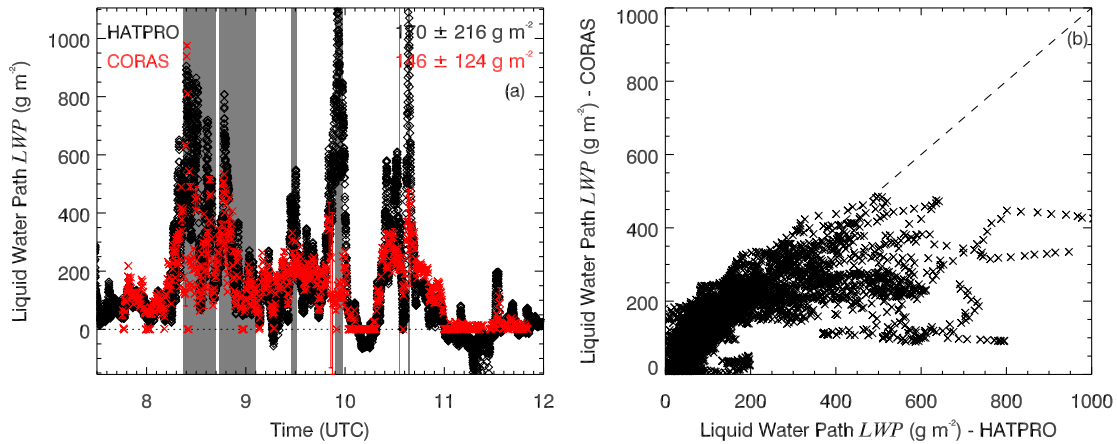


Figure 5.4: (a) Time series of LWP as retrieved from HATPRO (black diamonds) and CORAS (red crosses) data at 7.45 - 12.0 UTC on May 6, 2012 around 28°N and 15°W from ANT-XXVIII/5. (b) Scatter plot of the retrieved LWP from HATPRO and CORAS. The distance covered in the depicted times series is about 23 km.

around the periods of rain, because rain droplets can evaporate in the atmosphere before they reach the surface. Additionally, rain droplets cause uncertainties in the HATPRO LWP retrieval because the assumption of neglecting scattering in radiative transfer model used in the HATPRO algorithm is not valid for rain droplets. Furthermore, major uncertainties in the HATPRO retrieval are caused by the contamination of the radome with water. The appropriate scatter plot for the presented time period is shown in Figure 5.4b. The rain droplets in the atmospheric column cause higher uncertainties in HATPRO LWP retrieval and a shift towards larger values compared to CORAS LWP . Therefore, all rain-flagged data points were removed. The microwave radiometer measures the emission of cloud droplets regardless of size in the microwave wavelength region which is directly proportional to LWC . For that purpose it is not important whether the cloud is homogeneous or inhomogeneous, it is only essential how many cloud droplets are in the atmospheric column. Nevertheless, because LWP values from both instruments follow a similar trend, and the fact that the microwave retrieval is insensitive to cloud inhomogeneities, it can be concluded from this case study that the new cloud retrieval is applicable to inhomogeneous water clouds with limitations for optically thick clouds ($\tau > 40$).

5.1.3 Scattered Cloud Case

A time series of retrieved τ and r_{eff} of scattered liquid water clouds is shown in Figure 5.5 at 17.1 - 18.3 UTC for April 28, 2011 around 9°S and 4°W during ANT-XXVII/4. A typical photo of those clouds can be seen in the right panel of Figure 5.6. Six observed clouds are illustrated with gray shaded areas.

Cloud 1 and 2 show an increased τ at cloud edges, followed by a smaller value of τ , while r_{eff} decreases toward cloud edges and varies within the cloud. To analyze the temporal development of the retrieved cloud properties, Figure 5.6 shows the observed spectral transmissivity over the wavelength region from CORAS for cloud 1 (left panel). The temporal resolution

between 11 spectra is 15 s. The observed cloud is schematically illustrated in the photo from the full-sky imager with the red box. The cloud moves from the right to left corner, indicated by the red arrow. Observed spectra from time step t_1 to t_{11} are illustrated with colored lines. While $T_{\lambda,\text{obs}}(t_1)$ and $T_{\lambda,\text{obs}}(t_{11})$ refer to clear sky, the $T_{\lambda,\text{obs}}$ values ranging from t_2 to t_{10} refer to cloud observations. For clear sky observations in the VIS wavelength region the spectral shape of the spectra is dominated by Rayleigh scattering through the atmosphere. At t_2 a cloud spectrum was observed (compare to model results in Section 4.1.3), resulting in a retrieved τ and r_{eff} of 1.8 and 2.0 μm , respectively. 15 s later (t_3), an offset between VIS and NIR wavelength region in the transmissivity spectrum is obvious. The reason for this offset between both CORAS spectrometers is that radiance and irradiance measured with two spectrometers in each case are accessed in sequence and not simultaneously (see Section 3.2). First irradiances and radiances are measured by the VNIR spectrometers with a certain integration time t_{int} (here $t_{\text{int}} = 3000$ ms), followed by measurements using the SWIR spectrometers (here $t_{\text{int}} = 500$ ms). Usually, this is not a problem for homogeneous clouds but for scattered clouds this might cause such offsets in the observed transmissivity spectra. For $T_{\lambda,\text{obs}}(t_3)$ this means that the spectrum in the VNIR wavelengths between 450–950 nm probably refer to a cloud edge indicated by spectral features of both clear sky and cloud affected extinction properties. While the cloud propagates during the measurement of irradiance, the SWIR spectrometer for radiance detects cloud parts, as the magnitude of transmissivity between 950–2000 nm is larger. In the multi-wavelength retrieval cloud properties are inferred by a combination of all three transmissivity ratios. Therefore, the retrieval of τ and r_{eff} at t_3 results in 0.1 and 3.1 μm , respectively. While τ is more sensitive to VIS wavelength regions, here influenced by cloud edge, r_{eff} is more sensitive to NIR wavelength regions. The same spectral behavior is seen for t_4 , t_5 and t_{10} which represents again the cloud edge. The along-track footprint d_a of the radiance measurements is about 70 m, depending on the ship speed of 10 kn and t_{int} . The cross-track footprint d_c for clouds with a base height of 1670 m is about 33 m. If additionally the wind speed is increased (here 10.3 ms^{-1}), the temporal

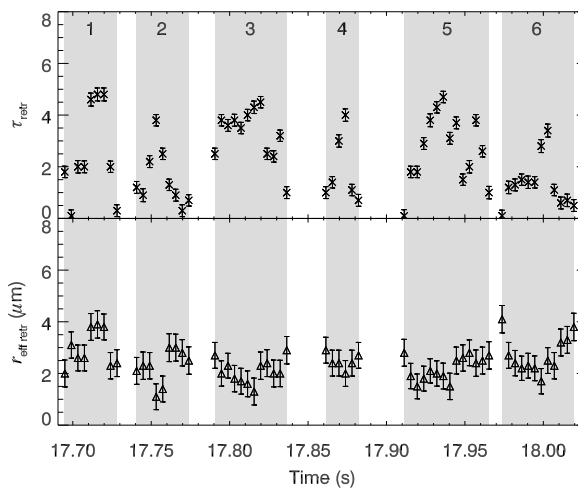


Figure 5.5: Time series of τ (upper panel) and r_{eff} (lower panel) at 17.7 - 18.3 UTC on April 28, 2011 around 9°S and 4°W from ANT-XXVII/4, based on retrievals using data from CORAS. Gray shaded time periods illustrates six liquid water clouds. Here, only successful retrieval results are shown ($\tau > 0.1$ and $r_{\text{eff}} > 0.1 \mu\text{m}$).

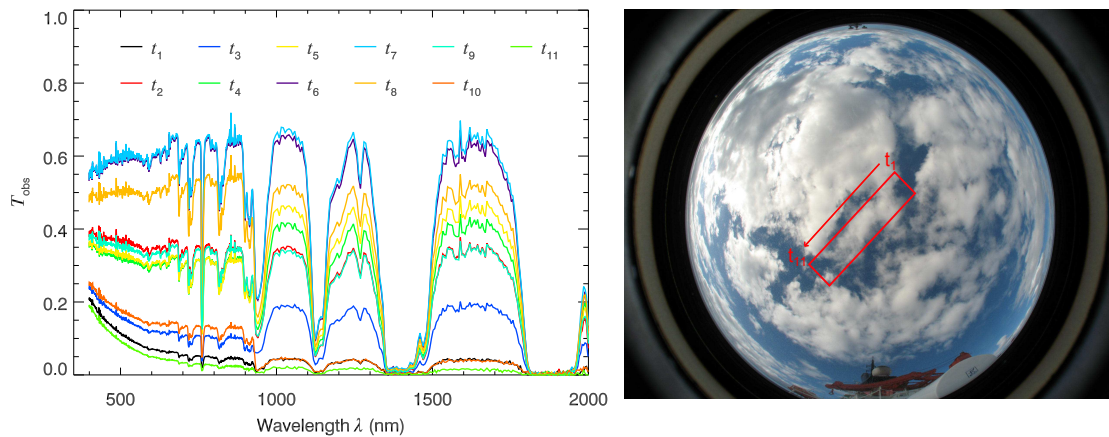


Figure 5.6: Observed spectral transmissivity from CORAS data for liquid water cloud 1 shown in Fig. 5.5. Spectra at time steps t_n ranging from t_1 to t_{11} are illustrated with different colored lines (left panel). Corresponding photo from full-sky imager of liquid water cloud 1. Red box schematically illustrates the observed cloud. The cloud moves from right to left corner of the picture (right panel).

development of scattered clouds is strained. This corresponds to a 1100 m spatial segment. The larger the wind speed and/or opposite direction of cloud movement, the smaller is the sampling resolution of radiance measurements. This characteristic should be considered for scattered clouds.

There are several studies which investigate the transition zone between cloudy and clear air. It is characterized as a region with strong aerosol–cloud interactions and increased humidity near cloud boundaries. The transition zone spans between 50 m and several hundred meters (Koren et al., 2007; Su et al., 2008; Redemann et al., 2009). Most aircraft, satellite and ground-based instruments have insufficient spatial and temporal resolution to resolve the transition zone (Chiu et al., 2009). Using 1 s resolution measurements of zenith radiance, Chiu et al. (2009) and Marshak et al. (2009) found a spectrally invariant behavior between ratios of transmissivity in the transition zone. Chiu et al. (2009) defined 5 regimes of the difference and the sum of transmissivity at 870 nm and 1640 nm. While regime 0 refers to cloud-free areas, regime 1 corresponds to the transition zone where τ is up to 0.2, where they found a linear relationship between the difference and the sum. For regime 2 to 4 with areas of τ with 1, 5, and $\tau > 5$, respectively, this relationship is nonlinear. Such high-resolution measurements could be approximated by low temporal resolution spectral transmissivity measurements using this simple linear relationship (Marshak et al., 2009). Offsets in the observed transmissivity spectra and the larger temporal resolution of CORAS showed more or less a sharp decrease of the spectral-invariant functions. Unfortunately, the time between cloud-free, transition zone and full cloudy parts is too short for applying this method to CORAS data.

For clouds 3 to 6 such offsets in the transmissivity spectra were not observed. Moreover, another characteristic of retrieved cloud properties was found. At cloud edges retrieved τ are small and increase toward the center of the cumulus cloud, while retrieved r_{eff} values are increased at cloud edges and slightly decrease toward the center of the cloud. The reason for this is that the plane-parallel approximation (1D) in the radiative transfer model

is not valid at cloud edges. Several studies discuss the radiative effects of cloud three-dimensional (3D) structure on 1D retrievals of τ (e.g., Varnai and Marshak, 2001, 2002b; Iwabuchi and Hayasaka, 2002; Horvath and Davies, 2004) and r_{eff} (e.g., Varnai and Marshak, 2002a; Iwabuchi and Hayasaka, 2003; Marshak et al., 2006) as derived from satellite observations. Marshak et al. (2006) found that 3D radiative effects influence the retrieval of r_{eff} in different ways. Averaging over larger scales decreases r_{eff} . Furthermore, they reported that shadowing tends to overestimate r_{eff} more than illumination underestimates r_{eff} with regard to the 1D plane-parallel assumption. As a result, on overall bias toward larger r_{eff} was found. By ignoring shadowing in 1D retrievals, r_{eff} is substantially overestimated while τ is underestimated. This effect is much more pronounced for scattered cumulus than for stratocumulus clouds (Marshak et al., 2006). Those 3D radiative effects of scattered liquid water clouds were also observed in the ship-based CORAS retrievals. To investigate 3D radiative effects on ground-based retrievals, 3D radiative transfer calculations are required in future work.

5.2 Cirrus

In this work only the optical properties of ice particles were used based on the parametrization of Baum et al. (2005a,b, 2007). Although it is known that ice crystal single scattering properties vary strongly with crystal shape (e.g., Macke et al., 1998; Yang et al., 2000; Wendisch et al., 2005), the Baum et al. (2005a,b, 2007) parametrization was assumed as best choice due to the lack of in situ information concerning the crystal shape. Eichler et al. (2009) investigated cirrus clouds over the North Sea using airborne spectral radiance measurements. Using different ice crystal habits (hollow columns, plates, solid columns, rough aggregates) and a mixture of ice crystal shapes in the radiative transfer calculations, they found best fits between observed and modeled radiances with smallest r_{eff} of 18 – 19 μm on average assuming hollow columns and rosettes, whereas a mixture based on Baum et al. (2005a,b, 2007) parametrization retrieved larger r_{eff} of 23 μm . The uncertainties related to an incorrect assumption of ice crystal shape for ground-based cirrus retrievals was investigated by Schäfer et al. (2013). Retrieving only τ_{ci} from visible radiance, they found enhanced sensitivity with respect to the ice crystal shape of up to 90% and to the surface albedo of up to 30%. The sensitivity of the retrieval method with regard to ice crystal radius and the cloud height can be neglected with deviations of $\leq 5\%$ and $\leq 0.5\%$. The single scattering properties (asymmetry factor, single scattering albedo) are more sensitive to different crystal shapes than to crystal size (Macke et al., 1998).

Taking into account the optical properties of ice particles in the model, cirrus microphysical properties were retrieved with the new multi-wavelength method. In Figure 5.7 retrievals of τ and r_{eff} of four cirrus clouds observed on April 20, 2012 around 25°S and 38°W are presented. Unfortunately, during ANT-XXVIII/5 the lidar was not on board and in many cases the cirrus was not detected by ceilometer because base heights were higher than the upper detection limit, but can clearly be identified in the sky images shown in Figure 5.8 and in the CORAS signals. The cloud base height was estimated using radiosonde data to be larger than 8.5 km. In all cases the cirrus can clearly be distinguished from clear sky

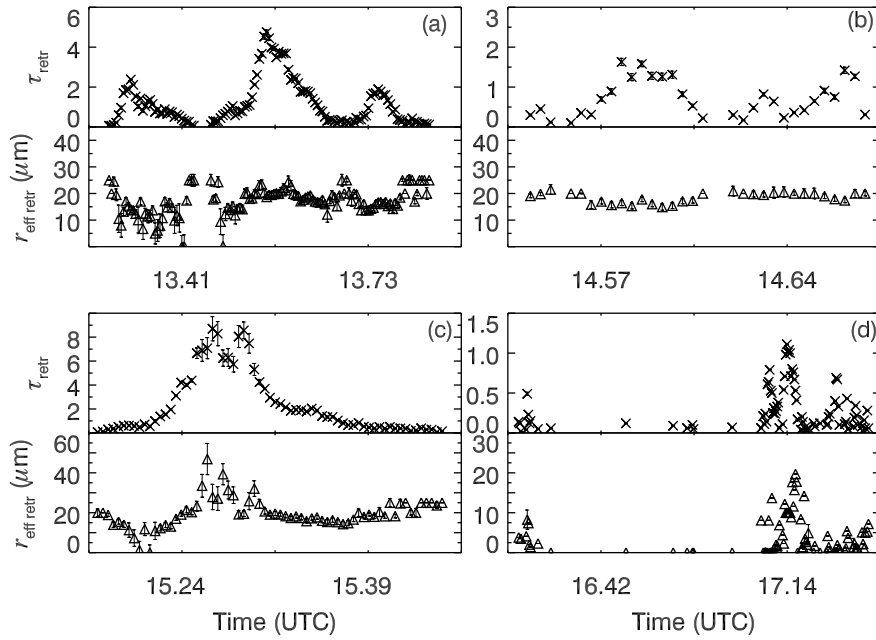


Figure 5.7: Time series of retrieved τ and r_{eff} of four cirrus clouds (a-d) observed on April 20, 2012 around 25°S and 38°W from ANT-XXVIII/5. Note the different scaling. The distance covered in the depicted time series ranges from 1 km to 30 km.

segments because of the changing spectral behavior in the NIR region in the presence of ice particles. Figure 5.7a and c show results for a thick inhomogeneous cirrus cloud. The mean values of τ are 1.1 ± 0.1 and 2.3 ± 0.2 , respectively. Mean values of r_{eff} are $16.9 \pm 2.2 \mu\text{m}$ and $19.5 \pm 2.9 \mu\text{m}$ with larger uncertainties, respectively. The effective radius is more homogenous in both cases. Furthermore, r_{eff} increases in the vicinity of cloud edges which might be caused by 3D radiative effects. Figure 5.7b presents a thinner cirrus with smaller τ of 0.6 ± 0.1 , and a relatively constant r_{eff} of $17.6 \pm 2.0 \mu\text{m}$. In Figure 5.7d retrieved data of a Cirrocumulus cloud are shown with thin and fractal parts. τ is around 0.4 ± 0.01 and an averaged r_{eff} of around $4.7 \pm 0.5 \mu\text{m}$. Due to large solar zenith angles around 17 UTC retrieving r_{eff} is often not possible because the measured radiance is too noisy and associated with larger uncertainties. However, all four cases illustrate, that cloud inhomogeneities can be resolved by CORAS measurements. For example, during the time series shown in Figure 5.7c, r_{eff} values vary by a factor of four due to spatial cirrus inhomogeneities.

To evaluate the retrieval results for cirrus obtained from spectral radiation measurements, a comparison with vertical extinction coefficient profiles obtained from lidar was done. For ANT-XXIX/1 lidar data from Polly^{XT} Arielle (Althausen et al., 2009) and data analysis programs are provided by TROPOS, Leipzig. The comparison of passive and active remote sensing applications requires a sensible selection of time periods. The data have to be limited to cirrus without the presence of underlying marine boundary layer (MBL) clouds. Here, the zenith radiance spectra would be influenced by liquid water droplets in the MBL clouds and ice crystals. A separation of contributions of liquid water and ice to the retrieval of τ and r_{eff} in the radiative transfer model is not possible (see Section 5.4). On the other hand, the cirrus should be thin enough that the laser could penetrate the cloud. For optically thick

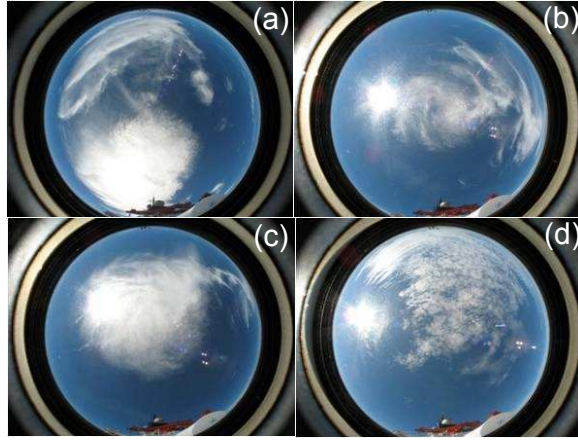


Figure 5.8: Photos of the full-sky imager on RV *Polarstern* from April 20, 2012 around 25°S and 38°W from ANT-XXVIII/5. Photos (a-d) corresponds to the measurement times in the time series in Fig. 5.7a-d.

cirrus the attenuation of electromagnetic radiation due to multiple scattering is stronger, and thus the signal-to-noise ratio above cloud top height is increased. Considering those criteria, a time period from 10.0 - 12.0 UTC on October 31, 2012 near the coast of Portugal was chosen for the intercomparison.

Figure 5.9a shows the temporal development of the range corrected signal at 1064 nm from lidar. In the upper troposphere between 8 – 10 km height, a cirrus cloud was observed. The marine boundary layer is located between 0 – 2 km. Within the MBL thin and fractal cumulus clouds are obvious indicated by red colors. Those liquid water clouds were nearly invisible in the photos from full-sky imager. The time series of retrieved τ of this cirrus cloud from CORAS measurements on October 31, 2012 between 10.0 - 12.0 UTC is illustrated in Figure 5.10. The cirrus is very inhomogeneous as the values of τ range between 0.2 and 2.7. Mean averaged τ and standard deviation is 1.20 ± 2.7 for the entire time series. A significant influence of the liquid water MBL clouds is not obvious in the retrieval time series since the clouds were very thin. These time periods were excluded from the comparison between lidar and spectrometer. During 10:30 - 11:25 UTC only cirrus was observed and used for the following analysis. The time period is illustrated in Figure 5.9a and Figure 5.10 with vertical white and black dashed lines, respectively.

To determine the optical parameters from lidar measurements, for elastic backscatter signals (during daytime) the Klett method was used (Klett, 1985). A constant ratio between particle extinction to particle backscatter coefficient has to be assumed. The particle lidar ratio $S_{\lambda}^{\text{par}}(R)$ in units of sr^{-1} is given with:

$$S_{\lambda}^{\text{par}}(R) = \frac{\alpha_{\lambda}^{\text{par}}(R)}{\beta_{\lambda}^{\text{par}}(R)}, \quad (5.3)$$

depending on the spatial resolution R of the lidar system. The particle lidar ratio is the most critical input parameter in the Klett method. It depends on microphysical, chemical and morphological properties of the particles and varies with height (Ansmann and Müller,

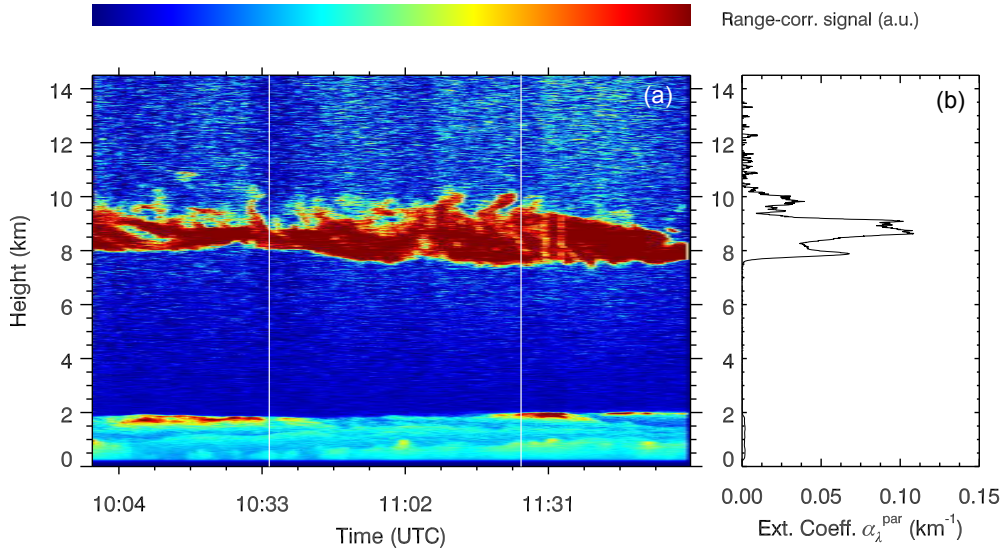


Figure 5.9: (a) Range corrected signal (in arbitrary units) at 1064 nm from October 31, 2012 obtained from Polly^{XT} Arielle aboard *Polarstern*. The marine boundary layer height is located around 2 km. A cirrus cloud is located between 8 – 10 km altitude. Vertical white lines indicates the analyzed time period. (b) Measured vertical extinction coefficient profile at 532 nm from lidar averaged over 5 minutes.

2005). Typical lidar ratios for marine particles at 532 nm were determined with a Raman lidar by Ansmann et al. (2001); Franke et al. (2001) ranging from $20 - 35 \text{ sr}^{-1}$. In this study a lidar ratio of 25 sr^{-1} was used to account also for multiple scattering (Wandinger, 1998). By substituting $\alpha_{\lambda}^{\text{par}}(R)$ with Eq. (5.3) and using the molecular lidar ratio $S^{\text{mol}} = 8\pi/3 \text{ sr}^{-1}$, the lidar equation (Fernald, 1984) can be solved to obtain the vertical profile of particle backscatter coefficient $\beta_{\lambda}^{\text{par}}(R)$ in units of $\text{km}^{-1}\text{sr}^{-1}$ (Sasano et al., 1985). Additionally, the vertical molecular backscatter coefficient must be known which is usually calculated with sufficient accuracy from standard atmosphere or actual radiosonde data (Ansmann et al., 1993). Furthermore, reference particle backscatter coefficients in a certain reference height have to be assumed. This height is chosen such that $\beta_{\lambda}^{\text{par}}(R)$ is minimized. Reference values for the particle backscatter coefficient of $5.0 \times 10^{-6} \text{ km}^{-1}\text{sr}^{-1}$ at 355 nm and $1.0 \times 10^{-6} \text{ km}^{-1}\text{sr}^{-1}$ at 532 nm and 1064 nm are used for the reference interval between 11.0 –

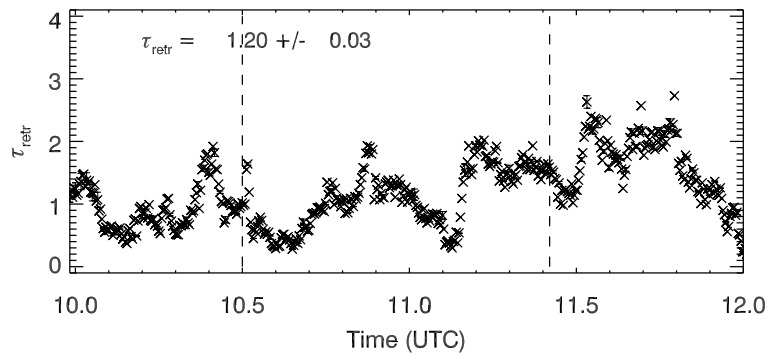


Figure 5.10: Time series of retrieved τ of a cirrus cloud observed on October 31, 2012 around 41°N and 11°W from ANT-XXIX/1.

12.5 km above the cirrus. Once the vertical profiles of $\beta_{\lambda}^{\text{par}}(R)$ are determined, the particle extinction coefficient in units of km^{-1} can be calculated using Eq. (5.3). As the cloud optical thickness is the vertical integral of the extinction coefficient (see Eq. (2.28)) for a cloud between cloud base and cloud top, τ can be determined from lidar measurements.

A measurement example from 10:50 - 10:55 UTC of vertical extinction coefficient at 532 nm is shown in Figure 5.9b. The cirrus cloud, located between 8.0–10.0 km is obvious since $\alpha_{\lambda}^{\text{par}}(R)$ increases up to values of 0.11 km^{-1} at 532 nm. The integration of extinction coefficient over altitude (with cloud boundaries $z_{\text{base}} = 8 \text{ km}$ and $z_{\text{top}} = 10 \text{ km}$) results in an optical thickness at 532 nm of $\tau = 1.02$. The associated uncertainty ranges between 15–20%. Using 5–minutes averages of lidar profiles, τ_{ci} was determined, see Table 5.1.

Table 5.1: Calculated 5-minute averages of τ_{ci} and error for the time period 10:30-11:25 UTC on October 31, 2012 from CORAS and lidar measurements.

Time (UTC)	τ_{ci} (CORAS)	τ_{ci} (lidar)	$\pm\delta\tau_{\text{ci}}$ (CORAS)	$\pm\delta\tau_{\text{ci}}$ (lidar)
10:30-10:35	0.90	0.16	0.02	0.02
10:35-10:40	1.03	0.14	0.01	0.02
10:40-10:45	0.46	0.25	0.02	0.04
10:45-10:50	0.57	4.73	0.02	0.71
10:50-10:55	1.07	1.02	0.03	0.15
10:55-11:00	1.32	0.97	0.02	0.15
11:00-11:05	1.29	0.15	0.02	0.02
11:05-11:10	1.02	0.23	0.03	0.03
11:10-11:15	0.61	0.98	0.01	0.15
11:15-11:20	1.46	0.65	0.03	0.10
11:20-11:25	1.61	0.42	0.03	0.06

The mean values of τ_{ci} of the time period for CORAS and lidar measurements are 1.03 ± 0.02 and 0.88 ± 0.13 , respectively. Mostly, τ_{ci} from lidar method is less than the τ retrievals of CORAS. The mean difference between both methods for the entire time period is 0.97. Larger discrepancies, for example at 10:45 - 10:50 UTC, are likely caused by an incorrect assumption of the constant lidar ratio. The values of particle backscatter and extinction coefficients above cirrus fluctuates. By reducing the lidar ratio from 25 sr^{-1} to 22 sr^{-1} or 20 sr^{-1} , values of τ_{ci} of 1.22 or 0.87 are determined, respectively. This clarifies the sensible assumption of lidar ratio. It can only be considered as a first guess, the true lidar ratio remains unknown (Ansmann and Müller, 2005). Cirrus cloud inhomogeneities are better resolved with the multi-wavelength cloud retrieval since the temporal resolution is larger and for relatively thin cirrus enough photons could penetrate the cloud. While the elastic lidar signals are strongly influenced by cloud microphysical and morphological properties.

5.3 Comparison of Slope and Multi-Wavelength Method

The comparison of the retrieval methods by McBride et al. (2011), hereafter named the slope method, and the multi-wavelength method are shown in Figure 5.11 for a time period from November 14, 2012 around 0°N and 11°E from ANT-XXIX/1. During this period low-level boundary layer clouds with a cloud base height of about 1 km were observed which is shown in the time series of backscatter coefficient from ceilometer data (Figure 5.11d). The geometrical thickness of the cloud ranges between 500 – 800 m. Cloud top heights were lower than the freezing level obtained from atmospheric sounding indicating a liquid water cloud. Ceilometer, as well as the lidar did not detect higher level cirrus. In Figure 5.11a–b the retrieval of τ and r_{eff} from the new multi-wavelength method (red symbols) and the slope method (blue symbols) is presented. The retrieved τ from both methods show similar results with mean values of 16.3 and 14.3 for the multi-wavelength and slope method, respectively. The mean difference between both approaches is 2.5 for the entire time series, while the differences in r_{eff} are larger with a mean difference of 4.4 μm . The multi-wavelength method

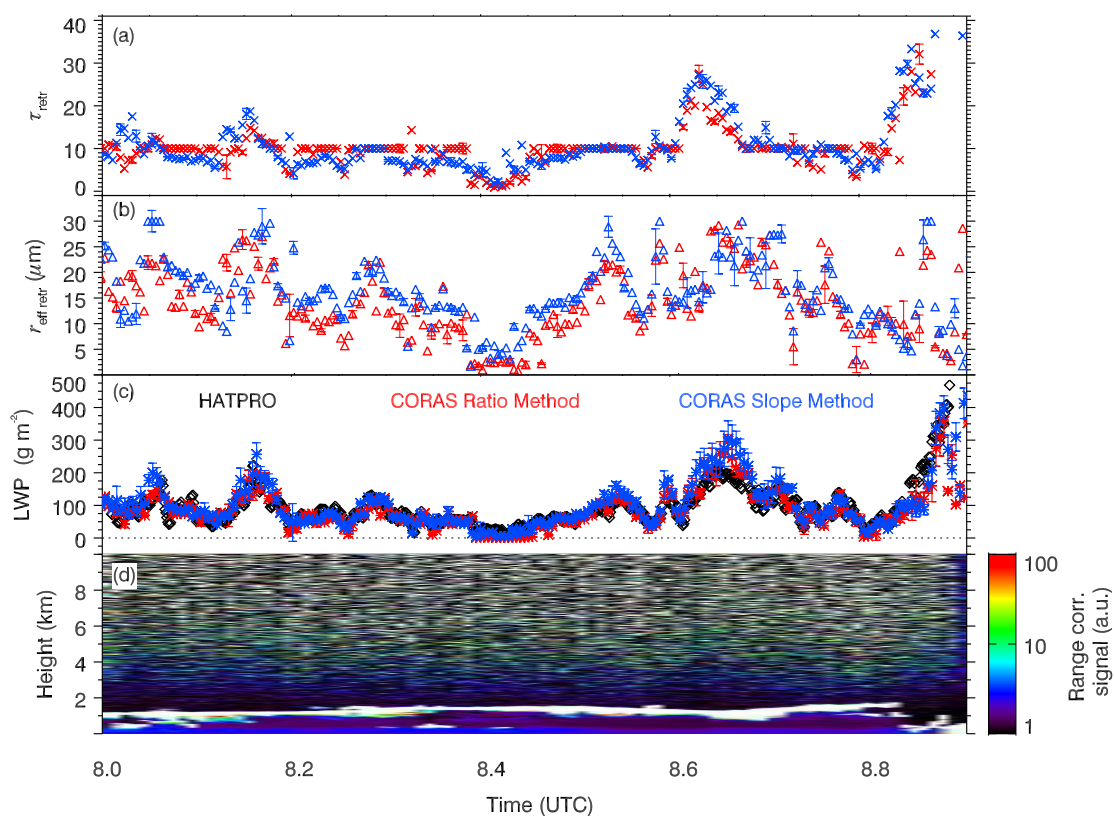


Figure 5.11: Time series of τ (a) and r_{eff} (b) at 8.0 - 9.0 UTC on November 14, 2012 around 0°N and 11°E from ANT-XXIX/1, based on two retrieval methods using data from CORAS. Retrieval results from the new multi-wavelength method are shown with red symbols, results from the slope method by McBride et al. (2011) in blue symbols. (c) Time series of LWP as retrieved from HATPRO (black diamonds), CORAS with multi-wavelength method (red crosses) and CORAS with slope method by McBride et al. (2011) (blue crosses). (d) Time series of vertical backscatter coefficient in arbitrary units (a.u.) obtained from ceilometer. The distance covered in the depicted times series is about 18 km.

retrieves smaller values of r_{eff} with $14.0 \mu\text{m}$ compared to $17.0 \mu\text{m}$ from the slope method. But in general, the agreement is within the uncertainties of the retrieved cloud properties from both methods. This is also evident in the time series plot of HATPRO LWP and the derived LWP using Eq. (5.2) shown in Figure 5.11c. Both retrievals matches the LWP observations from the microwave radiometer, except the later period where it starts to rain. Only around 8.6–8.68 UTC, the LWP derived from the multi-wavelength method matches more closely the LWP from HATPRO, because the slope method retrieves larger values of τ . Mean values of LWP and standard deviations are $139.8 \pm 26.3 \text{ g m}^{-2}$ for HATPRO, $126.9 \pm 10.6 \text{ g m}^{-2}$, and $142.5 \pm 17.7 \text{ g m}^{-2}$ for the multi-wavelength and slope method, respectively.

The uncertainties of τ , r_{eff} , and LWP from the multi-wavelength and slope methods along the time series from November 14, 2012 are shown in Figure 5.12. The retrieval uncertainty thresholds of ± 1 in τ , and $\pm 2 \mu\text{m}$ in r_{eff} are plotted with black dashed lines in Figure 5.12a–b. Eq. (4.8) was used to calculate the uncertainties in τ and r_{eff} for the multi-wavelength method. The uncertainties of the slope method were calculated as reported by McBride et al. (2011), but using the measurement uncertainty of CORAS spectrometers of 5.1% in the VIS wavelength region and 2.2% uncertainty in normalized transmissivity used for the spectral slope fit. Uncertainties of LWP were calculated using error propagation of uncertainties of τ and r_{eff} from both methods. As shown in Figure 5.12a, the multi-wavelength method does not significantly reduce the uncertainty in τ , since both methods (valid retrieval multi-wavelength method: 82%; valid retrievals slope method: 78%) stay below the threshold. Uncertainties increase around 8.18 UTC and 8.6 UTC as τ increases for both methods. Due to the use of ratios of transmissivity, the uncertainty in r_{eff} is significantly reduced for the multi-wavelength method. 80% of the retrievals passes the $2 \mu\text{m}$ threshold, whereas 66% valid retrievals were observed for the slope method. Uncertainties in r_{eff} under thicker clouds are reduced, which is also obvious in the LWP uncertainty shown in Figure 5.12c.

5.4 Uncertainty Discussion

It was shown in Section 4.3.2 that retrieval uncertainties are calculated by propagating the measurement uncertainties of three ratios of transmissivity through 64 solutions of the cost function. This procedure accounts for measurement uncertainties more thoroughly compared to retrieval uncertainties consisting of the maximum and minimum retrieval of τ and r_{eff} . Furthermore, it was shown in Section 5.3 that retrieval uncertainties are reduced for r_{eff} compared to the slope method by McBride et al. (2011).

Cloud phase misclassification (mixed-phase or multi-layer clouds) is the largest contributor to variability in zenith radiance. For example, a cloud consisting of liquid water droplets with $\tau_{\text{liquid}} = 5$ and $r_{\text{eff,liquid}} = 5 \mu\text{m}$ and additional ice crystals with values of $\tau_{\text{ice}} = 1$ and $r_{\text{eff,ice}} = 30 \mu\text{m}$, compared to an assumed cloud consisting of liquid water droplets only, leads to an overestimation of retrieved τ and r_{eff} of 74% and 182%, respectively. A separation of contributions from liquid water or ice is not possible. As the multi-wavelength cloud retrieval depends on several input parameters in the radiative transfer model, an error in the chosen thermodynamic phase leads to large uncertainties. The cloud base heights from ceilometer,

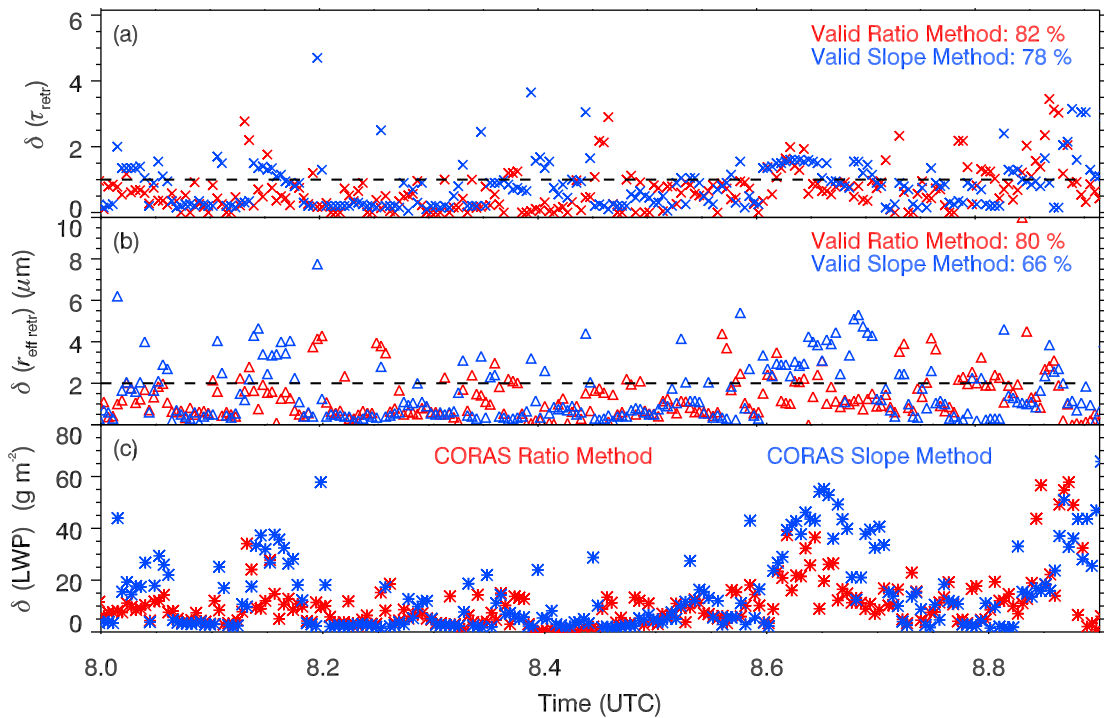


Figure 5.12: Time series of calculated uncertainties of (a) τ , (b) r_{eff} , and (c) LWP at 8.0 - 9.0 UTC on November 14, 2012 around 0°N and 11°E from ANT-XXIX/1. Uncertainties from the new multi-wavelength method are shown with red symbols, uncertainties from the slope method by McBride et al. (2011) in blue symbols. Black dashed lines in (a) and (b) shows the uncertainty threshold of 1 in τ , and $2\ \mu\text{m}$ in r_{eff} used to define valid retrievals.

in combination with sky images and atmospheric soundings from the ship, were used as an estimate of cloud phase. Clouds with a base height $< 2\ \text{km}$ and a cloud top height below the freezing level obtained from radiosonde data, were classified as liquid water clouds. Accordingly, clouds were classified as ice clouds with base heights $> 5\ \text{km}$ and top heights above the freezing level. The radiosonde data, and the associated determined freezing level, are only available around noon. If the meteorological conditions change during the measurements, it is possible that the position of the freezing level alter toward higher (and colder) altitudes which increase the probability of existing ice crystals. Similarly, clouds with a high vertical development (Cumulonimbus) cannot be clearly identified from the ground observations. In those cases, the assumed liquid water phase in the radiative transfer model cause large uncertainties in the retrieval. The uncertainties associated with an inaccurate determination of cloud top heights obtained from radiosonde data are in the range of 2 – 4%. When a cloud is relatively thick and the lidar cannot resolve higher level clouds, the comparison with microwave radiometer observations is often a good indicator for cloud misclassification as the radiometer is insensitive to ice clouds (Löhnert et al., 2007). Retrievals of LWP from HATPRO and CORAS significantly differ by a factor of up to 10. Furthermore, the cloud should consists of only one layer or multi-layer clouds under similar microphysical conditions. The comparison with MODIS data from satellite mostly confirms the assumption of single-layer clouds based on the assumptions from the daily atmospheric soundings on *Polarstern*.

It was highlighted in Section 5.1.3 that 3D radiative effects are an important contributor to

the retrievals of cloud properties. Scattered cumulus clouds are more affected than stratocumulus. Illuminated and shadowed cloud parts are possible biases in the overall measurements of zenith radiance. To solve this issue, 3D radiative transfer calculations are required. Considering the numerous measurements during three *Polarstern* cruises, this can certainly only be done statistically via LES calculations.

To account for uncertainties in the zenith radiances caused by the ship movements, an active horizontal stabilization platform would be desirable. In this work only data with a horizontal misalignment smaller than 5° were analyzed. Largest deviations from the horizontal reference plane occurs during storms or heavy swell or during the turns of the ship.

As discussed in Section 5.1, uncertainties in the retrieved cloud properties might come from the approximation of the adiabatic cloud model used in the radiative transfer calculations. Different studies report the impact of the vertical variation of r_{eff} on satellite retrievals (e.g., Chang and Li, 2002, 2003; Chen et al., 2007). As Platnick (2000) investigates in a theoretical study vertical photon transport through cloud layers, he demonstrates that the weighting function for transmissivity shows a symmetric weighting throughout the center layer of the cloud. Using vertical weighting functions of r_{eff} or LWC profiles in the radiative transfer model could help to understand and quantify the influence on calculated zenith radiance.

6 Statistical Cloud Analysis

While the previous chapter introduced representative cloud scenes and characteristics, this chapter concerned with a statistical cloud property analysis obtained from multi-spectral cloud retrieval from individual and all three *Polarstern* cruises. The analysis was performed for liquid water and cirrus clouds individually. Section 6.1 concentrates on liquid water clouds regarding their meridional distribution of cloud properties (Section 6.1.1), prevailing cloud classes (Section 6.1.2), and the frequency distribution of retrieved cloud properties (Section 6.1.3). All cirrus cloud properties are analyzed in Section 6.2. This chapter is completed in Section 6.3 with a comparison of ship-based and satellite-based cloud retrievals.

6.1 Liquid Water Clouds

A statistical analysis of the retrieved microphysical cloud properties for non-precipitating liquid water clouds is reported here. Precipitating clouds were sorted out using the rain sensor data from the microwave radiometer. Furthermore, data which did not pass the horizontal misalignment criteria described were excluded. To exclude multi-layer or mixed-phase clouds, atmospheric soundings from the ship in combination with satellite data from MODIS were used. Furthermore, longer time periods of clear sky situations were not considered. Thus, the subsequent statistical cloud analysis for liquid water clouds is only valid for the analyzed time periods which passed the above mentioned exclusion criteria. Altogether during the three Atlantic transects 105963 data points were analyzed using the multi-spectral cloud retrieval. About one third of data were sorted out.

6.1.1 Meridional Distribution of Cloud Properties

During the transects the ship passes different climate zones between 50°N - 50°S with different atmospheric conditions. While each cruise leg is characterized by local and temporary limited weather systems, there should be similarities in the cloud microphysical properties in certain climate zones. An exemplary illustration of 5-minutes-averages of retrieved cloud optical thickness (a), cloud effective radius (b), and liquid water path (c) along the ship track derived from CORAS is plotted in Figure 6.1 from ANT-XXIX/1. Corresponding graphics for the other two cruise legs can be found in the Appendix A. Colored dots represent mean values of retrieved cloud properties. Black and dark blue colors refer to smaller values while red colors indicate large mean values. All liquid water clouds and all cloud classes are illustrated. Missing data points (i.e., around 10°N - 20°N) which indicate cirrus or mixed-phase cloud scenes are not included in the figure. Certain regions with similar cloud properties are obvious.

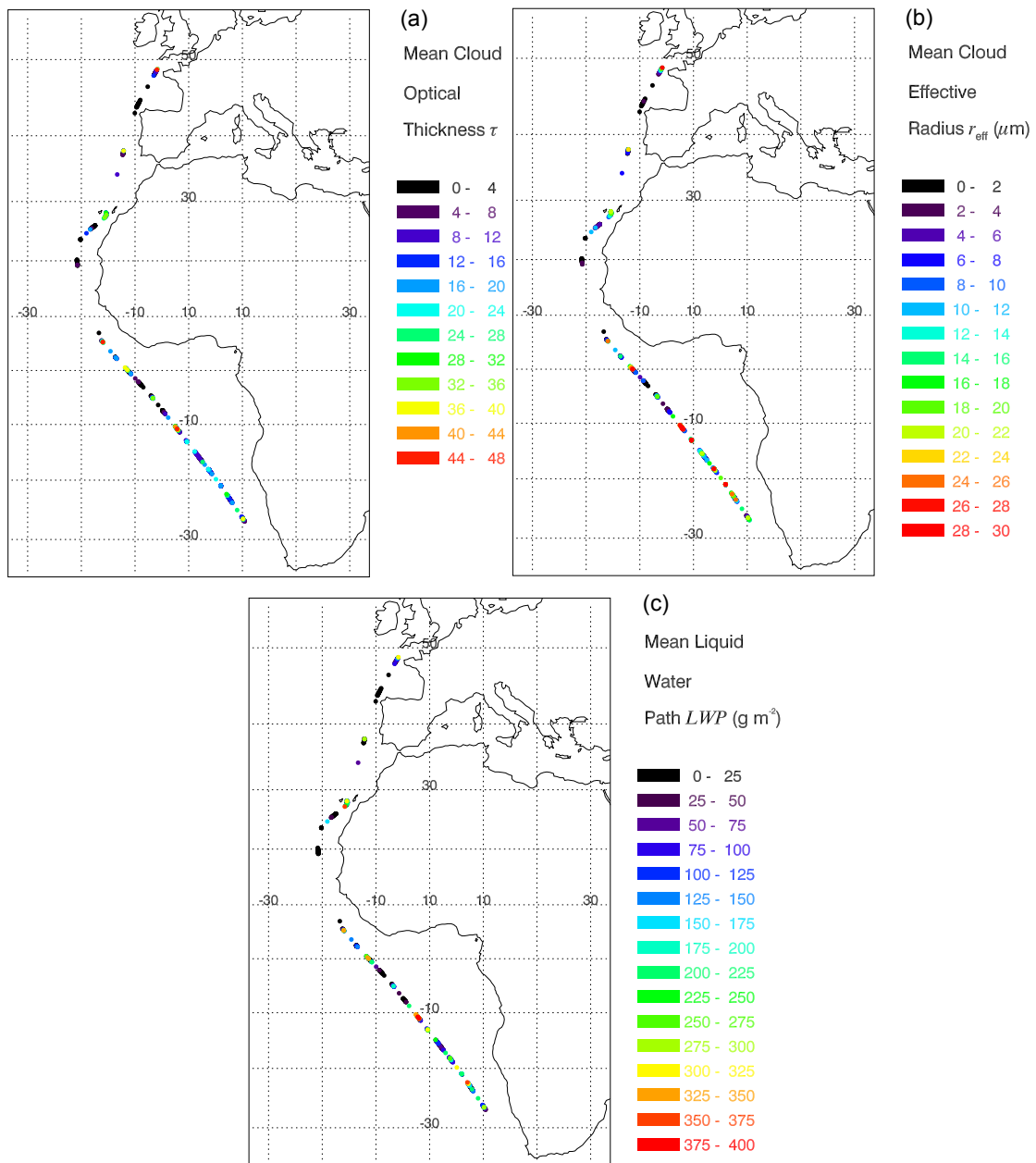


Figure 6.1: 5–minutes–averages of retrieved (a) τ , (b) r_{eff} , and (c) LWP along the ship track from October 29 to November 24, 2012 during ANT-XXIX/1. Data points include all liquid water clouds.

The region between 10°S - 30°S is characterized with variable mean values of all properties but mostly consistent clouds with mean values of $\tau > 10$ and $r_{\text{eff}} > 12 \mu\text{m}$. Due to a strong temperature inversion over the cold ocean, a stratocumulus layer formed near the west coast of Africa. The ITCZ around 0°N - 10°N is characterized by convective clouds indicated with larger mean values of τ and r_{eff} . It should be kept in mind, that the retrieval is only valid for single–layer clouds. Therefore, especially tropical deep convective clouds cannot be resolved with the multi–spectral cloud retrieval. Around the ITCZ there are regions with smaller mean values of τ , r_{eff} , and LWP representing the trade wind zone. The west wind zone between 30°N - 50°N is essentially influenced by a high pressure system in the Bay of

Biscay (see Section 3.1). Here, only small mean values of all cloud properties were observed. Whereas, near the English Channel distinct thunderstorms caused increased mean values of τ , r_{eff} , and LWP .

A meridional cross section of the retrieved cloud properties ranging from 50°S - 50°N is shown in Figure 6.2 for all cruises. It comprises all non-precipitating, single-layer liquid water clouds. Averages of τ , r_{eff} , and LWP (a-c) are plotted in 5° -latitude bins. The standard deviation is included by vertical bars. Additionally, the number of data points per latitude bin is illustrated with a dotted line in order to be able to assess how representative certain latitude bins are. On the one hand, the data set is limited to the analyzed time series. Therefore, fewer data points are available (e.g., for 10°N - 25°N). On the other hand, data availability depends on the speed of the ship. With a usual ship velocity of 10 kn and 10 hours of measurements per day, a distance of around 200 km is covered. The increased number of data points around 10°S - 25°S is due to more frequent stationary stops but mainly due to circadian consistent cloud coverage. The meridional cross sections for the individual cruises can be found in the Appendix A.

All cloud properties show a distinct meridional distribution. In the northern west wind zone between 30°N - 50°N latitude averages of τ , r_{eff} and LWP are mainly affected by storm tracks. Here, north Atlantic cyclons often associated with strong westerly winds cause low-level stratus followed by convective cumulus clouds. Therefore, largest averages of τ up to 20 and $r_{\text{eff}} > 20 \mu\text{m}$ were observed in the Bay of Biscay (40°N - 45°N).

A clear decrease in cloud property averages is obvious in the northern subtropics to tropics between 10°N - 30°N . Northeasterly trade winds cause typical shallow trade wind cumuli beneath the trade wind inversion (Stephens et al., 2001). All three retrieved quantities show a minimum in the northern subtropics. Between 10°N - 15°N the influence of dry Sahara air results in lowest observed averages of $\tau = 1.7$, $r_{\text{eff}} = 4.1 \mu\text{m}$, and $LWP = 10 \text{ g m}^{-2}$. Comparable results were found by Zoll (2012) which analyzed the microwave radiometer data from HATRPO obtained from eight *Polarstern* transects between 2007-2011.

The tropical region between 5°S - 10°N is mainly influenced by convective clouds in the ITCZ and thus increased values of cloud properties were observed. As the data contain transects from April/May (ANT-XXVII/4, ANT-XXVIII/5) and from October/November (ANT-XXIX/1), the location of the ITCZ changes within these months. For both cruises in April/May the ITCZ is located more central around 5°S - 5°N , whereas in October/November it is located north of the equator around 5°N - 10°N . The convergence zone is well defined over the ocean because the convection is constrained by the distribution of ocean temperatures. The exact extent of the ITCZ cannot be determined since deep convective clouds complicates the application of the retrieval.

The southern tropics and subtropics between 5°S - 30°S are influenced by the southeasterly trade winds. In contrast to the northern subtropics, larger averages of τ , r_{eff} and LWP were observed, which is mainly due to the increased frequency of stratocumulus clouds formed under a strong temperature inversion. Furthermore, the increased number of data points in these latitudes causes a more smoothed pattern in the cloud properties.

Data in the southern west wind zone between 30°S - 50°S arise from the cruise leg Punta

Arenas–Bremerhaven. Here, the meteorological conditions were characterized by storms near the Drake Passage. Larger averages of τ , r_{eff} and LWP were observed due to increased occurrence of convective cumulus clouds.

With only three available expeditions a representative meridional distribution of cloud properties cannot be derived. On that account, a wide range of those transatlantic cruises are necessary. The influence of weather systems prevails compared to typical cloud distributions in climate zones.

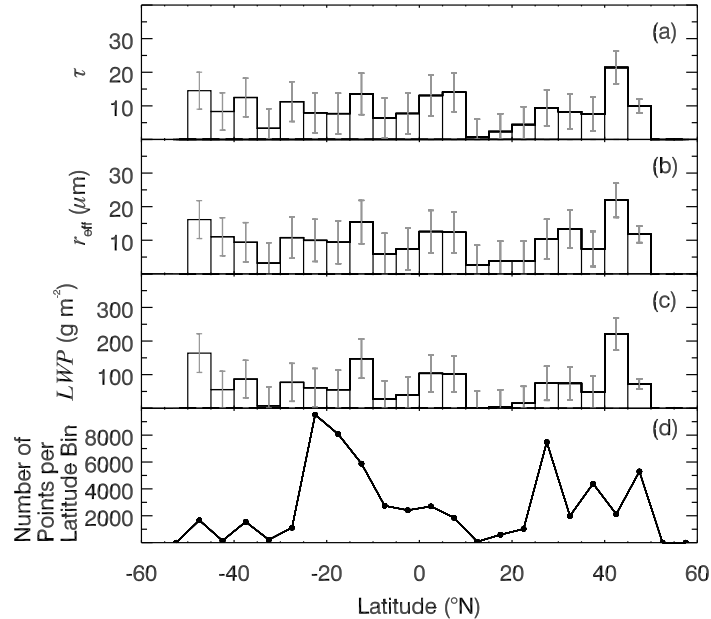


Figure 6.2: Meridional 5°-latitude-averages of retrieved (a) τ , (b) r_{eff} , and (c) LWP , and (d) number of retrieval points per latitude bin from 50°S - 50°N from all RV *Polarstern* cruises. Data points include all liquid water clouds.

6.1.2 Cloud Classification

There are distinct differences in the microphysical properties for homogeneous, inhomogeneous and scattered cloud scenes. To account for these characteristics, it is reasonable to classify all liquid water clouds into certain cloud classes. An automated cloud type classification algorithm, introduced by Heinle et al. (2010), is based on sky images provided from the full-sky imager. This cloud type classification is inappropriate for the data set presented in this work because of the different field-of-views from CORAS and HATPRO compared to sky imager. For example, a sky which is barely half of clear sky and a stratocumulus layer would be classified by the algorithm as stratiform cloudiness. But if the ship passes the cloudless part, CORAS and HATPRO with a small field-of-view of 2° would detect no clouds. Therefore, the cloud type was classified by hand for the three cruises using the observations from sky imager and spectrometer.

Liquid water clouds were separated into three cloud classes. The classification is based on the cloud classification for low liquid water clouds according to the DWD-key table for

observations on sea. A summary of the cloud classes is given in Table 6.1 and exemplary photos are presented in Figure 6.3. Cloud class '1' includes scattered clouds, cloud class '2' comprises homogeneous clouds like stratocumulus, and cloud class '3' inhomogeneous clouds which includes clouds before and after precipitation. Clear sky events were summarized in cloud class '0'.

A detailed listing for each cruise leg is given in Table 6.2. The resulting cloud classification is presented as histograms in Figure 6.4 for the three individual cruises (a-c) and all cruises (d). Considering first all three cruises, it was found that homogeneous stratocumulus (cloud class 2) are the prevailing clouds along the ship tracks. Here, the two cruise legs between Cape Town and Bremerhaven (Figure 6.4(a,c)) mostly contribute to these clouds. Stratocumulus priority forms over the colder ocean of the west coast of Africa. Accordingly, fewer stratocumulus clouds were observed for the cruise leg between Punta Arenas and Bremerhaven (Figure 6.4(b)). Considering the annual global distribution of low-level clouds over the oceans (see Figure 1.2(a)), the ship-based observations agree with the global observations from *CloudSat/Calipso*, although the ship tracks represent only a small segment of

Table 6.1: Cloud classes for liquid water clouds used in the subsequent statistical cloud analysis.

Cloud class	Cloud type
0	Clear sky
1	Cumulus humilis or fractus Cumulus congestus or mediocris Cumulus calvus
2	Stratocumulus cumulogenitis Stratocumulus stratiformis
3	Stratus nebulosus or fractus Bad weather Stratus or Cumulus Cumulus and Stratocumulus in different altitudes Cumulonimbus cappilatus

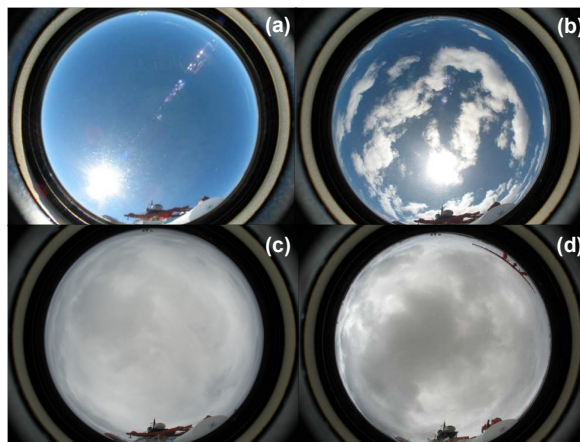


Figure 6.3: Photos of typical clouds for (a) cloud class '0', (b) cloud class '1', (c) cloud class '2', and (d) cloud class '3' from full-sky imager.

this distribution. With about 43% of data points cloud-free parts were observed. Here, all cloud classes, but mostly scattered clouds (cloud class 1) with large time periods of clear sky, contribute to this. Inhomogeneous and scattered clouds were almost equally observed for all cruises (Figure 6.4(d)). Looking at each cruise separately, there are some differences. For cruise leg ANT-XXVIII/5 the prevailing cloud class are inhomogeneous clouds (Figure 6.4(b)). This coincides with the meteorological observations reported in Section 3.1. The cruise leg was dominated by several storm tracks. While for the other two cruises only 24% of all data were not analyzed, for ANT-XXVIII/5 about one half of data were excluded from the analysis. This is due to the observed dust event (April 30 - May 3, 2012) but also due to enhanced precipitation and mixed-phase clouds. While ANT-XXVII/4 (Figure 6.4(a)) and ANT-XXIX/1 (Figure 6.4(c)) have more or less the same cruise tracks but representing spring and fall (in the northern hemisphere), no seasonal differences were found.

Table 6.2: Number of data points for cloud classification including the analyzed and excluded data of liquid water clouds for the three individually cruise legs and all cruises.

Cruise leg	Cloud class				Analyzed	Not analyzed	Total
	0	1	2	3			
ANT-XXVII/4	13368	3183	12697	521	29769	9789	39556
ANT-XXVIII/5	16914	3311	3647	8233	32105	30499	58023
ANT-XXIX/1	14867	3183	21777	3870	44089	13934	62604
all cruises	45149	9945	38121	12624	105963	54220	160183

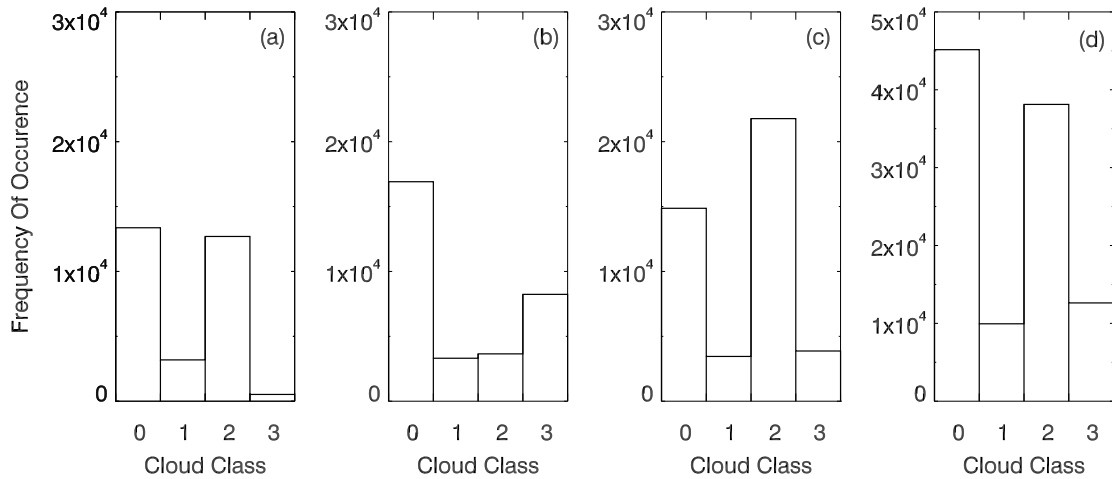


Figure 6.4: Histograms of determined cloud classes for liquid water clouds for (a) ANT-XXVII/4, (b) ANT-XXVIII/5, (c) ANT-XXIX/1, and (d) all cruises.

6.1.3 Histograms of Cloud Properties

Descriptive statistic is used to analyze the retrieved cloud properties from spectral radiation measurements along the ship track. The distribution of τ , r_{eff} , and LWP is illustrated in histograms in Figure 6.5. Data comprises all cloud classes from all cruises. Additionally,

the five-number summary including the minimum, the first quartile (or 25th percentile) P_{25} , the median, the third quartile (or 75th percentile) P_{75} , and the maximum of the respective distribution is given.

The range of the distribution, which is defined by the minimum and maximum value of observations, represents the retrieval limits. A cloud is defined when at least the minimum value of 0.1 in τ is retrieved. More explicitly, this means that a very thin cloud (i.e., in the transition zone between cloud free and cloud parts) is seen in the VIS spectrum of zenith radiance (sensitive to τ), but not yet in the NIR spectrum (sensitive to r_{eff}). As a result, the retrieval of r_{eff} would be not successful. For this reason, the range of the distributions are 0.1 – 80.0 in τ , and 0.0 – 30.0 μm in r_{eff} . As the LWP is calculated using the adiabatic approximation (Eq. (5.2)), the LWP range is 0.0 – 1333.3 g m^{-2} . Using the median instead of the arithmetic mean value of a distribution has the advantage that the half percentile range is symmetric distributed around the median. The median of the τ , r_{eff} and LWP distribution from all cruises is 6.6, 7.7 μm , and 29.2 g m^{-2} , respectively. To be independent on the assumption of a normal distribution, the interquartile range IQR and percentile range PR are used instead of standard deviation and variance as measures of spread, with:

$$IQR = P_{75} - P_{25}, \quad (6.1)$$

$$PR = P_{90} - P_{10}. \quad (6.2)$$

The IQR is a relatively robust statistic compared to the range and standard deviation. Furthermore, it is used to characterize the data when there are outliers that skew the data. The exact values for τ , r_{eff} and LWP are given in Table 6.3 which summarizes the statistics of each individual cloud class and all classes. Corresponding histograms and statistics for each cruise leg can be found in Appendix B.

For the τ distribution (Figure 6.5a), 80% of data are smaller than 18.4, whereas only 20% larger values were observed. While r_{eff} is distributed wider over the data range (Figure 6.5b), the largest frequencies occur for $r_{\text{eff}} \leq 3 \mu\text{m}$. The increased frequency for $r_{\text{eff}} = 30 \mu\text{m}$ results from the upper limit of the retrieval. As discussed in Section 5.1.1, the multi-spectral retrieval has problems in thick clouds and drizzle in the atmosphere. The spread of LWP values is relatively large (Figure 6.5c), meaning that only 20% of all data have a $LWP > 328.3 \text{g m}^{-2}$. It is remarkable that all cloud properties are distributed toward smaller values. Largest frequencies occur for clouds with $\tau \leq 2$ and $r_{\text{eff}} \leq 3 \mu\text{m}$. The distributions are greatly influenced by very thin clouds. Therefore, the statistic listed in Table 6.3 is translocated toward smaller values.

To classify these results, the same procedure was applied to the individual cloud classes. This is shown in Figure 6.6, while (a-c) presents cloud properties from cloud class 1, (d-f) cloud class 2, and (g-i) cloud class 3. The respective statistic is given in Table 6.3. For cloud class 1, which comprises 16% of all analyzed clouds, relatively small medians were calculated. This originates from the fact that 3D radiative effects are important for the radiative field of scattered clouds. Those inhomogeneous cloud parts influence the retrieval of τ and r_{eff} . As

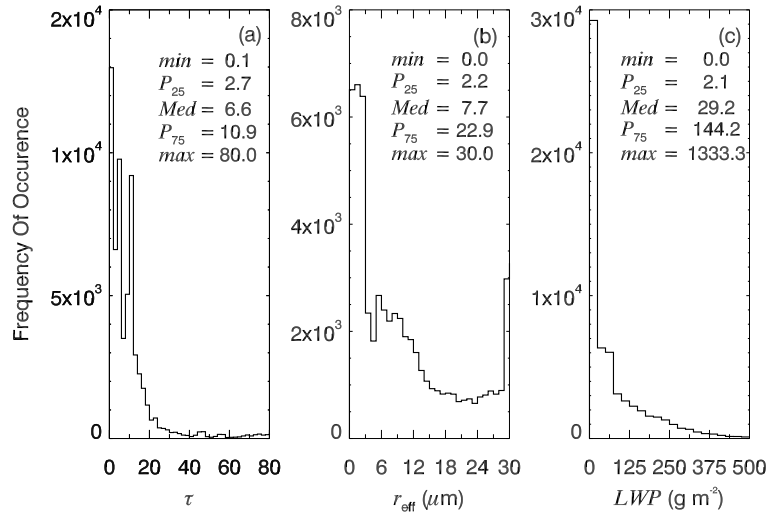


Figure 6.5: Histograms of retrieved (a) τ with binsize of 2, (b) r_{eff} in units of μm with binsize of $1 \mu m$, and (c) LWP in units of $g m^{-2}$ with binsize of $25 g m^{-2}$, containing all liquid water cloud classes from all *Polarstern* cruises. Numbers indicates minimum, first quartile, median, third quartile, and maximum value of the respective distribution.

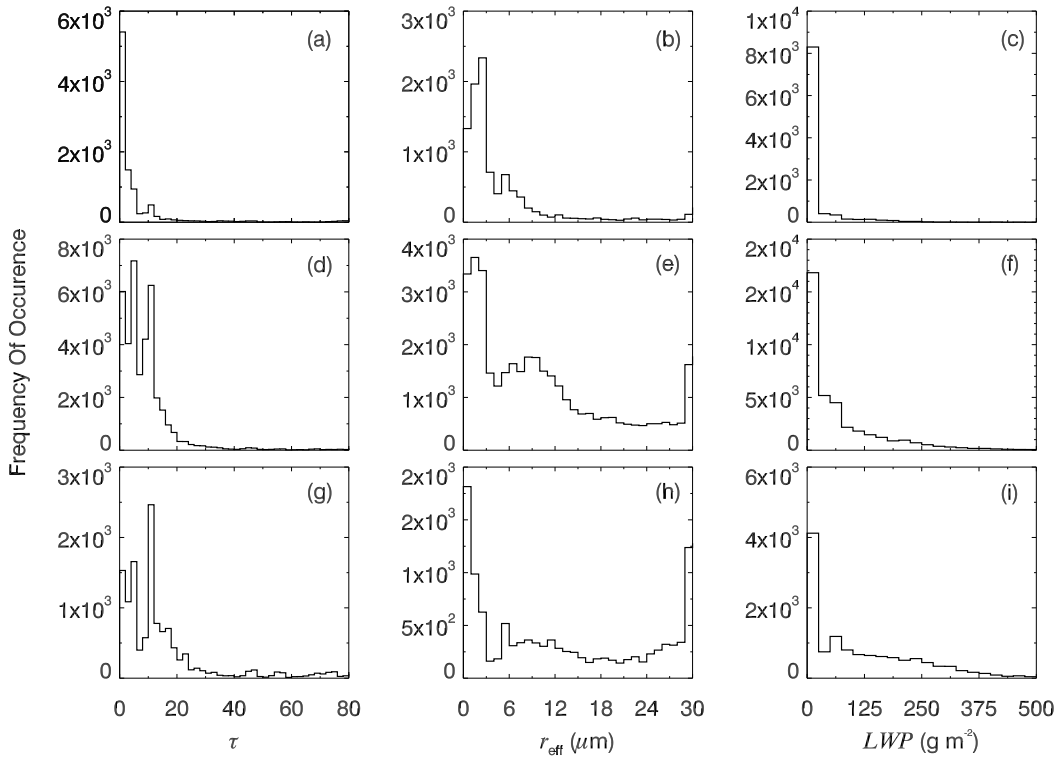


Figure 6.6: The same as Figure 6.5 separated into (a-c) cloud class 1, (d-f) cloud class 2, and (g-i) cloud class 3, containing all liquid water clouds from all *Polarstern* cruises.

reported in Section 5.1.3, in the transition zone between cloud free and cloud parts, τ is very small while r_{eff} is increased. This is clarified in the histograms in Figure 6.6a,b for smaller values of τ and r_{eff} . Although there is no consistent definition in the literature when a 'real' liquid water cloud starts in terms of τ and r_{eff} , it should be mentioned that a high amount of

Table 6.3: Minimum, first quartile, median, third quartile, maximum, interquartile range, and percentile range values of retrieved cloud properties for individual and all cloud classes containing data from all cruises.

		<i>min</i>	<i>P</i> ₂₅	<i>med</i>	<i>P</i> ₇₅	<i>max</i>	<i>IQR</i>	<i>PR</i>
cloud class 1 (<i>N</i> = 9945)	τ	0.1	0.5	1.6	4.9	80.0	4.4	13.1
	r_{eff} (μm)	0.0	1.6	2.5	6.0	30.0	4.4	13.9
	<i>LWP</i> (g m^{-2})	0.0	0.5	1.7	9.0	1333.3	8.5	66.3
cloud class 2 (<i>N</i> = 38121)	τ	0.1	3.8	7.3	10.2	80.0	6.4	15.5
	r_{eff} (μm)	0.0	2.5	8.7	17.2	30.0	14.7	27.0
	<i>LWP</i> (g m^{-2})	0.0	3.8	35.0	99.0	1333.3	95.1	206.0
cloud class 3 (<i>N</i> = 12624)	τ	0.1	4.6	10.0	16.8	80.0	12.2	31.0
	r_{eff} (μm)	0.0	2.3	12.0	27.0	30.0	24.7	29.9
	<i>LWP</i> (g m^{-2})	0.0	2.7	81.9	204.0	1333.3	201.3	308.4
all cloud classes (<i>N</i> = 60690)	τ	0.1	2.7	6.6	10.9	80.0	8.2	18.4
	r_{eff} (μm)	0.0	2.2	7.7	22.9	30.0	20.7	29.1
	<i>LWP</i> (g m^{-2})	0.0	2.1	29.2	144.2	1333.3	143.1	328.3

not neglectable small values of τ and r_{eff} were observed during the three *Polarstern* cruises. Another behavior was characterized for homogenous clouds in cloud class 2. This comprises almost 63% of all analyzed clouds. Although there is also an increased number of observations with small values which might be influenced by 3D effects, the medians of τ and r_{eff} with 7.3 and 8.7 μm show comparable results to values reported in other studies. McBride et al. (2012) found r_{eff} ranging from 5 – 15 μm for stratocumulus clouds; LeBlanc et al. (2014) found r_{eff} ranging from 3 – 15 μm for homogeneous clouds. Inhomogeneous clouds in class 3 are characterized by a wide range of retrieved τ , r_{eff} and *LWP* values. Medians are 10.0, 12.0 μm , and 81.9 g m^{-2} , respectively. The large spread of *IQR* and *PR* reflects the inhomogeneous behavior of those clouds. As this cloud class includes also clouds before and after rain periods, a lot of r_{eff} values around (or above) 30 μm were observed.

It is obvious that 3D radiative effects influence the retrieval distributions at cloud edges. The plane-parallel assumption in the radiative transfer model is not valid. These effects are emphasized for scattered cumulus clouds in cloud class 1. As a result, the statistic is heavily influenced by those fuzzy and fractal broken clouds. The median of τ and r_{eff} are shifted toward smaller values. To consider 3D radiative effects in the analyzed data of liquid water clouds, data were filtered by applying a cloud step filter, which is introduced in the following.

An example of clouds categorized in cloud class 1 is given in Figure 6.7. While (a) shows unfiltered data, (b) illustrates data filtered with cloud step. For the time series in (a) 4 clouds are shown which are highlighted with grey shaded areas. A cloud is detected, when at least retrieved τ is 0.1. Cloud 1 is a small cloud with regard to the spatial extent. As the temporal resolution between the retrievals is usually 15 s, the cloud was observed in between 45 s with two values from cloud edge and one from the center of the cloud. Cloud 2 is a cumulus cloud with a distinct center with increased values of τ and 3D radiative effects at cloud edges with increased r_{eff} (compare to Section 5.1.3). The two following clouds are very thin with small values of τ and r_{eff} . Between cloud 3 and 4 there is only a small gap where

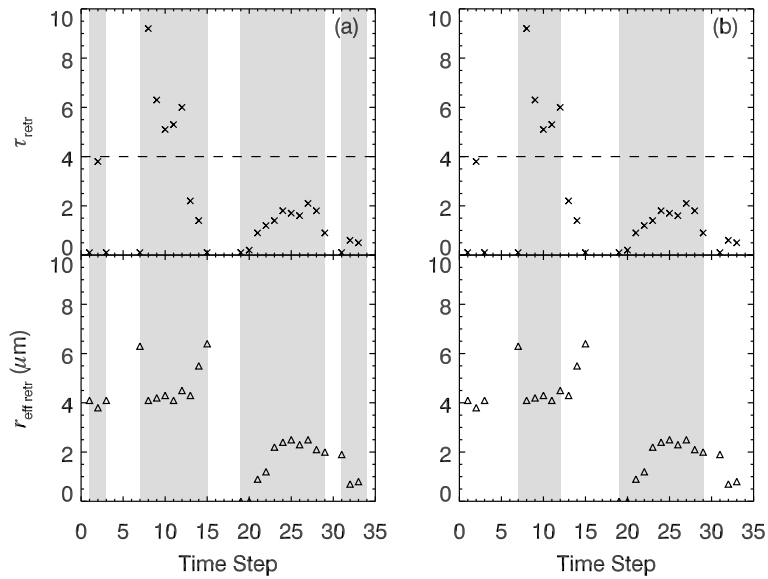


Figure 6.7: Schematic illustration of cloud step filter. Grey shaded areas illustrates the analyzed cloud while (a) is without cloud step filter and (b) is with cloud step filter.

clear sky was observed. An average of τ and r_{eff} over the time series is dominated by those edge effects.

According to the definitions of transition zone and cloud edges by Chiu et al. (2009), a cloud step filter was defined using a simple criteria for retrieved τ with:

$$\tau_{\text{cloud step}} = \tau(t_i) + \tau(t_{i+1}) \geq 4, \quad (6.3)$$

while $i = 0, \dots, N$ CORAS measurements. To fulfill the cloud step, the sum of two sequenced retrieved τ have to be greater or equal than a threshold of $\tau = 4$. This is illustrated in Figure 6.7 with a horizontal dashed line. As a consequence, thresholds of successive pairs of τ are given. These are either the pairs $\tau_1 = 0.1$ and $\tau_2 = 3.9$ or $\tau_1 = 2.0$ and $\tau_2 = 2.0$, where a cloud is defined. This means that retrievals at cloud edges with increased uncertainty due to 3D radiative effects are sorted out as soon as they do not pass these thresholds. Additionally, thin clouds that do not meet Eq. (6.3) but can be observed for more than 8 time steps (2 minutes) with $\tau > 0$ are also included in this analysis. This time threshold is a reasonable compromise to account for typical measurement conditions during *Polarstern* cruises (t_{int} , ship speed or wind speed). Applying both thresholds to the time series in Figure 6.7 yields only 2 of 4 defined clouds. Cloud 1 and 4 do not pass the cloud filter since sequenced τ pairs are smaller than 4. While cloud 3 conforms to the unfiltered counterpart in (a) with respect to the temporal extent, cloud 2 is shortened as the last 3 values do not pass the cloud step filter. As a result, the uncertain retrieval at the cloud edge are removed. Averaged values of τ increases while r_{eff} decreases.

It is obvious that the results of the filtered data heavily depends on the defined thresholds. Different thresholds were tested. Using the calculated retrieval uncertainties to identify biased values was not successful. Uncertainties of retrieved τ and r_{eff} at cloud edges were not

significantly increased. For that reason, a threshold has to be defined which is applicable to the huge data set, and additionally, is suitable to provide a sufficient number of remaining useful data. In other words, for a broken cloud scene a reduction of the cloud step to $\tau = 1$ or $\tau = 2$ yields a remaining data set of 65% or 55%, respectively. About two third or half of the retrieval is still biased because of the temporal resolution of the CORAS measurements reported in Section 5.1.3. With a better resolution probably a more clearer threshold can be given. Chiu et al. (2009) defined the transition zone and cloud edges using 1 s resolution measurements of zenith radiance although they did not retrieve cloud properties. Accordingly, an increase of cloud step results in an abruptly decrease in remaining data. The threshold of $\tau = 4$ used in this work comprises the above mentioned requirements best.

The statistics of cloud step filtered data of liquid water clouds are presented in Figure 6.8 and Figure 6.9 for all clouds and cloud classes, respectively. By comparing Figure 6.8 with Figure 6.5 for unfiltered data, it is obvious that the frequencies for small τ and r_{eff} are reduced.

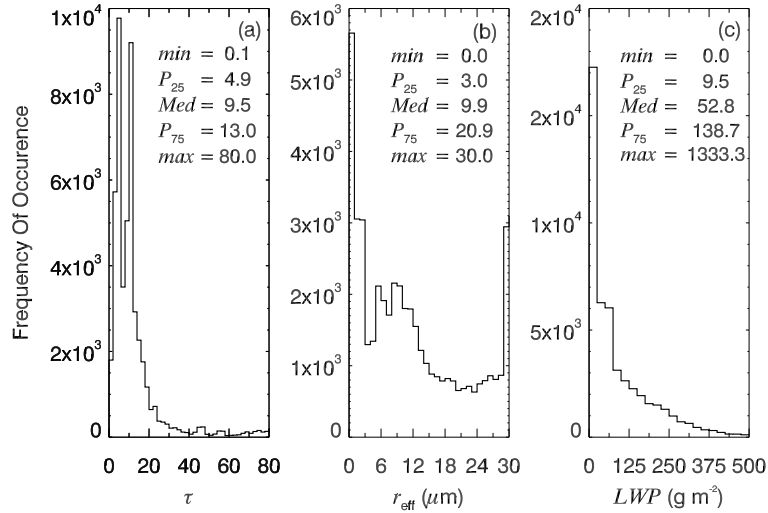


Figure 6.8: Same as Figure 6.5 but including cloud step filtered data.

Table 6.4: Same as Table 6.3 but including cloud step filtered data.

		<i>min</i>	P_{25}	<i>med</i>	P_{75}	<i>max</i>	<i>IQR</i>	<i>PR</i>
cloud class 1	τ	0.1	3.4	5.0	10.9	80.0	7.5	31.2
($N = 4722$)	$r_{\text{eff}} (\mu\text{m})$	0.0	1.4	3.0	7.2	30.0	5.8	22.1
$\hat{=} 47.5\%$	$LWP (\text{g m}^{-2})$	0.0	1.7	10.3	53.6	1333.3	51.9	151.9
cloud class 2	τ	0.1	4.9	8.9	11.4	80.0	6.5	14.1
($N = 32631$)	$r_{\text{eff}} (\mu\text{m})$	0.0	4.5	10.0	19.2	30.0	14.7	27.9
$\hat{=} 85.6\%$	$LWP (\text{g m}^{-2})$	0.0	12.0	48.9	116.8	1333.3	104.9	218.9
cloud class 3	τ	0.1	5.4	10.2	17.8	80.0	12.4	34.4
($N = 11282$)	$r_{\text{eff}} (\mu\text{m})$	0.0	5.0	14.1	27.9	30.0	22.9	30.0
$\hat{=} 89.4\%$	$LWP (\text{g m}^{-2})$	0.0	26.4	105.0	221.0	1333.3	194.6	317.9
all cloud classes	τ	0.1	4.9	9.5	13.0	80.0	8.1	18.8
($N = 48745$)	$r_{\text{eff}} (\mu\text{m})$	0.0	3.0	9.9	20.9	30.0	17.9	29.1
$\hat{=} 80.3\%$	$LWP (\text{g m}^{-2})$	0.0	9.5	52.8	138.7	1333.3	129.2	248.1

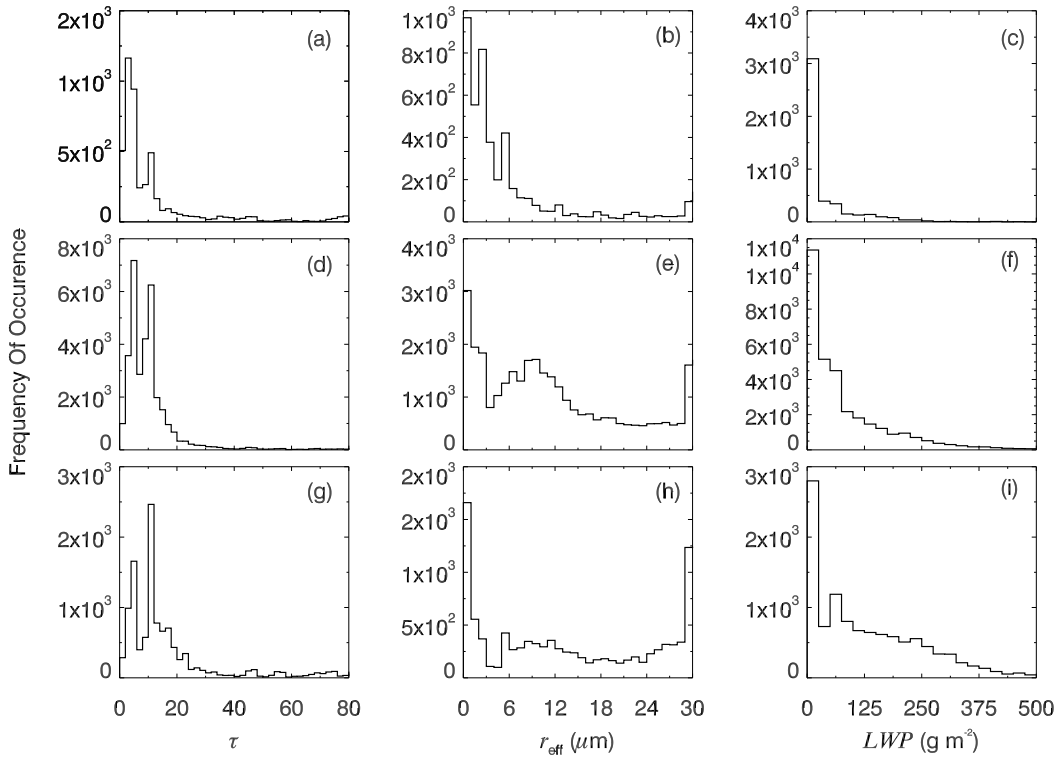


Figure 6.9: Same as Figure 6.6 but including cloud step filtered data.

About 20% of data were sorted out. The median of the τ , r_{eff} , and LWP distribution from all cruises is 9.5, 9.9 μm and 52.8 g m^{-2} , respectively. This corresponds to a percentage increase in τ and r_{eff} median of about 40%. Also the location of P_{25} and P_{75} is shifted towards larger values and most of the biased cloud properties were excluded by applying the cloud step filter. As expected, largest influence on cloud property distributions occur for cloud class 1 (Figure 6.9a-c). Here, almost 48% of retrievals were sorted out. The median of τ , r_{eff} , and LWP distributions is 5.0, 3.0 μm and 10.3 g m^{-2} , respectively. Although data were significantly reduced, this agrees better to other studies which focus on scattered cumulus clouds (Kogan et al., 2012; Werner et al., 2013). For cloud class 2 and 3 only 15% and 10% of all data were affected by the cloud step filter. Statistics were slightly shifted toward larger values. All cloud statistics are summarized in Table 6.4 separated into cloud classes.

6.2 Cirrus Clouds

During the three *Polarstern* cruises only 12 cirrus cloud cases were observed, see Table 6.5. It contains the position, time period and the cloud base height obtained from ceilometer or lidar data. Exemplary photos from the full-sky imager for each case are presented in Figure 6.10. The relatively low number of data points ($N_{\text{ci}} = 4010$) compared to observations of liquid water clouds, is caused due to the limitation of the applicability of the multi-wavelength cloud retrieval with regard to multi-layer clouds. Often the retrieval cannot be applied to cirrus because of the presence of underlying low-level boundary layer clouds. But as there is currently only one study which reports retrievals of cirrus microphysical properties from

ground-based spectral radiation measurements (LeBlanc et al., 2014), this work gives for the first time the opportunity to investigate different cirrus clouds at different locations over the ocean using ground-based radiation measurements. This could be the basis to compare them to satellite observations over the ocean and could help to understand the differences between both methods.

Classifying cirrus into cloud classes is not meaningful because as Figure 6.10 illustrates, cirrus is always inhomogeneous. Thus, all cirrus cases are shown in a meridional cross section from 50°S - 50°N in Figure 6.11. The latitude binsize is 5°. Although the number of data points per latitude bin (c) is too small to infer any meridional characteristics, it shows the large variability in retrieved microphysical properties. Largest fluctuations occur for τ ranging from nearly subvisible cirrus with averages of 0.2 to optically thick cirrus with $\tau = 6.0$ on average.

The frequency distribution of retrieved τ and r_{eff} from 12 cirrus clouds is presented in Fig-

Table 6.5: Overview on analyzed cirrus clouds during all cruises.

Case	Date	Latitude (°)	Longitude (°)	Time period (UTC)	Cloud base height (km)
1	May 2, 2011	3.945	-13.097	15.93 - 17.16	8.5
2	May 12, 2011	34.974	-11.244	11.61 - 16.12	9.0
3	Apr 12, 2012	-48.419	-62.597	16.10 - 16.32	6.0
4	Apr 14, 2012	-42.759	-55.125	12.96 - 18.53	6.0-10.0
5	Apr 17, 2012	-34.436	-43.246	18.34 - 20.35	9.0-10.0
6	Apr 20, 2012	24.540	-37.851	13.28 - 17.52	8.0-9.0
7	May 4, 2012	24.212	-37.851	18.34 - 18.36	9.0-11.0
8	May 7, 2012	33.153	-13.660	11.0 - 12.26	12.0
9	May 9, 2012	38.514	-12.649	12.27 - 13.16	9.0
10	Oct 31, 2012	41.410	-10.733	9.98 - 12.53	9.0
11	Nov 2, 2012	34.833	-13.133	16.86 - 19.91	8.0-10.0
12	Nov 10, 2012	11.555	-20.062	16.85 - 18.82	8.0-10.0

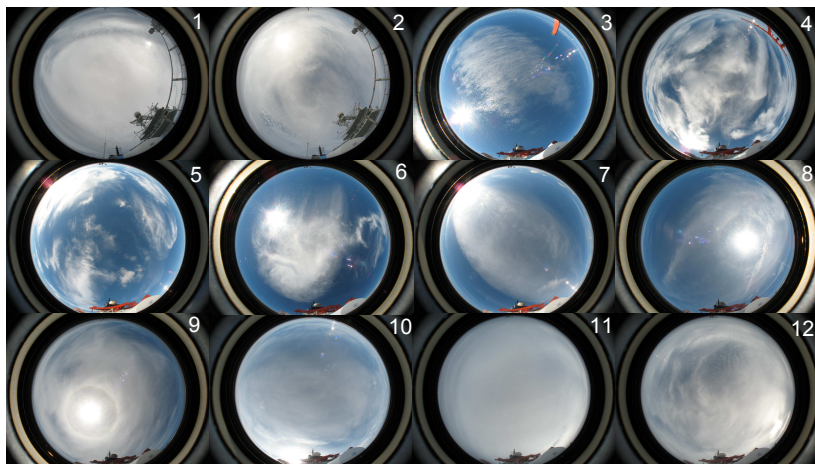


Figure 6.10: Photos of typical cloud situation for numbered cirrus cases from full-sky imager.

ure 6.12. The binsize for τ and r_{eff} is 0.5 and $2\ \mu\text{m}$, respectively. Additionally, the five–number summary is given for the respective distribution. As discussed in Section 6.1.3, the range of the distribution is 0.1 – 10.0 for τ , and 0.0 – $60.0\ \mu\text{m}$ for r_{eff} . It represents the retrieval limit for ice clouds. The τ distribution shows largest frequency of occurrence for $\tau \leq 1$ but also has a second maximum around 5. This is probably only a random event caused by the low number of data points rather than a characteristic optical thickness for cirrus. The median of the distribution is 1.2. The respective *IQR* and *PR* is 3.5 and 6.0, respectively. The distribution of r_{eff} is more normal distributed. Comparable to the liquid water cloud results, also an increased number of $r_{\text{eff}} \leq 2\ \mu\text{m}$ reveals. One possible reason could be the increased number of observations at high solar zenith angles. In 7 of 12 cases, θ_0 was larger than 70° . The signal–to–noise ratio increases, especially in the NIR wavelength region where transmissivity is sensitive to r_{eff} . When the cirrus is optically thin, which occurs often, then the retrieval for r_{eff} is not successful, which in turn has influence on the median of the distribution. The median is $12.2\ \mu\text{m}$, that is rather small for ice crystals. The *IQR* is $16.7\ \mu\text{m}$ and *PR* is $28.0\ \mu\text{m}$. Meaning only 20% of all r_{eff} retrievals were larger than $28.0\ \mu\text{m}$. It also should be kept in mind, that the ice crystal parametrization by Baum et al. (2007) was used in the radiative transfer model due to the lack of information on the ice crystal shape. The pictures in Figure 6.10 illustrate visually that there are distinct differences between all cirrus cases, resulting from differences of microphysical properties as ice crystal shape or particle diameter or ice water content. Further investigations including in situ data are required to understand the influence of those parameters on the retrieval of cirrus from ground–based radiation measurements.

6.3 Comparison with Satellite Measurements

For the first time ground–based measurements along transatlantic cross sections over the ocean were used to retrieve cloud properties. That provides the unique opportunity to com–

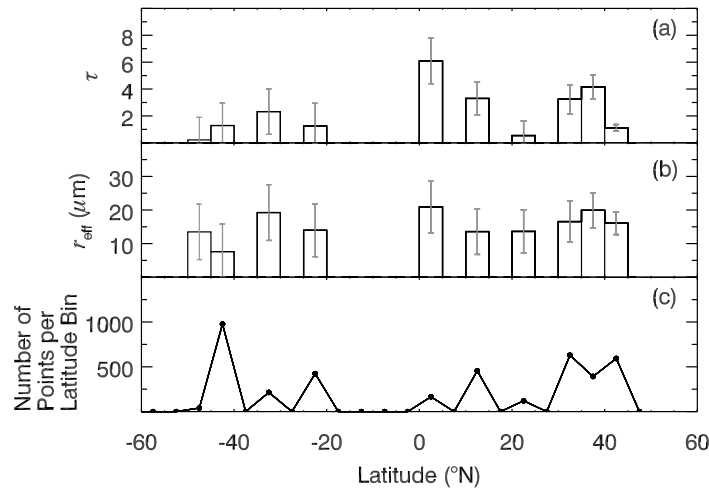


Figure 6.11: Meridional 5° –latitude–averages of retrieved (a) τ , (b) r_{eff} , and (c) number of retrieval points per latitude bin from 50°S - 50°N from all RV *Polarstern* cruises. Data points include all cirrus clouds.

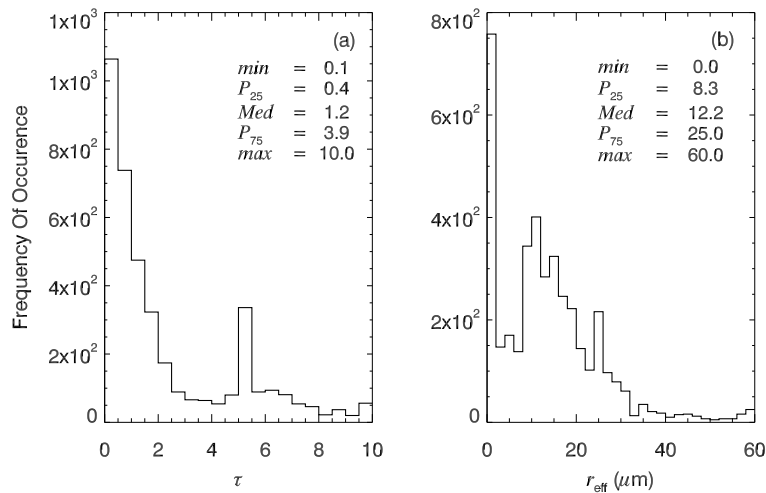


Figure 6.12: Histograms of retrieved (a) τ with binsize of 0.5, (b) r_{eff} in units of μm with binsize of $2 \mu\text{m}$, containing all cirrus clouds from all *Polarstern* cruises. Numbers indicates minimum, first quartile, median, third quartile, and maximum value of the respective distribution.

pare and complement satellite-based cloud retrievals over the ocean in different climate zones. So far there are only a few papers focusing on ship-based cloud retrievals (McBride et al., 2011, 2012), but these are limited to case studies only. Currently, there are no cloud retrievals from buoy measurements available. This work provides a first approach to investigate and understand the differences from ground-based and satellite-based cloud property retrievals over the ocean. The CORAS retrievals were compared to satellite data obtained from the Moderate Resolution Imaging Spectroradiometer (MODIS) on Terra and Aqua. MODIS is a 36-band scanning spectroradiometer, while 4 spectral bands (858 nm, 1640 nm, 2130 nm, and 3750 nm) are used in a daytime solar cloud retrieval algorithm over ocean (King et al., 1997, 2006). Other spectral bands in the terrestrial spectral region are used to obtain cloud cover and cloud top properties (e.g., thermodynamic phase). The instrument is designed to scan in the nadir direction in a plane perpendicular to the velocity of the spacecraft. Further technical details can be found in King et al. (1997). MODIS retrievals of τ and r_{eff} are based on plane-parallel radiative transfer calculations using the definition for spectral reflectivity function given in Chapter 2. The current MODIS algorithm (Platnick et al., 2003) is an updated version of the classic Nakajima and King (1990) 2-WL-method. MODIS data are provided on different websites. The MODIS Level-2 and Level-3 data were taken from <http://ladsweb.nascom.nasa.gov/index.html> provided by NASA Goddard Space Flight Center.

First, the MODIS collection 5.1 Level-2 cloud product (MYD06_L2) data were used to compare the retrieval results for each measurement day of ANT-XXIX/1. Therefore, the MODIS pixel have to be selected according to the geographic position of the ship. In a first step, the latitudes and longitudes from MODIS were interpolated from the 5×5 km resolution to a 1×1 km pixel resolution. To adjust the satellite data to the measured time series of liquid water clouds, the mean values of ship latitude and longitude and the absolute values between the difference of minimum and maximum latitude/longitude of the respective time periods were used to define the corresponding MODIS pixels for each day. The geographic section

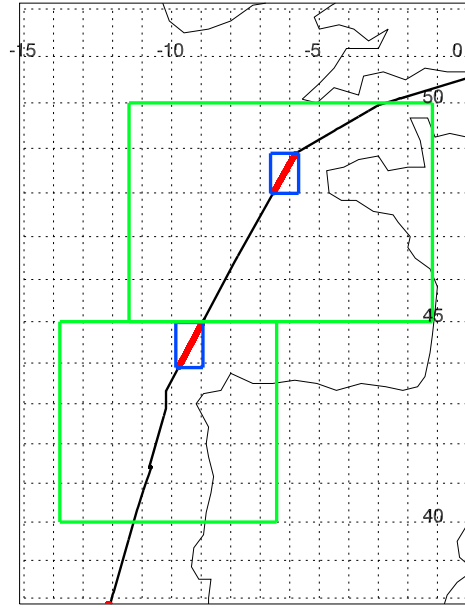


Figure 6.13: Geographical section between 38°N and 52°N, and 0°E and 15°W for illustration of satellite data preparation from MODIS. Black solid line is the cruise track from RV *Polarstern* with red plotted segments representing measurements of CORAS from liquid water clouds. Two different data preparation versions are shown. Blue square illustrates the geographic coordinates of 1 × 1 km resolution MODIS Level-2 cloud product, which is adjusted to the cruise track for each measurement day. Green square illustrates the geographic coordinates of 1 × 1 km resolution monthly global MODIS Level-3 cloud product adjusted to cruise track in 5°-latitude bins.

is illustrated in Figure 6.13 with a blue box around the CORAS measurements for a short cruise track excerpt. Usually, this results in one (or two) satellite overpass depending on the measured time period. Additional to τ and r_{eff} data, the multi-layer and cirrus flag was used to identify single-layer or cirrus clouds. The satellite derived LWP was calculated using Eq. (5.2) to be comparable to CORAS LWP retrievals. Furthermore, Seethala and Horvath (2010) found that an overall MODIS high bias in overcast cloud scenes could be removed using the adiabatic correction in a global mean sense.

The meridional cross section of 5°-latitude averages of τ , r_{eff} and LWP is shown in Figure 6.14 for ANT-XXIX/1. Black and blue colored bars refer to ship-based CORAS and HATPRO retrievals, respectively, while red colored bars represents MODIS retrievals with respective standard deviations. The meridional cross sections of the other two cruise legs can be found in the Appendix A. As discussed in Section 6.1.1, the CORAS retrievals show a distinct meridional distribution. With regard to τ , the satellite retrievals reveals a good agreement with CORAS data for averages of $\tau \leq 10$. Largest similarities occur for liquid water clouds in the subtropics. Whereas it seems to be that there is a bias toward smaller values of τ from MODIS for thicker clouds ($\tau > 10$). This is pronounced in the mid-latitudes and tropics. Although MODIS has a relatively high spatial resolution of 1 × 1 km in reflected radiances, the collocation with CORAS and the ship track may sometimes not coincide. As the blue box in Figure 6.13 illustrates, the MODIS retrievals are an average over a wider area than the ship-based retrievals. However, CORAS retrievals under thick clouds are associated with larger uncertainties which results in a lower number of valid retrievals. τ is

overestimated which might cause those deviations under thick clouds. Such large deviations in averaged values are not determined for the r_{eff} retrievals since both r_{eff} averages lie within the respective standard deviations. On the contrary, there seems to be a bias in MODIS r_{eff} toward larger averages. MODIS r_{eff} retrievals are 20% – 70% larger than those obtained from CORAS. Platnick (2000) modeled photon multiple scattering through cloud layers for different wavelengths in the NIR region which are used in the MODIS algorithm to retrieve r_{eff} . Using vertical profiles of r_{eff} , he calculated reflectivity weighting functions through the cloud and showed significant differences among these wavelengths. While the weighting at $1.6\ \mu\text{m}$ spreads more evenly into the lower portion of the cloud, the weighting at $3.7\ \mu\text{m}$ is confined to the near cloud top with larger cloud droplets, whereas transmissivity showed a more symmetric weighting throughout the center and bottom layer of the cloud associated with smaller droplets. Retrievals from satellite-based measurements of cloud reflectivity are mostly determined from the upper cloud layers (Platnick et al., 2003). As it was discussed in Section 5.1.3, 3D radiative effects can arise from resolved and unresolved cloud structure variability. The latter is known as the subpixel cloudiness (Platnick et al., 2003; Marshak et al., 2006). Clear regions on a subpixel scale reduce the reflectivity of what is assumed to be an overcast pixel. The retrieved r_{eff} is overestimated while τ is underestimated. Resolved or neighboring pixel variability cause an increase in the domain averaged retrievals of τ and r_{eff} compared to their 1D counterparts (Marshak et al., 2006). The comparison of averaged *LWP* retrievals (Figure 6.14c) from CORAS, MODIS and HATPRO generally shows a good agreement within the standard deviations. While the retrievals based on radiation measurements are restricted to the analyzed time periods, averages of HATPRO *LWP* includes also non-precipitating liquid water clouds during night. As already mentioned, the CORAS *LWP* shows an overestimation of *LWP* under thick clouds.

To investigate the above mentioned differences in τ and r_{eff} retrievals from CORAS and MODIS, Figure 6.15 presents the distributions of retrieved τ (left panels) and r_{eff} (right panels) from both instruments for all single-layer clouds. Both τ distributions have similar medians with 6.6 for CORAS and 7.9 for MODIS. The influence of smaller values of τ was already discussed. Comparing the distributions of r_{eff} , reveals a difference between both methods. The CORAS distribution is shifted toward smaller values of r_{eff} (reasons have been discussed) but shows a wider range of distributed r_{eff} . The median is $7.7\ \mu\text{m}$. The MODIS retrievals are more normal distributed and narrow. The median of MODIS r_{eff} distribution is $11.9\ \mu\text{m}$. Even with consideration of 3D radiative effects on CORAS r_{eff} retrievals (cloud step filter), the median indeed increases to $9.9\ \mu\text{m}$, but the shape of the distribution is still significantly different compared to the satellite results reflecting the different perspectives of retrieval methods based on reflectivity or transmissivity.

To summarize, the meridional distribution of cloud properties obtained from ship-based CORAS measurements can be confirmed with satellite observations from MODIS for each day with respect to τ . Limitations holds true for thick clouds. With regard to r_{eff} distributions both methods reveal a similar meridional distribution. However, the r_{eff} obtained from satellite are generally biased toward larger values of r_{eff} compared to the ground-based observations. To understand and quantify those differences between satellite- and ground-based cloud retrievals further investigations are needed. Especially the influence of cloud

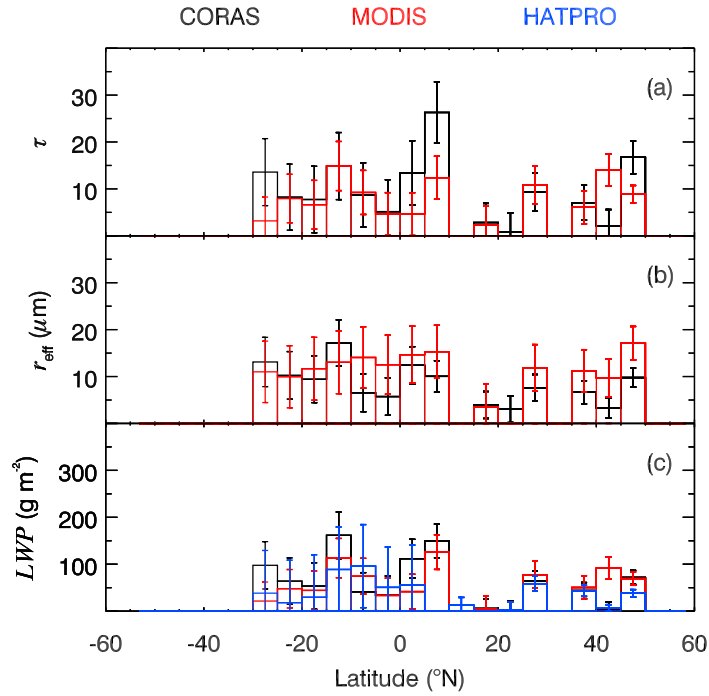


Figure 6.14: Meridional 5° -latitude-averages of retrieved (a) τ , (b) r_{eff} , and (c) LWP from 30°S - 50°N from ANT-XXIX/1. Black and blue colored bars represents retrieval results from CORAS and HATPRO, respectively, along the ship track. Red colored bars includes MODIS Level-2 cloud product retrievals adjusted to cruise track. Data points include all single-layer non-precipitating liquid water clouds.

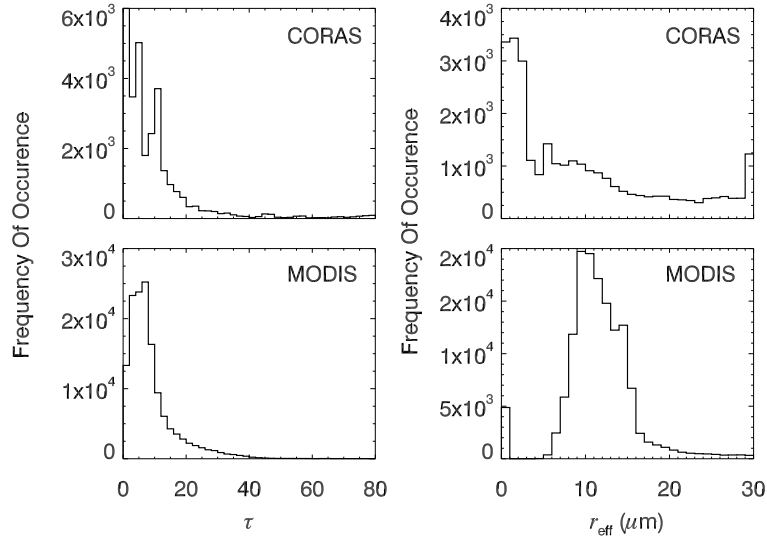


Figure 6.15: Histograms of retrieved τ from CORAS and MODIS with binsize of 2 (left panels), and r_{eff} in units of μm from CORAS and MODIS with binsize of $1\mu\text{m}$ (right panels), containing all liquid water clouds from ANT-XXIX/1.

vertical stratification on r_{eff} retrievals of both methods should be studied in more detail.

In a second approach, it was verified whether the meridional distribution observed during the transect between October/November 2012 is representative of climatological distinctive

cloud properties. Therefore, the monthly MODIS collection 5.1 Level-3 cloud product data from Terra and Aqua (MOD08_M3.051, MYD08_M3.051) were used to create a climatology of τ , r_{eff} and LWP from October/November in 2008–2012 of liquid water clouds. According to the previous approach, a 5° -latitude bin was used. To consider a larger longitudinal area than that restricted to the cruise track, MODIS data were selected by using the longitudes $\pm 2.5^\circ$ at the respective latitude coordinates. This is illustrated in Figure 6.13 with green boxes. Thereby, the amount of land surfaces should preferably be low, but in fact cannot be ruled out completely.

The climatology from 30°S - 50°N is presented in Figure 6.16. Although the differences in latitude averages are smaller compared to those shown in Figure 6.14, a meridional distribution in τ is noticeable. The northern mid-latitudes are dominated by autumn storm tracks with maximum τ averages. The subtropics are characterized by lowest τ averages, whereas it is more pronounced in the northern than in the southern subtropics. Due to the influence of dry Sahara air between 10°N - 15°N τ reaches minimum averages. The southern subtropics exhibit larger averages due to the increased frequency of stratocumulus clouds in front of the west coast of Africa. The same was observed for cruise leg ANT-XXIX/1. However, the tropics are characterized in the climatology by relative moderate averages of τ . This underlines the variable character of tropical convective systems. Furthermore, the influence of multi-layer clouds or overlying ice clouds on the MODIS τ (r_{eff}) retrievals is strengthened which might cause lower averages than those observed during one day cross section through the ITCZ. But in general, the observed meridional τ distribution during ANT-XXIX/1 is reflected in the 5-year climatology from October/November observed from MODIS. However, the climatological r_{eff} distribution is more smoothed. Increased r_{eff} averages are obvious in the tropics and northern subtropics contrary to the observations from the ship. But as there are currently largest discrepancies between r_{eff} retrievals from the ground and from satellite, this issue certainly requires further investigations.

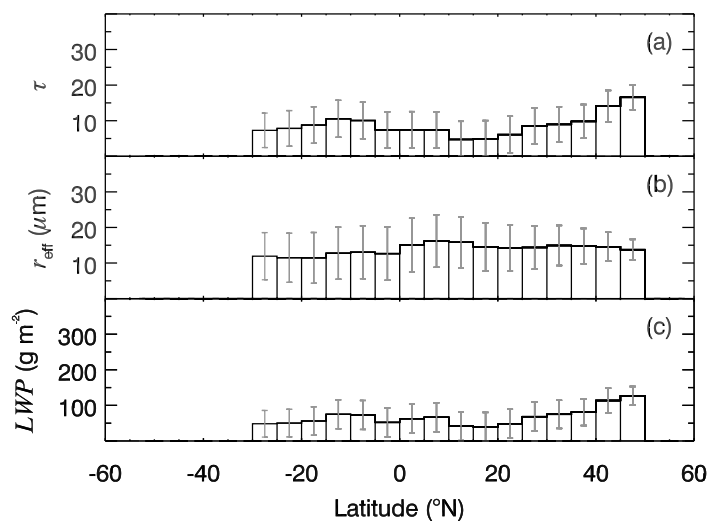


Figure 6.16: Meridional monthly means of 5° -latitude-averages of retrieved (a) τ , (b) r_{eff} , and (c) LWP from MODIS Level-3 cloud product from 30°S - 50°N for October/November 2008–2012. Data points include all single-layer non-precipitating liquid water clouds.

7 Summary, Conclusions and Outlook

Within this work the microphysical and optical properties of marine clouds have been investigated by radiative transfer simulations and respective ship-based measurements of spectral zenith radiances. The objective of this thesis is to develop a ground-based cloud retrieval to deduce optical (τ) and microphysical (r_{eff} , LWP) cloud properties which is suitable to characterize different types of liquid water and ice clouds over the ocean. Further, the retrievals are used to analyze the distribution of cloud properties regarding their specific and meridional characteristics. These two issues are summarized in the following sections. Finally, an outlook on further investigations is given.

7.1 Summary and Conclusions

Within the German Leibniz-network OCEANET-project, ship-based active and passive remote sensing measurements were performed during three transects of RV *Polarstern* over the Atlantic ocean. Latitudes between 50°N and 50°S were covered within 13 weeks. Spectral zenith radiances I_{λ}^{\downarrow} with a time resolution of 15 s were sampled by the COmpact RAdiation measurement System (CORAS). I_{λ}^{\downarrow} was measured in the spectral wavelength region between 350 – 2000 nm with two spectrometers covering the visible to near-infrared (VNIR) to short-wave infrared (SWIR) spectral region. The optical inlets for spectral irradiance and radiance were mounted on the roof of a measurement container and were connected via optical fibers to a spectrometer system. In this work, only the radiance measurements were used. The spectrometers were calibrated in the laboratory before and after each measurement campaign. To monitor the calibration stability of the system, a transfer calibration was performed if procurable each day on the ship.

The measurements were completed by several instruments measuring basic meteorological parameters (temperature, pressure, humidity, wind speed), broadband solar and terrestrial downward radiation, and a full-sky imager provided 180° -photographs of the upper hemisphere. A lidar provided vertical profiles of aerosol microphysical properties with a high temporal and spatial resolution. The microwave radiometer Humidity And Temperature PROfiler (HATPRO) supplied vertical profiles of temperature and humidity as well as profiles of liquid water path (LWP). The slow velocity of usually 10 kn (about 5 m s^{-1}) of the ship allows sufficient measurements with respect to temporal and spatial resolution to investigate cloud inhomogeneities.

7.1.1 Improved Multi-Wavelength Cloud Retrieval

The retrieval of optical thickness τ and droplet effective radius r_{eff} of clouds using observed and simulated spectral zenith radiances requires a different treatment of physical principles compared to the well-known reflectivity-based counterpart as performed by satellites and aircraft measurements. However, zenith radiances which can be converted to spectral transmissivity contains relatively less information on r_{eff} compared to reflectivity. Due to competing effects of cloud droplet absorption and forward scattering, the sensitivity to this parameter is reduced. Furthermore, transmissivity is not a unique function of τ , which causes retrieval ambiguities. Existing transmissivity-based cloud retrievals already achieved reasonable results for τ ranging from 10 to 40, however, large uncertainties remain for optically thin clouds with $\tau < 5$. Also the sensitivity to r_{eff} could be enhanced by using spectral features of asymmetry factor and spectral coalbedo within the NIR spectral wavelength region. Still the range of validity of these retrievals and associated uncertainties reveals a number of essential improvements.

To infer microphysical properties from spectral transmissivity measurements, simulated zenith radiances were calculated using a plane-parallel (1D) radiative transfer model. Thus, lookup tables of transmissivity were generated for a reasonable range of τ and r_{eff} . Single-scattering properties based on Mie theory were used for liquid water clouds, while a parametrization of ice single-scattering properties from Baum et al. (2005a, 2007) was applied.

In this work a new cloud retrieval using ratios of spectral cloud transmissivity is introduced. The six-wavelength approach uses the information of three ratios of spectral transmissivity (wavelength combinations: 450 nm/680 nm, 1050 nm/1250 nm, 1670 nm/1560 nm) to retrieve simultaneously cloud optical thickness and effective radius. The combination of these transmissivity ratios overcomes the limitations of existing retrievals concerning thin liquid water clouds ($\tau < 5$). Furthermore, the retrieval ambiguity with regard to τ is circumvented by separating very thin and thick clouds. Using ratios of transmissivity in certain wavelength regions, reduces the measurement uncertainties significantly compared to methods using absolute values. The multi-wavelength method benefits from the spectral features of zenith radiance depending on the scattering and absorption properties from liquid water droplets and ice crystals and thus is applicable to liquid water and ice clouds. The retrieval is fast and accurate and thus suitable for operational purposes and the huge variety of measurements obtained during three cruises. Compared to the slope method by McBride et al. (2011), the computational time was reduced by a factor of 15.

The spectral cloud retrieval was applied to observations on board of RV *Polarstern* during three Atlantic transfers of the OCEANET-project. Primarily, the new cloud retrieval was applied to homogenous, inhomogeneous, and scattered liquid water clouds, as well as to cirrus clouds.

For the presented case study of a homogenous liquid water cloud the mean τ and r_{eff} was calculated with 9.1 ± 0.5 and $16.1 \pm 1.7 \mu\text{m}$, respectively. The variability of r_{eff} is caused by complex mixing of thermal energy and water vapor from layers above and beneath the cloud. Larger variability in the r_{eff} retrieval occur for thicker clouds when zenith radiance is more attenuated. Considering an uncertainty threshold of ± 1 in τ and $\pm 2 \mu\text{m}$ in r_{eff} ,

the new multi-wavelength retrieval results in 87% and 78% valid retrievals for τ and r_{eff} , respectively. Measurement uncertainties increase for thicker clouds ($\tau > 40$) as the attenuation of spectral radiance is increased. For a number of measurements r_{eff} reaches values up to $30 \mu\text{m}$ which represents the upper retrieval limit. Possible reasons for cloud particles with $r_{\text{eff}} > 30 \mu\text{m}$ were discussed. In warm marine stratocumulus clouds a large number of drizzle droplets near the cloud base was found which can significantly increase r_{eff} and could explain these observations reported here. From the retrieved microphysical properties the *LWP* was calculated using an adiabatic approximation where r_{eff} increases above the cloud base height. The comparison with the *LWP* from microwave radiometer HATPRO shows an overestimation of the *LWP* by CORAS for clouds with $LWP > 80 \text{ g m}^{-2}$ and an underestimation for values of $LWP < 80 \text{ g m}^{-2}$. Due to the increased attenuation of spectral zenith radiance in optical thick clouds, the CORAS retrieval results are larger and associated with larger uncertainties. For the analyzed homogeneous cloud scene a mean *LWP* of $87 \pm 49 \text{ g m}^{-2}$ for HATPRO and $97 \pm 11 \text{ g m}^{-2}$ for CORAS was derived. Even for a complex inhomogeneous precipitating water cloud scene both instruments have shown comparable results for the *LWP*. That indicates that the transmissivity retrieval provides reasonable cloud properties.

Applying the multi-wavelength retrieval to scattered liquid water cloud scenes introduced a number of challenges. Particularly for fuzzy and fractal clouds in combination with an increased wind speed, the temporal resolution of the CORAS measurements (15 s) might be not sufficient to resolve those clouds. In particular, 3D radiative effects at cloud edges cause significantly increased values of retrieved r_{eff} , whereas τ is underestimated.

In addition to water clouds also cirrus clouds were investigated by the multi-wavelength approach. For the different cirrus cases, cloud inhomogeneities were observed with mean values of τ range from 0.2 – 2.3 with uncertainties ranging from ± 0.04 to ± 0.2 . While τ significantly changes within the cloud, observed r_{eff} are found to be more constant with mean values ranging from $4.9 \pm 0.8 \mu\text{m}$ to $19.7 \pm 1.9 \mu\text{m}$ for different cloud scenes. For cirrus with $\tau < 2.5$ a comparison with lidar observations of τ is possible, since those clouds are transparent for laser light. By calculating 5-minute averages of vertical extinction coefficient profiles obtained from Polly^{XT} Arielle, mean values and standard deviations of τ (at $\lambda = 532 \text{ nm}$) for a chosen time period are calculated with 1.03 ± 0.02 for CORAS and 0.88 ± 0.13 for lidar observations, respectively. Note, that results from the lidar are heavily sensitive to the assumption of the lidar ratio. Cirrus cloud inhomogeneities are better temporally resolved with the multi-wavelength cloud retrieval.

A comparison between the new multi-wavelength cloud retrieval and the slope method (McBride et al., 2011) yields similar results for τ and r_{eff} , while the mean temporal deviation for τ was smaller (2.5) than for r_{eff} ($4.4 \mu\text{m}$). Both methods exhibit good agreement with the HATPRO *LWP* retrieval. Propagating the measurement uncertainties through both approaches, it was found that the multi-wavelength retrieval slightly reduces the uncertainties with regard to τ (slope method: 78%, multi-wavelength method: 82%) considering an uncertainty threshold of ± 1 , and significantly reduce the r_{eff} uncertainties. 80% of the retrievals passes the uncertainty threshold ($\pm 2 \mu\text{m}$), whereas only 66% valid retrievals were obtained with the slope method. In conclusion, the new multi-wavelength retrieval yields comparable

values of τ and r_{eff} with regard to the existing slope method, but reduces the retrieval uncertainties by using ratios instead of absolute values. In conjunction with the notable reduction of the computational time, this method is more suitable for the observations on the ship and more adjustable to different cloud scenes, in particular for clouds with $\tau < 5$.

7.1.2 Distributions of Cloud Properties

In the second part of this thesis, the meridional distribution of the retrieved cloud properties (τ , r_{eff} , and LWP) obtained during three transatlantic cruises with *Polarstern* were investigated. The statistical analysis was limited to either all non-precipitating single-layer liquid water clouds or to cirrus. First, liquid water clouds governed by local weather systems were investigated to find certain main characteristics of their properties in different climate zones. It was found that the west wind zone in the mid-latitudes (30°N/S - 50°N/S) is dominated by storm tracks, associated with larger cloud droplets and denser clouds. The subtropics around the equator reveals a conspicuous minimum of 5°-latitude averaged values of τ and r_{eff} . Prevailing trade winds formed typical trade wind cumuli. Especially, between 10°N - 15°N cloud properties achieved minimum averages of $\tau = 1.7$, $r_{\text{eff}} = 4.1 \mu\text{m}$, and $LWP = 10 \text{ g m}^{-2}$, as the influence of dry Sahara air causes mainly fair weather conditions. Same results were found for meridional distribution of HATPRO LWP observations during 8 *Polarstern* cruises (Zoll, 2012). The southern subtropics are affected by the increased frequency of stratocumulus clouds formed over the colder ocean in front of the west coast of Africa. This is consistent with global observations. Here, moderate averages of τ , r_{eff} and LWP with $\tau = 9.8$, $r_{\text{eff}} = 10.3 \mu\text{m}$, and $LWP = 67 \text{ g m}^{-2}$ were found. In the tropics cloud properties are mainly influenced by convective clouds in the ITCZ. But as the multi-wavelength cloud retrieval is limited to non-precipitating single-layer clouds, many data points have to be excluded from the analysis. In the end, similar characteristics of cloud properties can be found in the mid-latitudes and northern subtropics for all three cruises, but the large variability of meridional distribution in the remaining regions imply that the influence of weather systems prevails compared to typical cloud distributions. This work gives a first starting point for those investigations, but certainly a larger number of transatlantic cruises are required.

Nevertheless, main characteristics of cloud properties for certain liquid water cloud types are obvious. Therefore, a cloud type classification was performed to separate homogeneous, inhomogeneous and scattered liquid water clouds. From altogether 60692 cloud data points, the cloud class 2 including homogeneous stratocumulus was found to be the prevailing cloud type over the ocean with about 63%; followed by cloud class 1 (scattered cumulus) and cloud class 3 (inhomogeneous stratus or cumulus) with an occurrence of 16% and 21%, respectively. Clear sky, summarized in cloud class 0, amounts to 43% of all analyzed 105963 data, while each cloud class contributes to this percentage. The two almost identical cruise legs between Cape Town and Bremerhaven in spring and autumn, exhibit no seasonal differences in cloud classification. About one third of all observed data from three cruises were excluded. In detail this comprises mixed-phase or multi-layer clouds, as well as longer time periods of clear sky observations.

Based on the cloud classification of liquid water clouds, descriptive statistics of retrieved cloud properties were calculated for unfiltered and cloud step filtered data separately. For the unfiltered distributions, medians of τ , r_{eff} and LWP were calculated with 6.6, 7.7 μm , and 29.2 g m^{-2} , respectively. The individual cloud class distributions reveal differences. Cloud class 1 distributions are characterized by small values of descriptive statistic (1.6, 2.5 μm , 1.7 g m^{-2}). A wider range of retrieved τ and r_{eff} is found for cloud class 2 (7.3, 8.7 μm , 35.0 g m^{-2}). As expected, cloud class 3 reveals the broadest distribution of cloud properties (10.0, 12.0 μm , 81.9 g m^{-2}). However, it has become apparent that all distributions were affected by an increased frequency of small values of retrieved cloud properties. This was probably caused by 3D radiative effects, especially around cloud edges which cannot be sufficiently resolved and covered by 1D retrievals. Therefore, the adequate analysis was performed with cloud step filtered data to account for these effects. The sum of two sequenced retrieved values of τ have to be greater or equal 4. As a result, retrievals at cloud edges with increased uncertainty due to 3D radiative effects were almost sorted out. The threshold of $\tau \geq 4$ is found to be the most suitable to provide a sufficient number of remaining data and reduce the bias toward smaller values. Applying the cloud step filter to the distributions results in medians of τ , r_{eff} and LWP of 9.5, 9.9 μm , and 52.8 g m^{-2} , respectively. With almost 48% cloud class 1 is mostly affected by cloud edge observations, nevertheless, medians of cloud property distributions were corrected by filtering toward more realistic values for scattered cumulus clouds found in the literature (5.0, 3.0 μm , 10.3 g m^{-2}).

With only 12 analyzed cirrus cloud cases during all transects, a representative statement about the meridional distribution of cirrus cloud properties cannot be made. Since there is currently only one other study which investigates cirrus microphysical cloud properties from ground-based spectral radiation measurements over land, this work introduces a remarkable data set of retrieved cirrus properties based on ship measurements over the ocean for the first time. The median of cirrus τ and r_{eff} distributions is 1.2 and 12.2 μm , respectively.

Using the huge amount of ship-based cloud retrievals in different climate zones provides the unique opportunity to compare them to satellite-based cloud retrievals over the ocean. Recently studies focus only on single case studies. This work introduce a first approach to investigate differences in ship-based and satellite-based cloud retrievals. Retrieval data of τ , r_{eff} and LWP from the Moderate Resolution Imaging Spectroradiometer (MODIS) are compared to CORAS results. In a first approach, the MODIS retrievals were adjusted to the cruise track and observed time series of liquid water clouds from CORAS for each day of one measurement campaign. It was found, with respect to the meridional distribution, that MODIS retrievals show a good agreement with CORAS data of 5°-latitude averages for $\tau \leq 10$, while largest correlations were found in the subtropics. Smaller retrieved values of τ from MODIS are found for clouds with averages of $\tau > 10$. However, the MODIS r_{eff} retrievals are biased toward larger averages by differences of 20 – 70% compared to the ship-based observations. Applying also an adiabatic approximation for the LWP retrieval of MODIS has shown good agreement with the two ship-based LWP data sets from CORAS and HATPRO. Just for optical thick clouds with mean averages of $\tau > 10$ CORAS seems to overestimate the LWP . Differences of r_{eff} distributions between CORAS and MODIS retrievals were found. While MODIS r_{eff} values are normal distributed, CORAS r_{eff} distribution is shifted toward

smaller values and shows a wider range of r_{eff} . However, the information on r_{eff} comes from different layers inside the cloud (Platnick, 2000). As MODIS measures the reflectivity of the upper cloud layers, especially for optical thick clouds, the r_{eff} retrieval is shifted toward larger cloud droplets. Whereas the transmissivity-based CORAS retrievals of r_{eff} are determined by the center and the bottom layer of the cloud with smaller cloud droplets. Moreover, the merging of both r_{eff} retrievals could provide information on the vertical cloud structure. MODIS is sensitive to the upper cloud region, while CORAS is more sensitive to cloud droplets in the center and bottom of the cloud. From this analysis it can be concluded, that the meridional distribution of cloud properties obtained from the ship and space along a single cruise track show comparable averages of τ with limitations for optical thick clouds. Meridional r_{eff} distributions agreed within the uncertainties, however, the satellite generally retrieves larger values of r_{eff} compared to the ground-based retrieval.

In a second approach the climatology of monthly means of MODIS cloud retrievals from October/November in 2008-2012 were analyzed to evaluate the meridional distribution observed during an autumn cruise leg. With regard to the meridional τ distribution, same characteristic features observed during one transect are reflected in the 5-year climatology obtained from MODIS. Largest discrepancies were found for the climatological distribution of r_{eff} which is smoother for the MODIS data.

7.2 Outlook

In this work a new multi-wavelength cloud retrieval using ship-based spectral transmissivity measurements was presented and applied to a multitude of cloud types. It is planned to improve this retrieval, especially with regard to the vertical variation of the r_{eff} profile in the cloud. By using zenith radiance weighting functions, the influence of the vertical distribution of optical and microphysical cloud properties such as volumetric extinction coefficient and r_{eff} on zenith radiance will be investigated. Furthermore, the comparison with in situ microphysical measurements of droplet number concentration and r_{eff} obtained from aircraft measurements could help to verify the results presented here. For that purpose, a future campaign Arctic Amplification: Climate Relevant Atmospheric and Surface Processes and Feedback Mechanisms AC³ in the scope of the German Transregio-project, is planned in 2017, where spectral radiation measurements on RV *Polarstern* will be complemented with airborne measurements of spectral reflectivity performed on the research aircraft Polar 5 and Polar 6 operated by the Alfred-Wegener-Institute (AWI) Bremerhaven. For scattered clouds the plane-parallel (1D) approximation in the radiative transfer model is not applicable. To investigate and quantify 3D radiative effects on ground-based cloud retrievals, comparisons with 3D radiative transfer models are required. Furthermore, the influence of different ice crystal shapes on the retrieval is still under investigation and needs thorough quantification. Sensitivity studies with respect to ice habits have shown a broad range of τ and r_{eff} indicating a strong dependence of retrieved microphysical parameters on assumed ice crystal habit (e.g., McFarlane et al., 2005; Eichler et al., 2009). For that purpose, a campaign in Melpitz, Germany is planned in 2015, where the introduced multi-wavelength retrieval method will be applied to measurements provided by

two imaging spectrometers aisaEAGLE and aisaHAWK in the VIS and NIR wavelength region (<http://www.specim.fi/index.php/products/airborne>). These instruments provide high spectral, spatial and temporal resolved fields of radiance as a function of scattering angle, which can be used to give an estimate on the ice crystal shape. For the case studies presented here, the retrieval was either limited to liquid water or ice clouds in advance by independent observations. However, as shown by e.g., Pilewskie and Twomey (1987); Ehrlich et al. (2008b); Jäkel et al. (2013) spectral measurements can be used to retrieve the thermodynamic cloud phase. Adapting such methods for zenith radiance or transmissivity would allow to develop a retrieval for cloud phase suited for continuous measurements in different climate zones such as those on RV *Polarstern*. Such methods could help to identify undetected cloud layers which cause problems in the cloud retrieval.

The cloud remote sensing in a range of climate zones with latitudinal and longitudinal transects of research vessels provides a unique opportunity to understand the different perspectives of satellite and ground-based observations of clouds over the ocean. The presented data set in this work could help to complement geostationary and polar-orbiting satellite data. With respect to conclusions concerning climatological cloud property distributions, the amount of three transatlantic cruises is certainly insufficient. Beside the results from the comparison of cloud retrievals obtained from MODIS satellite and CORAS introduced in this work, it is planned to extend this investigation using Level-2 cloud product data of the Satellite Application Facility on Climate Monitoring (CM SAF) from the Spinning Enhanced Visible and InfraRed Imager (SEVIRI) along the cruise tracks of *Polarstern*. In a similar vein, it would be highly beneficial to use the CORAS retrievals for deriving surface energy budget terms, and compare those to estimates from the Clouds and the Earth's Radiant Energy System (CERES) on Terra/Aqua satellite, which has not been sufficiently validated with buoy measurements. As a result, especially the surface estimates over ocean are currently highly uncertain. Therefore, it would be beneficial to achieve a closure between the transmissivity-derived cloud properties and the associated spectral downward and broadband irradiances.

A Meridional Distributions of Cloud Properties

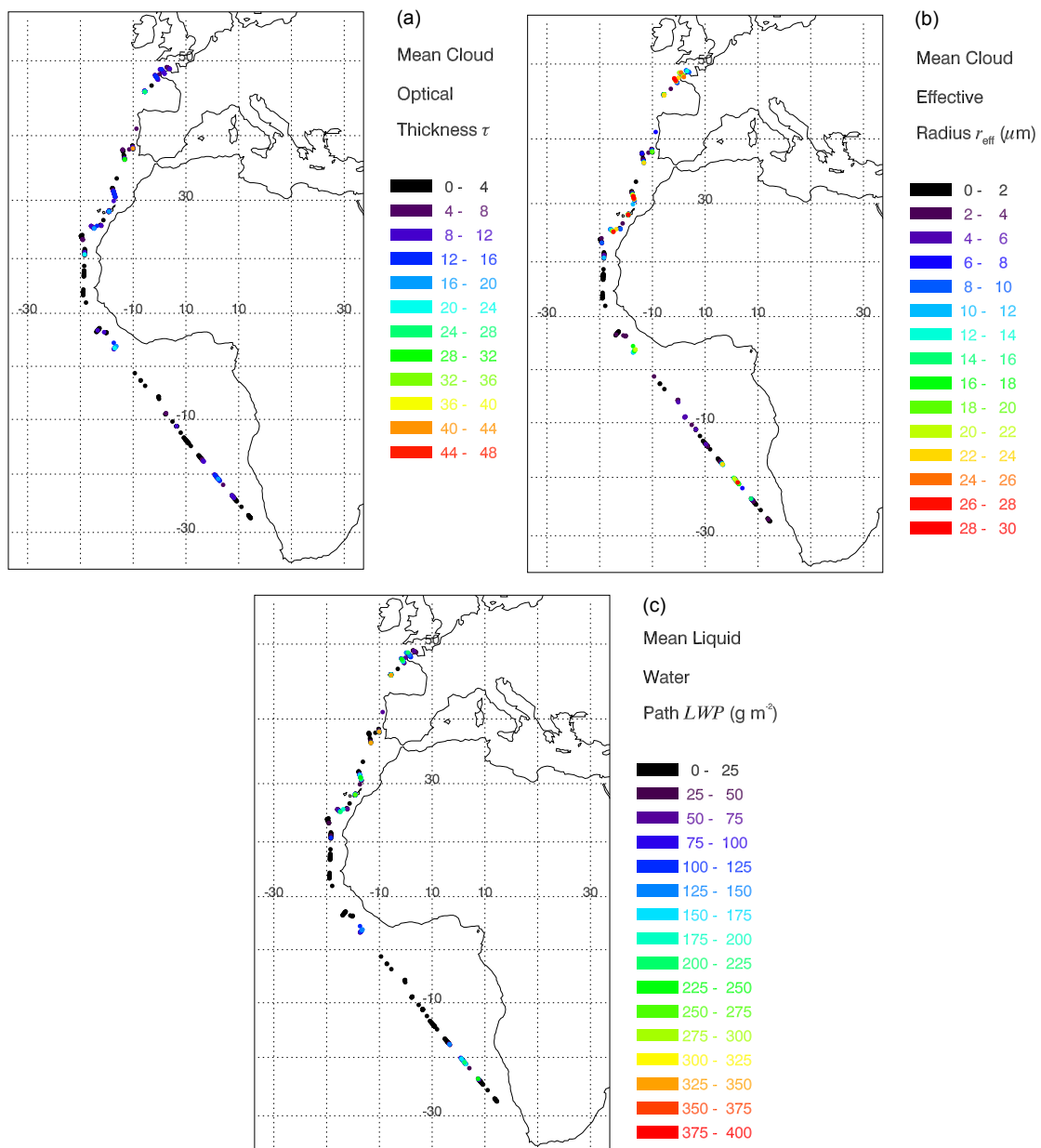


Figure A.1: 5-minutes-averages of retrieved (a) τ , (b) r_{eff} , and (c) LWP along the ship track from ANT-XXVII/4. Data points include all liquid water clouds.

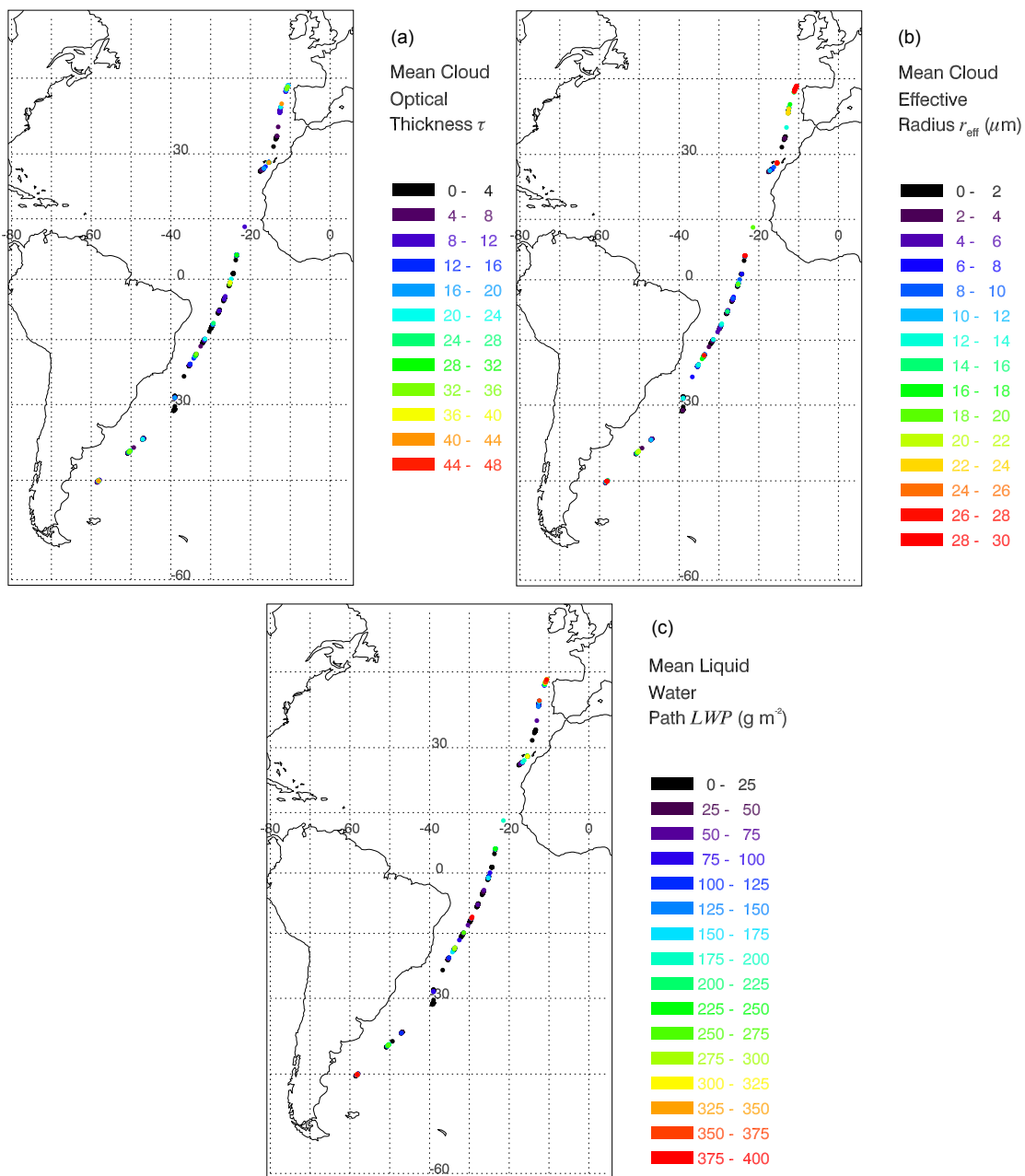


Figure A.2: 5-minutes-averages of retrieved (a) τ , (b) r_{eff} , and (c) LWP along the ship track from ANT-XXVIII/5. Data points include all liquid water clouds.

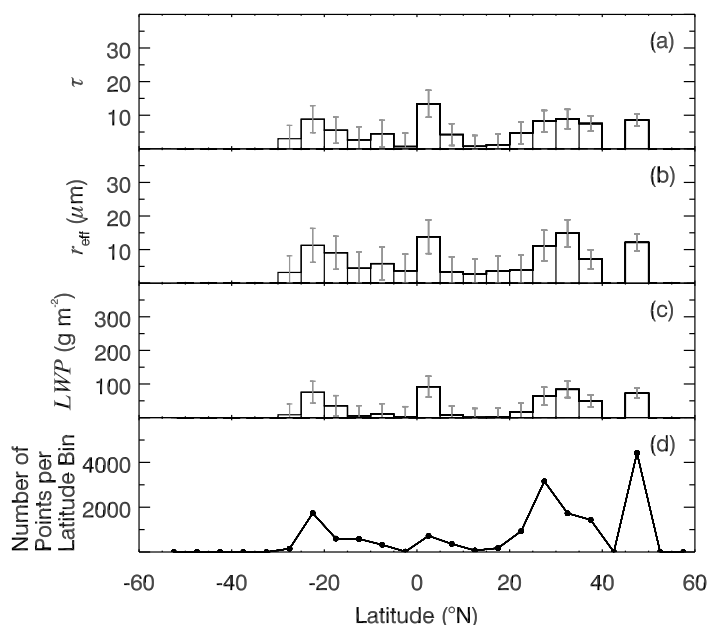


Figure A.3: Meridional 5° -latitude-averages of retrieved (a) τ , (b) r_{eff} , and (c) LWP , and (d) number of retrieval points per latitude bin from 40°S - 50°N from ANT-XXVII/4. Data points include all liquid water clouds.

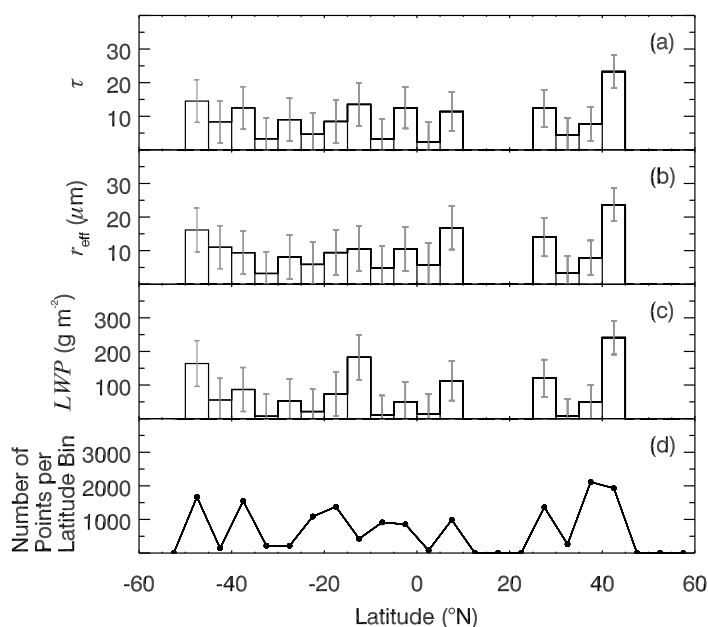


Figure A.4: Meridional 5° -latitude-averages of retrieved (a) τ , (b) r_{eff} , and (c) LWP , and (d) number of retrieval points per latitude bin from 40°S - 50°N from ANT-XXVIII/5. Data points include all liquid water clouds.

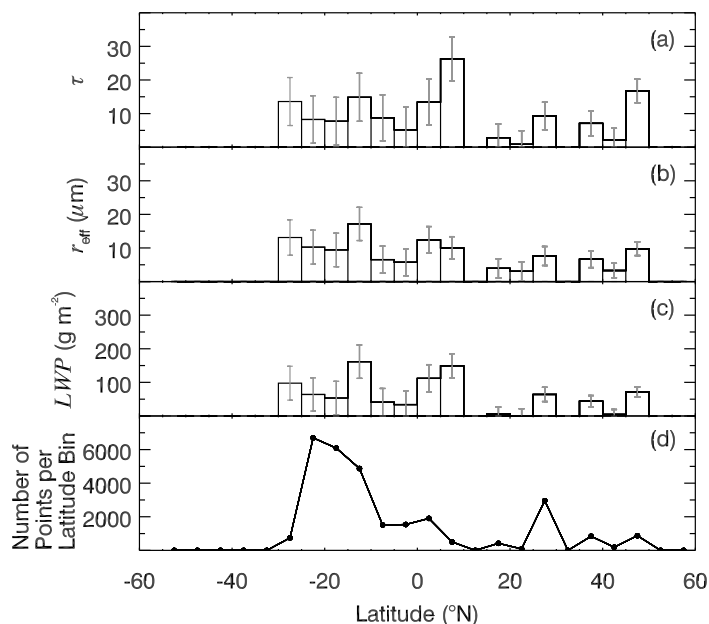


Figure A.5: Meridional 5°-latitude-averages of retrieved (a) τ , (b) r_{eff} , and (c) LWP , and (d) number of retrieval points per latitude bin from 40°S - 50°N from ANT-XXIX/1. Data points include all liquid water clouds.

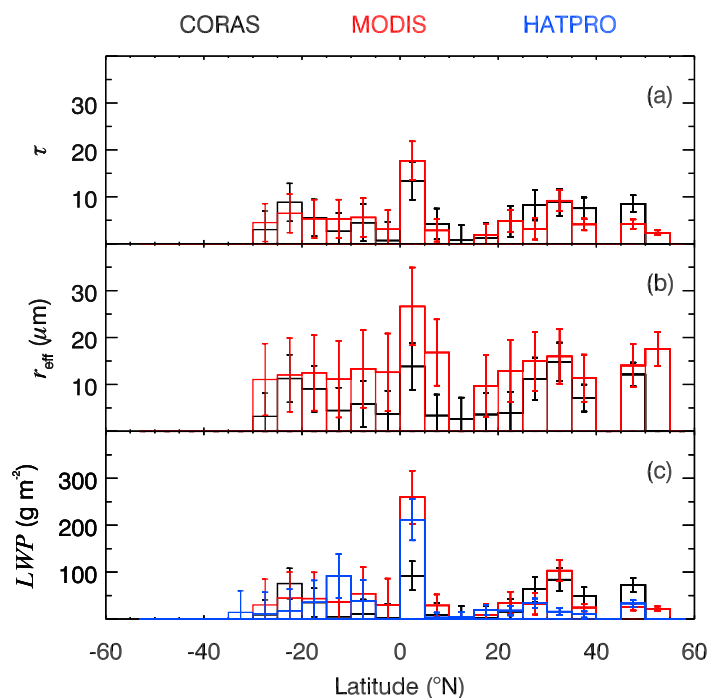


Figure A.6: Meridional 5°-latitude-averages of retrieved (a) τ , (b) r_{eff} , and (c) LWP from 50°S - 50°N from ANT-XXVII/4. Black and blue colored bars represents retrieval results from CORAS and HATPRO, respectively, along the ship track. Red colored bars includes MODIS Level-2 cloud product retrievals adjusted to cruise track. Data points include all single-layer non-precipitating liquid water clouds.

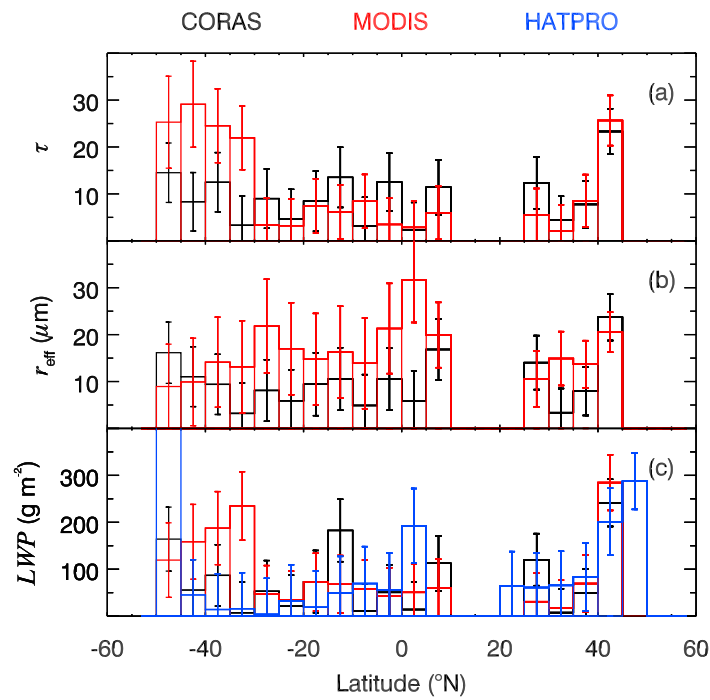


Figure A.7: Meridional 5°-latitude-averages of retrieved (a) τ , (b) r_{eff} , and (c) LWP from 50°S - 50°N from ANT-XXVIII/5. Black and blue colored bars represents retrieval results from CORAS and HATPRO, respectively, along the ship track. Red colored bars includes MODIS Level-2 cloud product retrievals adjusted to cruise track. Data points include all single-layer non-precipitating liquid water clouds.

B Histograms of Cloud Properties

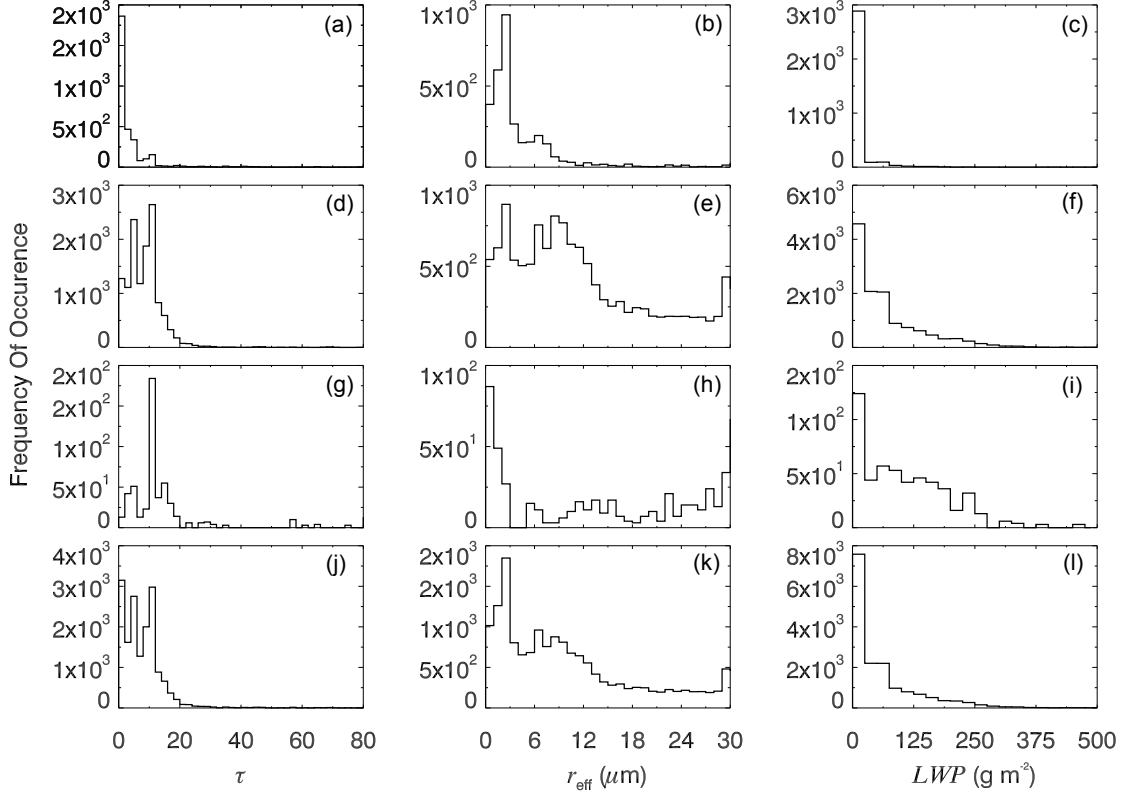


Figure B.1: Histograms of retrieved τ with binsize of 2, r_{eff} in units of μm with binsize of $1 \mu\text{m}$, and LWP in units of g m^{-2} with binsize of 25g m^{-2} , containing all liquid water clouds, separated into (a-c) cloud class 1, (d-f) cloud class 2, and (g-i) cloud class 3, and (j-k) all cloud classes from cruise leg ANT-XXVII/4.

Table B.1: Minimum, first quartile, median, third quartile, maximum, interquartile range, and percentile range values of retrieved cloud properties for individually and all cloud classes containing data from cruise leg ANT-XXVII/4.

		<i>min</i>	<i>P</i> ₂₅	<i>med</i>	<i>P</i> ₇₅	<i>max</i>	<i>IQR</i>	<i>PR</i>
cloud class 1 (<i>N</i> = 3183)	τ	0.1	0.5	1.4	4.2	79.9	3.7	9.8
	r_{eff} (μm)	0.0	1.7	2.5	5.0	30.0	3.3	7.8
	<i>LWP</i> (g m^{-2})	0.0	0.5	1.6	4.4	1333.3	3.9	23.5
cloud class 2 (<i>N</i> = 12697)	τ	0.1	4.8	8.5	10.2	80.0	5.4	12.4
	r_{eff} (μm)	0.0	5.0	9.7	17.0	30.0	12.0	24.3
	<i>LWP</i> (g m^{-2})	0.0	11.7	46.5	98.3	786.7	86.6	175.1
cloud class 3 (<i>N</i> = 521)	τ	0.1	9.3	10.2	14.7	80.0	5.4	22.4
	r_{eff} (μm)	0.0	1.8	14.8	27.2	30.0	25.4	30.0
	<i>LWP</i> (g m^{-2})	0.0	32.2	88.9	158.9	455.0	126.7	229.9
all cloud classes (<i>N</i> = 16401)	τ	0.1	3.4	7.2	10.0	80.0	6.6	13.5
	r_{eff} (μm)	0.0	3.0	8.2	17.3	30.0	14.3	27.1
	<i>LWP</i> (g m^{-2})	0.0	3.4	30.6	99.4	1333.3	96.0	206.1

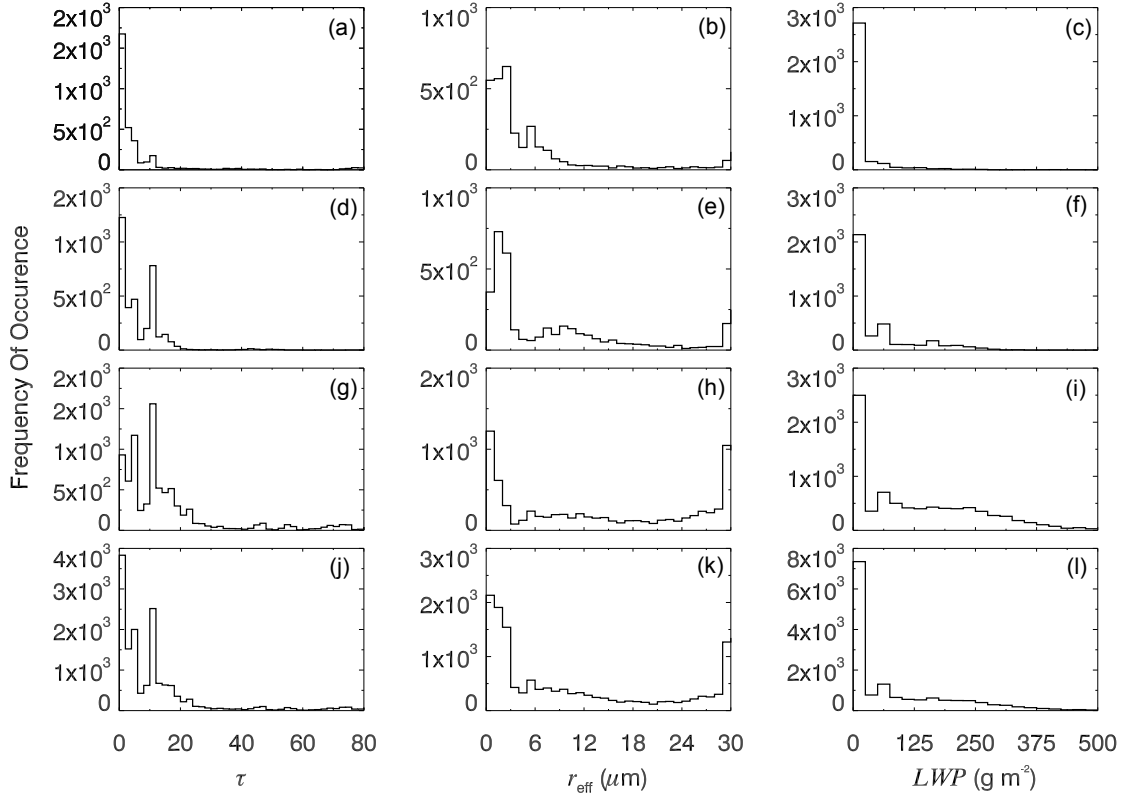


Figure B.2: Histograms of retrieved τ with binsize of 2, r_{eff} in units of μm with binsize of $1 \mu\text{m}$, and *LWP* in units of g m^{-2} with binsize of 25g m^{-2} , containing all liquid water clouds, separated into (a-c) cloud class 1, (d-f) cloud class 2, and (g-i) cloud class 3, and (i-k) all cloud classes from cruise leg ANT-XXVIII/5.

Table B.2: Minimum, first quartile, median, third quartile, maximum, interquartile range, and percentile range values of retrieved cloud properties for individually and all cloud classes containing data from cruise leg ANT-XXVIII/5.

		<i>min</i>	<i>P</i> ₂₅	<i>med</i>	<i>P</i> ₇₅	<i>max</i>	<i>IQR</i>	<i>PR</i>
cloud class 1 (<i>N</i> = 3311)	τ	0.1	0.5	1.9	5.0	80.0	4.5	16.8
	r_{eff} (μm)	0.0	1.6	2.7	6.7	30.0	5.1	21.0
	<i>LWP</i> (g m^{-2})	0.0	0.5	1.7	12.1	1333.3	11.5	73.7
cloud class 2 (<i>N</i> = 3647)	τ	0.1	1.2	4.4	10.0	80.0	8.8	13.4
	r_{eff} (μm)	0.0	1.7	4.1	13.1	30.0	11.4	28.7
	<i>LWP</i> (g m^{-2})	0.0	1.1	4.8	64.5	1292.9	63.4	165.9
cloud class 3 (<i>N</i> = 8233)	τ	0.1	4.7	10.0	17.3	80.0	12.6	32.8
	r_{eff} (μm)	0.0	2.4	14.7	28.9	30.0	26.5	30.0
	<i>LWP</i> (g m^{-2})	0.0	2.8	103.7	228.3	1333.3	225.5	322.8
all cloud classes (<i>N</i> = 15191)	τ	0.1	1.9	7.1	13.4	80.0	11.5	23.1
	r_{eff} (μm)	0.0	1.8	7.6	29.5	30.0	27.7	29.8
	<i>LWP</i> (g m^{-2})	0.0	1.2	36.3	224.3	1333.3	223.1	950.1

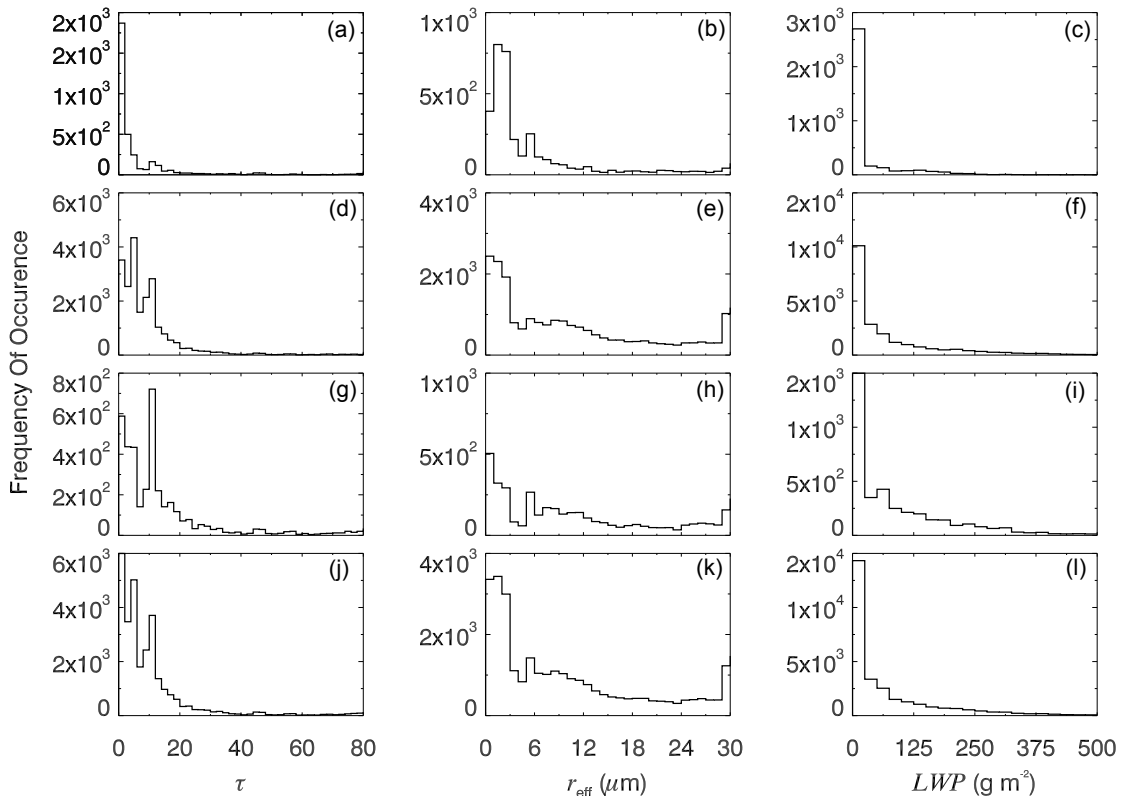


Figure B.3: Histograms of retrieved τ with binsize of 2, r_{eff} in units of μm with binsize of $1 \mu\text{m}$, and *LWP* in units of g m^{-2} with binsize of 25g m^{-2} , containing all liquid water clouds, separated into (a-c) cloud class 1, (d-f) cloud class 2, and (g-i) cloud class 3, and (i-k) all cloud classes from cruise leg ANT-XXIX/1.

Table B.3: Minimum, first quartile, median, third quartile, maximum, interquartile range, and percentile range values of retrieved cloud properties for individually and all cloud classes containing data from cruise leg ANT-XXIX/1.

		<i>min</i>	<i>P</i> ₂₅	<i>med</i>	<i>P</i> ₇₅	<i>max</i>	<i>IQR</i>	<i>PR</i>
cloud class 1 (<i>N</i> = 3183)	τ	0.1	0.5	1.7	5.2	80.0	4.7	16.5
	r_{eff} (μm)	0.0	1.6	2.5	6.3	30.0	4.7	17.0
	<i>LWP</i> (g m^{-2})	0.0	0.5	1.7	16.7	1333.3	16.1	115.8
cloud class 2 (<i>N</i> = 21777)	τ	0.1	3.6	6.7	10.7	80.0	7.1	18.1
	r_{eff} (μm)	0.0	2.2	8.4	18.1	30.0	15.9	28.2
	<i>LWP</i> (g m^{-2})	0.0	3.3	31.8	105.6	1333.3	102.3	233.0
cloud class 3 (<i>N</i> = 3870)	τ	0.1	3.7	10.0	15.8	80.0	12.1	29.8
	r_{eff} (μm)	0.0	2.3	8.6	18.8	30.0	16.5	28.4
	<i>LWP</i> (g m^{-2})	0.0	2.4	54.3	144.7	1333.3	142.3	270.0
all cloud classes (<i>N</i> = 29222)	τ	0.1	2.9	6.1	11.1	80.0	8.2	20.2
	r_{eff} (μm)	0.0	2.1	7.3	21.8	30.0	19.7	29.2
	<i>LWP</i> (g m^{-2})	0.0	2.3	27.0	136.2	1333.3	133.8	333.0

Bibliography

- Althausen, D., Engelmann, R., Baars, H., Heese, B., Ansmann, A., Müller, D., and Kompula, M.: Portable Raman Lidar PollyXT for automated profiling of aerosol backscatter, extinction, and depolarization, *J. Atmos. Oceanic Technol.*, 26, 2366–2378, 2009.
- Anderson, G., Clough, S., Kneizys, F., Chetwynd, J., and Shettle, E.: AFGL Atmospheric constituent profiles (0–120 km), Tech. Rep. AFGL-TR-86-0110, AFGL (OPI), Hanscom AFB, MA 01736, 1986.
- Ansmann, A. and Müller, D.: LIDAR: Range-Resolved Optical Remote Sensing of the Atmosphere, chap. Lidar and Atmospheric Aerosol Particles, pp. 105–141, Springer Science+Business Media Inc., 2005.
- Ansmann, A., Bösenberg, J., Brogniez, G., Elouragini, S., Flamant, P. H., Klapheck, K., Linn, H., Meneger, L., Michaelis, W., Riebesell, M., Senff, C., Thro, P.-Y., Wandinger, U., and Weitkamp, C.: Lidar network observations of cirrus morphological and scattering properties during the International Cirrus Experiment 1989: The 18 October 1989 case study and statistical analysis, *J. Appl. Met.*, 32, 1608–1622, 1993.
- Ansmann, A., Wagner, F., Althausen, D., Müller, D., Herber, A., and Wandinger, U.: European pollution outbreaks during ACE 2: Lofted aerosol plumes observed with Raman lidar at the Portuguese coast, *J. Geophys. Res. Atmos.*, 106, 20 725–20 733, DOI: 10.1029/2000JD000091, 2001.
- Auel, H., ed.: Reports on Polar and Marine Research. The Expedition of the Research Vessel "Polarstern" to the Antarctic in 2012 (ANT-XXIX/1), vol. 670, Alfred-Wegener-Institute for Polar and Marine Research, Bremerhaven, Germany, 2013.
- Bannehr, L. and Glover, V.: Preprocessing of airborne pyranometer data, Tech. rep., NCAR Tech. Note NCAR/TN-3641+STR, 35 pp., 1991.
- Bannehr, L. and Schwiesow, R.: A technique to account for the misalignment of pyranometers installed on aircraft, *J. Atmos. Oceanic Technol.*, 10, 774–777, 1993.
- Baran, A. J.: From the single-scattering properties of ice crystals to climate prediction: A way forward, *Atmos. Res.*, 112, 45–69, 2012.
- Baum, B. A., Heymsfield, A. J., Yang, P., and Bedka, S. T.: Bulk scattering properties for the remote sensing of ice clouds. Part I: Microphysical data and models, *J. Appl. Meteor.*, 44, 1885–1895, 2005a.

- Baum, B. A., Yang, P., Heymsfield, A. J., Platnick, S., King, M. D., Hu, Y. X., and Bedka, S. T.: Bulk scattering properties for the remote sensing of ice clouds. Part II: Narrowband models, *J. Appl. Meteor.*, 44, 1896–1911, 2005b.
- Baum, B. A., Yang, P., Nasiri, S., Heidinger, A. K., Heymsfield, A., and Li, J.: Bulk scattering properties for the remote sensing of ice clouds. Part III: High-resolution spectral models from 100 to 3250 cm⁻¹, *J. Appl. Meteor.*, 46, 423–434, 2007.
- Bierwirth, E.: Airborne measurements of the spectral surface albedo over morocco and its influence on the radiative forcing of saharan dust, Ph.D. thesis, Johannes Gutenberg University Mainz, Germany, 2008.
- Boers, R., Jensen, J. B., and Krummel, P. B.: Microphysical and radiative structure of marine stratocumulus clouds over the Southern Ocean: Summer results and seasonal differences, *Q.J.R. Meteorol. Soc.*, 124, 151–168, 1998a.
- Boers, R., Mitchell, R., and Krummel, P.: Correction of aircraft pyranometer measurements for diffuse radiance and alignment errors, *J. Geophys. Res.*, 103, 16 753–16 758, 1998b.
- Boers, R., Acarreta, J. R., and Gras, J. L.: Satellite monitoring of the first indirect aerosol effect: Retrieval of the droplet concentration of water clouds, *J. Geophys. Res.*, 111, D22 208, DOI: 10.1029/2005JD006838, 2006.
- Bohren, C. F. and Huffman, D. R.: *Absorption and Scattering of Light by Small Particles*, Wiley-Interscience, New York, 1998.
- Bony, S. and Dufresne, J.-L.: Marine boundary layer clouds at the heart of tropical cloud feedback uncertainties in climate models, *Geophys. Res. Lett.*, 32, L20 806, DOI: 10.1029/2005GL023851, 2005.
- Boucher, O., Randall, D., Artaxo, P., Bretherton, C., Feingold, G., Forster, P., Kerminen, V. M., Kondo, Y., Liao, H., Lohmann, U., Rasch, P., Satheesh, S. K., Sherwood, S., B., S., and Zhang, X. Y.: Clouds and Aerosols, in *Climate Change 2013: The Physical Sciences Basis. Contribution of Working Group I to the Fifth Assessment Report of the Intergovernmental Panel on Climate Change*, edited by T. F. Stocker, D. Qin, G. K. Plattner, M. Tignor, S. K. Allen, J. Boschung, A. Nauels, V. Xia, V. Bex, and P. M. Midgley, Cambridge University Press, Cambridge, United Kingdom and New York, NY, USA, 2013.
- Brückner, M., Pospichal, B., Macke, A., and Wendisch, M.: A new multispectral cloud retrieval method for ship-based solar transmissivity measurements, *J. Geophys. Res. Atmos.*, 119, 11.338–11.354, DOI: 10.1002/2014JD021775, 2014.
- Bumke, K., ed.: *Reports on Polar and Marine Reserach. The Expedition of the Research Vessel "Polarstern" to the Antarctic in 2012 (ANT-XXVIII/5)*, vol. 654, Alfred-Wegener-Institute for Polar and Marine Research, Bremerhaven, Germany, 2012.
- Bumke, K., Schlundt, M., Kalisch, J., Macke, A., and Kleta, H.: Measured and parameterized energy fluxes estimated for Atlantic transects of R/V Polarstern, *J. Phys. Oceanogr.*, 44, 482–491, DOI: 10.1175/JPO-D-13-0152.1, 2014.

- Buras, R., Dowling, T., and Emde, C.: New secondary-scattering correction in DISORT with increased efficiency for forward scattering RID B-5447-2010, *J. Quant. Spectrosc. Ra.*, 112, 2028–2034, DOI: 10.1016/j.jqsrt.2011.03.019, 2011.
- Caldwell, P. and Bretherton, C. S.: Large-eddy simulation of the diurnal cycle in southeast Pacific stratocumulus, *J. Atmos. Sci.*, 66, 432–449, 2009.
- Chandrasekhar, S.: Radiative transfer, Oxford University Press, London, UK, 1950.
- Chang, F. L. and Li, Z. Q.: Estimating the vertical variation of cloud droplet effective radius using multispectral near-infrared satellite measurements, *J. Geophys. Res.*, 107, 4257, 2002.
- Chang, F. L. and Li, Z. Q.: Retrieving vertical profiles of water-cloud droplet effective radius: Algorithm modification and preliminary application, *J. Geophys. Res.*, 108, 4763, 2003.
- Chen, R. Y., Chang, F. L., Li, Z. Q., Ferraro, R., and Weng, F. Z.: Impact of the vertical variation of cloud droplet size on the estimation of cloud liquid water path and rain detection, *J. Atmos. Sci.*, 64, 3843–3853, 2007.
- Chen, R. Y., Wood, R., Li, Z. Q., Ferraro, R., and Chang, F. L.: Studying the vertical variation of cloud droplet effective radius using ship and space-borne remote sensing data, *J. Geophys. Res.*, 113, D00A02, 2008.
- Chen, T., Rossow, W., and Zhang, Y.: Radiative effects of cloud-type variations, *J. Climate*, 13, 264–286, 2000.
- Chen, Y. C., Xue, L., Lebo, Z. J., Wang, H., Rasmussen, R. M., and Seinfeld, J. H.: A comprehensive numerical study of aerosol-cloud-precipitation interactions in marine stratocumulus, *Atmos. Chem. Phys.*, 11, 9749–9769, DOI: 10.5194/acp-11-9749-2011, 2011.
- Chiu, J. C., Marshak, A., Knyazikhin, Y., Pilewskie, P., and Wiscombe, W. J.: Physical interpretation of the spectral radiative signature in the transition zone between cloud-free and cloudy regions, *Atmos. Chem. Phys.*, 9, 1419–1430, DOI: 10.5194/acp-9-1419-2009, 2009.
- Chiu, J. C., Marshak, A., Huang, C.-H., Várnai, T., Hogan, R. J., Giles, D. M., Holben, B. N., Ot’Connor, E. J., Knyazikhin, Y., and Wiscombe, W. J.: Cloud droplet size and liquid water path retrievals from zenith radiances measurements: examples from the Atmospheric Radiation Measurements Program and the Aerosol Robotic Network, *Atmos. Chem. Phys.*, 12, 10313–10329, DOI: 10.5194/acp-12-10313-2012, 2012.
- Choi, Y.-S. and Ho, C.-H.: Radiative effect of cirrus with different optical properties over the tropics in MODIS and CERES observations, *Geophys. Res. Lett.*, 33, L21811, DOI: 10.1029/2006GL027403, 2006.
- Christensen, M. W., Carrió, G. G., Stephens, G. L., and Cotton, W. R.: Radiative impacts of free-tropospheric clouds on the properties of marine stratocumulus, *J. Atmos. Sci.*, 70, 3102–3118, 2013.

- Ch \ddot{y} lek, P.: Extinction and liquid water content of fogs and clouds, *J. Atmos. Sci.*, 35, 296–300, 1977.
- Coddington, O., Pilewskie, P., and Vukicevic, T.: The Shannon information content of hyperspectral shortwave cloud albedo measurements: Quantification and practical applications, *J. Geophys. Res.*, 117, D04205, DOI: 10.1029/2011JD016771, 2012.
- Comstock, K. K., Bretherton, C. S., and Yuter, S. E.: Mesoscale variability and drizzle in southeast Pacific stratocumulus, *J. Atmos. Sci.*, 62, 3792–3807, 2005.
- Cox, C. and Munk, W.: Measurement of the roughness of the sea surface from photographs of the sun’s glitter, *J. Opt. Soc. Am. A.*, 44, 838–850, 1954.
- Crewell, S. and Löhnert, U.: Accuracy of cloud liquid water path from groundbased microwave radiometry 2. Sensor accuracy and synergy, *Radio Sci.*, 38(3), 8042, DOI: 10.1029/2002RS002634, 2003.
- Crewell, S., Czekala, H. and Löhnert, U., Rose, T., Simmer, C., and Zimmermann, R.: Microwave Radiometer for Cloud Carthography: A 22-channel ground-based microwave radiometer for atmospheric research, *Radio Sci.*, 36(4), 621–638, 2001.
- Crowther, B.: The Design, Construction, and Calibration of a Spectral Diffuse/Global Irradiance Meter, Ph.D. thesis, University of Arizona, United States of America, 1997.
- Czekala, H., Simmer, C., and Thiele, A.: Discrimination of cloud and rain liquid water path by ground-based polarized microwave radiometry, *Geophys. Res. Lett.*, 28, 267–270, 2001.
- Dong, X. and Mace, G.: Profiles of low-level stratus cloud microphysics deduced from ground-based measurements, *J. Atmos. Oceanic Technol.*, 20, 42–53, 2003.
- Edwards, J., Havemann, S., Thelen, J.-C., and Baran, A.: A new parametrization for the radiative properties of ice crystals: Comparison with existing schemes and impact in a GCM, *Atmos. Res.*, 83, 19 – 35, DOI: DOI:10.1016/j.atmosres.2006.03.002, 2007.
- Ehrlich, A.: The impact of ice crystals on radiative forcing and remote sensing of arctic boundary-layer mixed-phase clouds, Ph.D. thesis, Johannes Gutenberg University Mainz, Germany, 2009.
- Ehrlich, A., Bierwirth, E., Wendisch, M., Gayet, J.-F., Mioche, G., Lampert, A., and Heintzenberg, J.: Cloud phase identification of Arctic boundary-layer clouds from airborne spectral reflection measurements: Test of three approaches, *Atmos. Chem. Phys.*, 8, 7493–7505, 2008a.
- Ehrlich, A., Wendisch, M., Bierwirth, E., Herber, A., and Schwarzenböck, A.: Ice crystal shape effects on solar radiative properties of Arctic mixed-phase clouds - Dependence on microphysical properties, *Atmos. Res.*, 88, 266–276, 2008b.
- Eichler, H., Ehrlich, A., Wendisch, M., Mioche, G., Gayet, J.-F., Wirth, M., Emde, C., and Minikin, A.: Influence of ice crystal shape on retrieval of cirrus optical thickness and effective radius: A case study, *J. Geophys. Res.*, 114, D19203, DOI: doi:10.1029/2009JD012215, 2009.

- El Naggar, S., ed.: Reports on Polar and Marine Reserach. The Expedition of the Research Vessel "Polarstern" to the Antarctic in 2011 (ANT-XXVII/4), vol. 639, Alfred-Wegener-Institute for Polar and Marine Research, Bremerhaven, Germany, 2011.
- El Naggar, S. and Fahrbach, E., eds.: Handbuch FS Polarstern. Ein Leitfaden zu Planung und Durchführung von Expeditionen mit FS Polarstern, Alfred-Wegener-Institute for Polar and Marine Research, Bremerhaven, 2010.
- El Naggar, S. and Macke, A., eds.: Reports on Polar and Marine Reserach. The Expedition of the Research Vessel "Polarstern" to the Antarctic in 2009 (ANT-XXVI/1), vol. 614, Alfred-Wegener-Institute for Polar and Marine Research, Bremerhaven, Germany, 2010.
- Feingold, G., Furrer, R., Pilewskie, P., Remer, L. A., Min, Q. L., and Jonsson, H.: Aerosol indirect effect studies at Southern Great Plains during the May 2003 Intensive Operations Period, *J. Geophys. Res.*, 111, D05S14, DOI: 10.1029/2004JD005648, 2006.
- Fernald, F. G.: Analysis of atmospheric lidar observations: some comments, *Appl. Opt.*, 23, 652–653, 1984.
- Fowler, L. D. and Randall, D. A.: A global radiative-convective feedback, *Geophys. Res. Lett.*, 21, No. 18, 2035–2038, 1994.
- Franke, K., Ansmann, A., Müller, D., Althausen, D., Wagner, F., and Scheele, R.: One-year observations of particle lidar ratio over the tropical Indian Ocean with Raman lidar, *Geophys. Res. Lett.*, 28, 4559–4562, 2001.
- Fu, Q. and Liou, K.: Parameterization of the radiative properties of cirrus clouds, *J. Atmos. Sci.*, 50, 2008–2025, 1993.
- Garrett, T. J. and Zhao, C.: Ground-based remote sensing of thin clouds in the arctic, *Atmos. Meas. Tech.*, 6, 1227–1243, DOI: 10.5194/amt-6-1227-2013, 2013.
- Grenfell, T. C. and Warren, S. G.: Representation of a nonspherical ice particle by a collection of independent spheres for scattering and absorption of radiation, *J. Geophys. Res.*, 104, 31.697–31.709, 1999.
- Gueymard, C. A.: The sun's total and spectral irradiance for solar energy applications and solar radiation models, *Solar Energy*, 76, 423–453, 2004.
- Han, Q., Rossow, W., and Lacis, A.: Near-global survey of effective droplet radii in liquid water clouds using ISCCP data, *J. Climate*, 7, 465–497, 1994.
- Hansen, J. and Travis, L.: Light scattering in planetary atmospheres, *Space Sci. Rev.*, 16, 527–610, 1974.
- Harrison, E. F., Minnis, P., Barkstrom, B. R., Ramanathan, V., Cess, R. D., and Gibson, G. G.: Seasonal variation of cloud radiative forcing derived from Earth Radiation Budget Experiment, *J. Geophys. Res.*, 95, 18 687–18 703, 1990.
- Hartmann, D. L., Ockertbell, M. E., and Michelsen, M. L.: The effect of cloud type on earths energy-balance - global analysis, *J. Climate*, 5, 1281–1304, 1992.

- Heinle, A., Macke, A., and Srivastav, A.: Automatic cloud classification of whole sky images, *Atmos. Meas. Tech.*, 3, 557–567, 2010.
- Horvath, A. and Davies, R.: Anisotropy of water cloud reflectance: A comparison of measurements and 1D theory, *Geophys. Res. Lett.*, 31, doi:10.1029/2003GL018386, 2004.
- Iwabuchi, H. and Hayasaka, T.: Effects of cloud horizontal inhomogeneity on the optical thickness retrieved from moderate-resolution satellite data, *J. Atmos. Sci.*, 59, 2227–2242, DOI: 10.1175/1520-0469(2002)059<2227:E0CHI0>2.0.CO;2, 2002.
- Iwabuchi, H. and Hayasaka, T.: A multi-spectral non-local method for retrieval of boundary layer cloud properties from optical remote sensing data, *Remote Sens. Environ.*, 88, 293–308, 2003.
- Jäkel, E., Wendisch, M., Kniffka, A., and Trautmann, T.: Airborne system for fast measurements of upwelling and downwelling spectral actinic flux densities, *Appl. Opt.*, 44, 434–444, 2005.
- Jäkel, E., Walther, J., and Wendisch, M.: Thermodynamic phase retrieval of convective clouds: impact of sensor viewing geometry and vertical distribution of cloud properties, *Atmos. Meas. Tech.*, 6, 539–547, DOI: 10.5194/amt-6-539-2013, 2013.
- Kalisch, J. and Macke, A.: Estimation of the total cloud cover with high temporal resolution and parameterization of short-term fluctuations of sea surface insulation, *Meteorol. Z.*, 17, 603–611, 2008.
- Kanitz, T., Seifert, P., Ansmann, A., Engelmann, R., Althausen, D., Cassicia, C., and Rohwer, E.: Contrasting the impact of aerosol at northern and southern midlatitudes on heterogeneous ice formation, *Geophys. Res. Lett.*, 38, L17802, 1–5, 2011.
- Karstens, U., Simmer, C., and Ruprecht, E.: Remote sensing of cloud liquid water, *Meteor. Atmos. Phys.*, 54, 157–171, DOI: 10.1007/BF01030057, 1994.
- Key, J. R., Yang, P., Baum, B. A., and Nasiri, S. L.: Parameterization of shortwave ice cloud optical properties for various particle habits, *J. Geophys. Res.*, 107, Art. No. 4181, 2002.
- Kikuchi, N., Nakajima, T., Kumagai, H., Kuroiwa, H., Kamei, A., Nakamura, R., and Nakajima, T. Y.: Cloud optical thickness and effective particle radius derived from transmitted solar radiation measurements: Comparison with cloud radar observations, *J. Geophys. Res.*, 111, D07205, DOI: 10.1029/2005JD006363, 2006.
- King, M., Tsay, S.-C., Platnick, S., Wang, M., and Liou, K.-N.: Cloud retrieval algorithms for MODIS: Optical thickness, effective particle radius, and thermodynamic phase, MODIS Algorithm Theoretical Basis Document, No. ATBD-MOD-05, 1997, 1997.
- King, M., Platnick, P., Hubanks, P., Arnold, G., Moody, E., Wind, G., and Wind, B.: Collection 005 Change Summary for the MODIS Cloud Optical Property Algorithm., http://modis-atmos.gsfc.nasa.gov/C005_Changes/C005_CloudOpticalProperties_ver311.pdf, 2006.

- Kipp & Zonen: Instruction Manual CG 4. - Manual Version: 0304, Kipp & Zonen B.V., Delftechpark 36, 2628 Delft, Niederlande, 2001.
- Kipp & Zonen: Instruction Manual CM 21. - Manual Version: 0904, Kipp & Zonen B.V., Delftechpark 36, 2628 Delft, Niederlande, 2004.
- Klett, J. D.: Lidar inversion with variable backscatter/extinction ratios, *Appl. Opt.*, 20, 1638–1643, 1985.
- Kogan, Y. L., Mechem, D. B., and Choi, K.: Effects of sea-salt aerosols on precipitation in simulations of shallow cumulus, *J. Atmos. Sci.*, 69, 463–483, 2012.
- Koren, I., Remer, L. A., Kaufman, Y. J., Rudich, Y., and Martins, J. V.: On the twilight zone between clouds and aerosols, *Geophys. Res. Lett.*, 34, L08 805, DOI: 10.1029/2007GL029253, 2007.
- Kristjansson, J., Edwards, J., and Mitchell, D.: Impact of a new scheme for optical properties of ice crystals on climate of two GCMs, *J. Geophys. Res.*, 105, 10 063–10 079, 2000.
- LeBlanc, S. E., Pilewskie, P., Schmidt, K. S., and Coddington, O.: A generalized method for discriminating thermodynamic phase and retrieving cloud optical thickness and effective radius using transmitted shortwave radiance spectra, *Atmos. Meas. Tech. Discuss.*, 7, 5293–5346, DOI: doi:10.5194/amtd-7-5293-2014, 2014.
- Liou, K.-N.: Influence of cirrus clouds on weather and climate processes: A global perspective, *Mon. Wea. Rev.*, 114, 1167–1199, 1986.
- Loeb, N. G., Wielicki, B. A., Doelling, D. R., Smith, G. L., Keyes, D. F., Kato, S., Manalo-Smith, N., and Wong, T.: Toward optimal closure of the Earth’s top-of-atmosphere radiation budget, *J. Clim.*, 22, 748–766, DOI: 10.1175/2008JCLI2637.1, 2009.
- Löhnert, U. and Crewell, S.: Accuracy of cloud liquid water path from ground-based microwave radiometry 1. Dependency on cloud model statistics, *Radio Sci.*, 38, 8042, DOI: 10.1029/2002RS002654, 2003.
- Löhnert, U., Crewell, S., Simmer, C., and Macke, A.: Profiling cloud liquid water by combining active and passive microwave measurements with cloud model statistics, *J. Atmos. Oceanic Technol.*, 18, 1354–1366, 2001.
- Löhnert, U. E., van Meijgaard, E., Baltink, H. K., Groß, S., and Boers, R.: Accuracy assessment of an integrated profiling technique for operationally deriving profiles of temperature, humidity, and cloud liquid water, *J. Geophys. Res. Atmos.*, 112, D04 205, DOI: 10.1029/2006JD007379, 2007.
- Loveland, T. and Belward, A.: The IGBP-DIS global 1km land cover data set DISCover: first results, *Int. J. Remote Sensing*, 18, 3289–3295, 1997.
- Lynch, D., Sassen, K., Starr, D., and Stephens, G., eds.: *Cirrus*, Oxford University Press, 2002.

- Mace, G. G.: Cloud properties and radiative forcing over the maritime storm tracks of the Southern Ocean and North Atlantic derived from A-Train, *J. Geophys. Res. Atmos.*, 115, D10 201, DOI: 10.1029/2009JD012517, 2010.
- Macke, A.: Scattering of light by polyhedral ice crystals, *Appl. Opt.*, 32, 2780–2788, 1993.
- Macke, A., Francis, P. N., McFarquar, G. M., and Kinne, S.: The role of ice particle shapes and size distributions in the single scattering properties of cirrus clouds, *J. Atmos. Sci.*, 55, 2.874–2.883, 1998.
- Macke, A., Kalisch, J., Zoll, Y., and Bunke, K.: Radiative effects of the cloudy atmosphere from ground and satellite based observations, *EPJ Web of Conferences*, 9, 83–94, 2010.
- Marshak, A., Platnick, S., Varnai, T., Wen, G. Y., and Cahalan, R. F.: Impact of three-dimensional radiative effects on satellite retrievals of cloud droplet sizes, *J. Geophys. Res.*, 111, 2006.
- Marshak, A., Knyazikhin, Y., Chiu, J. C., and Wiscombe, W. J.: Spectral invariant behavior of zenith radiance around cloud edge s observed by ARM SWS, *Geophys. Res. Lett.*, 36, L16 802, DOI: 10.1029/2009GL039366, 2009.
- Mayer, B.: Radiative transfer in the cloudy atmosphere, *Eur. Phys. J. Conferences*, 1, 75–99, 2009.
- Mayer, B. and Kylling, A.: Technical note: The libRadtran software package for radiative transfer calculations - description and examples of use, *Atmos. Chem. Phys.*, 5, 1.855–1.877, 2005.
- McBride, P. J., Schmidt, K. S., Pilewskie, P., Kittelman, A. S., and Wolfe, D. E.: A spectral method for retrieving cloud optical thickness and effective radius from surface-based transmittance measurements, *Atmos. Chem. Phys.*, 11, 7235–7252, DOI: 10.5194/acp-11-7235-2011, 2011.
- McBride, P. J., Schmidt, K. S., Pilewski, P., Walther, A., Heidinger, A. K., Wolfe, D. E., Fairall, C. W., and Lance, S.: CalNex cloud properties retrieved from ship-based spectrometer and comparisions with satellite and aircraft retrieved cloud properties, *J. Geophys. Res.*, 117, D00V23, DOI: 10.1029/2012JD017624, 2012.
- McFarlane, S. A., Marchand, R. T., and Ackerman, T. P.: Retrieval of cloud phase and crystal habit from Multiangle Imaging Spectroradiometer (MISR) and Moderate Resolution Imaging Spectroradiometer (MODIS) data, *J. Geophys. Res.*, 110, Art. No. D14 201, 2005.
- McFarquhar, G., Yang, P., Macke, A., and Baran, A.: A new parameterization of single scattering solar radiative properties for tropical anvils using observed ice crystal size and shape distributions, *J. Atmos. Sci.*, 59, 2458–2478, 2002.
- Mie, G.: Beiträge zur Optik trüber Medien, speziell kolloidaler Metallösungen, *Annalen der Physik*, Vierte Folge, 25, 377–445, 1908.

- Min, Q.-L., Duan, M., and Marchand, R.: Validation of surface retrieved cloud optical properties with in situ measurements at the Atmospheric Radiation Measurement Program (ARM) South Great Plains site, *J. Geophys. Res.*, 108, 4547, DOI: 10.1029/2003JD003385, 2003.
- Nakajima, T. and King, M.: Determination of the optical thickness and effective particle radius of clouds from reflected solar radiation measurements. Part I: Theory, *J. Atmos. Sci.*, 47, 1878–1893, 1990.
- Nakajima, T. and Nakajima, T.: Wide-area determination of cloud microphysical properties from NOAA AVHRR measurements for FIRE and ASTEX regions, *J. Atmos. Sci.*, 52, 4043–4059, 1995.
- Nakajima, T. and Tanaka, M.: Algorithms for radiative intensity calculations in moderately thick atmospheres using a truncation approximation, *J. Quant. Spectrosc. Ra.*, 40, 51–69, 1988.
- Pandithurai, G., Takamura, T., Yamaguchi, J., Miyagi, K., Takano, T., Ishizaka, Y., Dipu, S., and Shimizu, A.: Aerosol effect on cloud droplet size as monitored from surface-based remote sensing over East China Sea region, *Geophys. Res. Lett.*, 36, L13 805, DOI: 10.1029/2009GL038451, 2009.
- Pilewskie, P. and Twomey, S.: Discrimination of ice from water in clouds by optical remote sensing, *Atmos. Res.*, 21, 113–122, 1987.
- Pilewskie, P., Pommier, J., Bergstrom, R., Gore, W., Howard, S., Rabbette, M., Schmid, B., Hobbs, P. V., and Tsay, S. C.: Solar spectral radiative forcing during the Southern African Regional Science Initiative, *J. Geophys. Res.*, 108, doi:10.1029/2002JD002 411, 2003.
- Platnick, S.: Vertical photon transport in cloud remote sensing problems, *J. Geophys. Res.*, 105, 22 919–22 935, 2000.
- Platnick, S. and Twomey, S.: Determining the susceptibility of cloud albedo to changes in droplet concentration with the Advanced Very High Resolution Radiometer, *J. Appl. Meteorol.*, 33, 334–347, 1994.
- Platnick, S., King, M., Ackerman, S., Menzel, W., Baum, B., Riedi, J., and Frey, R.: The MODIS cloud products: Algorithms and examples from TERRA, *IEEE Trans. Geosci. Remote Sens.*, 41, 459–473, 2003.
- Pospichal, B.: Diurnal to annual variability of the Atmospheric Boundary Layer over West Africa: A comprehensive view by remote sensing observations, Ph.D. thesis, University of Köln, Germany, 2009.
- Potter, J.: The delta function approximation in radiative transfer theory, *J. Atmos. Sci.*, 27, 943–949, 1970.
- Ramanathan, V., Cess, R. D., Harrison, E. F., Minnis, P., Barkstrom, B. R., Ahmad, E., and Hartmann, D.: Cloud-radiative forcing and climate: Results from the Earth Radiation Budget Experiment, *Science*, 243, 57–63, 1989.

- Ramanathan, V., Subasilar, B., Zhang, G., Conant, W., Cess, R., Kiehl, J., and Shi, L.: Warm pool heat budget and shortwave cloud forcing: a missing physics?, *Science*, 267, 499–503, 1995.
- Rawlins, F. and Foot, J. S.: Remotely sensed measurements of stratocumulus properties during FIRE using the C130 aircraft multi-channel radiometer, *J. Atmos. Sci.*, 47, 2488–2504, 1990.
- Redemann, J., Zhang, Q., Russell, P. B., Livingston, J. M., and Remer, L. A.: Case studies of aerosol remote sensing in the vicinity of clouds, *J. Geophys. Res. Atmos.*, 114, D06 209, DOI: 10.1029/2008JD010774, 2009.
- Ricchiazzi, P., Yang, S., Gautier, C., and Sowle, D.: SBDART: A research and teaching software tool for plane-parallel radiative transfer in the Earth’s atmosphere, *Bull. Amer. Meteorol. Soc.*, 79, 2101–2114, 1998.
- Rose, T., Crewell, S., Löhnert, U., and Simmer, C.: A network suitable microwave radiometer for operational monitoring of the cloudy atmosphere, *Atmos. Res.*, 75, 183–200, 2005.
- Rose and Czekala: RPG-HATPRO, RPG-TEMPRO, RPG-HUMPRO, RPG-LHUMPRO, RPG-LHATPRO Humidity and Temperature Profilers Operating Manual, Radiometer Physics, 2008.
- Rossow, W. and Schiffer, R.: ISCCP cloud data products, *Bull. Amer. Meteorol. Soc.*, 72, 2–20, 1991.
- Rossow, W., Walker, A., Beuschel, D., and Roiter, M.: International Satellite Cloud Climatology Project (ISCCP) - Documentation of new cloud datasets, Available at <http://isccp.giss.nasa.gov>, 1996.
- Rossow, W. B. and Cairns, B.: Monitoring changes of clouds, *Clim. Chang.*, 31, 305–347, 1995.
- Sasano, Y., Browell, E. V., and Ismail, S.: Error caused by using a constant extinction/backscattering ratio in the lidar solution, *Appl. Opt.*, 24, 3929–3932, 1985.
- Saunders, R. W., Brogniez, G., Buriez, J. C., Meerkötter, R., and Wendling, P.: A comparison of measured and modeled broadband fluxes from aircraft data during the ICE’89 field experiment, *J. Atmos. Oceanic Technol.*, 9, 391–406, 1992.
- Schäfer, M., Bierwirth, E., Ehrlich, A., Heyner, F., and Wendisch, M.: Retrieval of cirrus optical thickness and assessment of ice crystal shape from ground-based imaging spectrometry, *Atmos. Meas. Tech.*, 6, 1855–1868, DOI: 10.5194/amt-6-1855-2013, 2013.
- Schepanski, K., I., T., Todd, M. C., Heinold, B., Bönisch, G., Laurent, B., and Macke, A.: Meteorological processes forcing Saharan dust emission inferred from MSG-SEVIRI observations of subdaily dust source activation and numerical models, *J. Geophys. Res.*, 114, D10 201, DOI: 10.1029/2008JD010325, 2009.

- Schofield, R., Daniel, J. S., Portmann, R. W., Miller, H. L., Solomon, S., Eubank, C. S., Melamed, M. L., Langford, A. O., Shupe, M. D., and Turner, D. D.: Retrieval of effective radius and liquid water path from ground-based instruments: A case study at Barrow, Alaska, *J. Geophys. Res.*, 112, D21 203, 2007.
- Seethala, C. and Horvath, A.: Global assessment of AMSR-E and MODIS cloud liquid water path retrievals in warm oceanic clouds, *J. Geophys. Res. Atmos.*, 115, D13 202, DOI: 10.1029/2009JD012662, 2010.
- Seidel, D. J., Ao, C. O., and Li, K.: Estimating climatological planetary boundary layer heights from radiosonde observations: Comparison of methods and uncertainty analysis, *J. Geophys. Res.*, 115, D16 113, DOI: 10.1029/2009JD013680, 2010.
- Seifert, P., Ansmann, A., Mattis, I., Wandinger, U., Tesche, M., Engelmann, R., Müller, D., Perez, C., and Hausteiner, K.: Saharan dust and heterogeneous ice formation: Eleven years of cloud observations at a central European EARLINET site, *J. Geophys. Res. Atmos.*, 115, D20 201, DOI: 10.1029/2009JD013222, 2010.
- Shettle, E.: Models of aerosols, clouds and precipitation for atmospheric propagation studies, in *Atmospheric propagation in the uv, visible, ir and mm-region and related system aspects*, no. 454 in AGARD Conference Proceedings, 1989.
- Smirnov, A., Holben, B. N., Slutsker, I., Giles, D. M., McClain, C. R., Eck, T. F., Sakerin, S. M., Macke, A., Croot, P., Zibordi, G., Quinn, P. K., Sciare, J., Kinne, S., Harvey, M., Smyth, T. J., Piketh, S., Zielinski, T., Proshutinsky, A., Goes, J. I., Nelson, N. B., Larouche, P., Radionov, V. F., Goloub, P., Krishna Moorthy, K., Matarrese, R., Robertson, E. J., and Jourdin, F.: Maritime Aerosol Network as a component of Aerosol Robotic Network, *J. Geophys. Res.*, 114, D06 204, DOI: 10.1029/2008JD011257, 2009.
- Stamnes, K., Hendriksen, K., and Ostensen, P.: Simultaneous measurement of UV radiation received by the biosphere and total ozone amount, *Geophys. Res. Lett.*, 15, 784–787, 1988.
- Stephens, G., Tsay, S.-C., Stackhouse Jr., P., and Flatau, P.: The relevance of the microphysical and radiative properties of cirrus clouds to climate and climatic feedback, *J. Atmos. Sci.*, 47, 1742–1753, 1990.
- Stephens, G., Engelen, R., Vaughan, M., and Anderson, T.: Toward retrieving properties of the tenuous atmosphere using space-based lidar measurements, *J. Geophys. Res.*, 106, 28 143–28 157, 2001.
- Stephens, G., Vane, D., Boain, R., Mace, G., Sassen, K., Wang, Z., Illingworth, A., O'Connor, E., Rossow, W., Durden, S., Miller, S., Austin, R., Benedetti, A., Mitrescu, C., and the CloudSat Science Team: The CloudSat mission and the A-train, *Bull. Amer. Meteorol. Soc.*, 83, 1771–1790, 2002.
- Stocker, T. F., Qin, D., Plattner, G. K., Tignor, M., Allen, S. K., Boschung, J., Nauels, A., Xia, Y., Bex, V., and Midgley, P. M., eds.: *Climate Change 2013: The Physical Science Basis*. Working Group I Contribution to the Fifth Assessment Report of the Intergovernmental Panel on Climate Change, Cambridge University Press, UK, 2013.

- Su, W. Y., Schuster, G. L., Loeb, N. G., Rogers, R. R., Ferrare, R. A., Hostetler, C. A., Hair, J. W., and Obland, M. D.: Aerosol and cloud interaction observed from high spectral resolution lidar data, *J. Geophys. Res. Atmos.*, 113, D24 202, 2008.
- Takano, Y. and Liou, K.-N.: Solar radiative transfer in cirrus clouds. Part I: Single-scattering and optical properties of hexagonal ice crystals, *J. Atmos. Sci.*, 46, 1–19, 1989.
- Taylor, K. E. and Ghan, S. J.: An analysis of cloud liquid water feedback and global climate sensitivity in a general circulation model, *J. Climate*, 5, 907–919, 1992.
- Tegen, I., Harrison, S. P., Kohfeld, K., Prentice, I. C., Coe, M., and Heimann, M.: Impact of vegetation and preferential source areas on global dust aerosol: Results from a model study, *J. Geophys. Res.*, 107(D21), 4576, DOI: 10.1029/2001JD000963, 2002.
- Trenberth, K. E., Fasullo, J. T., and Mackaro, J.: Atmospheric moisture transports from ocean to land and global energy flows in reanalyses, *J. Climate*, 24, 4907–4924, 2011.
- Vaisala: CL51 Ceilometer for High-Range Cloud Height Detection, Vaisala Headquarters, Vanha Nurmijärventie 21, 01670 Vantaa, Finland, www.vaisala.com, 2010.
- Varnai, T. and Marshak, A.: Statistical analysis of the uncertainties in cloud optical depth retrievals caused by three-dimensional radiative effects, *J. Atmos. Sci.*, 58, 1540–1548, 2001.
- Varnai, T. and Marshak, A.: Observations of the three-dimensional radiative effects that influence MODIS cloud optical thickness retrievals, *J. Atmos. Sci.*, 59, 1607–1618, 2002a.
- Varnai, T. and Marshak, A.: Observations of three-dimensional radiative effects that influence satellite retrievals of cloud properties, *Q. J. Hung. Meteorol. Serv.*, 106, 265–278, 2002b.
- Wandinger, U.: Multiple-scattering influence on extinction- and backscatter-coefficient measurement with Raman and High-Spectral-Resolution lidars, *Appl. Opt.*, 37, 417–427, 1998.
- Wang, S., Zheng, X., and Jiang, Q.: Strong sheared stratocumulus convection: An observationally based large-eddy simulation study, *Atmos. Chem. Phys.*, 12, 5223–5235, 2012.
- Wang, Z. and Sassen, K.: Cirrus cloud microphysical property retrieval using lidar and radar measurements. Part I: Algorithm description and comparison with in situ data, *J. Appl. Meteorol.*, 41, 218–229, 2002.
- Wang, Z., Sassen, K., Whiteman, D. N., and Demoz, B. B.: Studying altocumulus with ice virga using ground-based active and passive sensors, *J. Appl. Meteorol.*, 43, 449–460, 2004.
- Weaver, C. P. and Ramanathan, V.: Relationships between large-Scale vertical velocity, static stability, and cloud radiative forcing over Northern Hemisphere extratropical oceans, *J. Climate*, 10, 2871–2887, 1997.
- Wen, G. Y., Marshak, A., and Cahalan, R. F.: Importance of molecular Rayleigh scattering in the enhancement of clear sky reflectance in the vicinity of boundary layer cumulus clouds, *J. Geophys. Res. Atmos.*, 113, D24 207, DOI: 10.1029/2008JD010592, 2008.

- Wendisch, M. and Mayer, B.: Vertical distribution of spectral solar irradiance in the cloudless sky: A case study, *Geophys. Res. Lett.*, 30, Art. No. 1183, 2003.
- Wendisch, M. and Yang, P.: *Theory of Atmospheric Radiative Transfer – A Comprehensive Introduction*, Wiley-VCH Verlag GmbH & Co. KGaA, Weinheim, Germany, ISBN: 978-3-527-40836-8, 2012.
- Wendisch, M., Heintzenberg, J., and Bussemer, M.: Measurement-based aerosol forcing calculations: the influence of model complexity, *Meteor. Z.*, 10, 45–60, 2001.
- Wendisch, M., Pilewskie, P., Jäkel, E., Schmidt, S., Pommier, J., Howard, S., Jonsson, H. H., Guan, H., Schröder, M., and Mayer, B.: Airborne measurements of areal spectral surface albedo over different sea and land surfaces, *J. Geophys. Res.*, 109, Art. No. D08 203, DOI: doi:10.1029/2003JD004392, 2004.
- Wendisch, M., Pilewskie, P., Pommier, J., Howard, S., Yang, P., Heymsfield, A. J., Schmitt, C. G., Baumgardner, D., and Mayer, B.: Impact of cirrus crystal shape on solar spectral irradiance: A case study for subtropical cirrus, *J. Geophys. Res.*, 110, Art. No. D03 202, 2005.
- Wendisch, M., Yang, P., and Pilewskie, P.: Effects of ice crystal habit on thermal infrared radiative properties and forcing of cirrus, *J. Geophys. Res.*, 112, D03 202, DOI: 10.1029/2006JD007899, 2007.
- Werner, F., Siebert, H., Pilewskie, P., Schmeissner, T., Shaw, R. A., and Wendisch, M.: New airborne retrieval approach for trade wind cumulus properties under overlying cirrus, *J. Geophys. Res. Atmos.*, 118, 3634–3649, DOI: 10.1002/jgrd.50334, 2013.
- Wielicki, B., Cess, R., King, M., Randall, D., and Harrison, E.: Mission to planet Earth: Role of clouds and radiation in climate, *Bull. Amer. Meteorol. Soc.*, 76, 2125–2153, 1995.
- Wieliczka, D. M., Weng, S. S., and Querry, M. R.: Wedge shaped cell for highly absorbent liquids - Infrared Optical-constants of water, *Appl. Opt.*, 28, 1714–1719, 1989.
- Wilcox, E. M.: Stratocumulus cloud thickening beneath layers of absorbing smoke aerosol, *Atmos. Chem. Phys.*, 10, 18 635–18 659, 2010.
- Winker, D. M., Pelon, J., and McCormick, M. P.: The CALIPSO mission: Spaceborne lidar for observation of aerosols and clouds, *Proc. SPIE*, 4893, 1–11, 2003.
- Wiscombe, W.: Doubling initialization revisited, *J. Quant. Spectrosc. Ra.*, 18, 245–248, 1977.
- Wiscombe, W.: Improved Mie scattering algorithms, *Appl. Opt.*, 19, 1505–1509, 1980.
- Wood, R.: Parametrization of the effect of drizzle upon the droplets effective radius in stratocumulus clouds, *Q.J.R. Meteorol. Soc.*, 126, 3309–3324, DOI: 10.1002/qj.49712657015, 2000.
- Wood, R.: Stratocumulus clouds, *Mon. Wea. Rev.*, 140, 2373–2423, 2012.

- Wood, R. and Hartmann, D. L.: Spatial variability of liquid water path in marine low cloud: The importance of mesoscale cellular convection, *J. Climate*, 19, 1748–1764, 2006.
- Yang, H. Y., Dobbie, S., Herbert, R., Connolly, P., Gallagher, M., Ghosh, S., Al-Jumur, S. M. R. K., and Clayton, J.: The effect of observed vertical structure, habits, and size distribution on the solar radiative properties and cloud evolution of cirrus clouds, *Quart. J. R. Met. Soc.*, 138, 1221–1232, 2012.
- Yang, P. and Liou, K. N.: Finite-difference time domain method for light scattering by small ice crystals in three-dimensional space, *J. Opt. Soc. Am. A.*, 13, 2.072–2.085, 1996.
- Yang, P., Liou, K. N., Wyser, K., and Mitchell, D.: Parameterization of the scattering and absorption properties of individual ice crystals, *J. Geophys. Res.*, 105, 4.699–4.718, 2000.
- Yang, P., Wei, H. L., Huang, H. L., Baum, B. A., Hu, Y. X., Kattawar, G. W., Mishchenko, M. I., and Fu, Q.: Scattering and absorption property database for nonspherical ice particles in the near- through far-infrared spectral region, *Appl. Opt.*, 44, 5512–5523, 2005.
- Yang, P., Zhang, L., Hong, G., Nasiri, S. L., Baum, B. A., Huang, H. L., King, M. D., and Platnick, S.: Differences between collection 4 and 5 MODIS ice cloud optical/microphysical products and their impact on radiative forcing simulations, *IEEE Trans. Geosci. Remote Sens.*, 45, 2886–2899, 2007.
- Yang, P., Bi, L., Baum, B. A., Liou, K. N., Kattawar, G. W., Mishchenko, M. I., and Cole, B.: Spectrally consistent scattering, absorption, and polarization properties of atmospheric ice crystals at wavelengths from 0.2 to 100 μm , *J. Atmos. Sci.*, 70, 330–347, 2013.
- Yi, B., Yang, P., Baum, B. A., L'Ecuyer, T., Oreopoulos, L., Mlawer, E. J., Heymsfield, A. J., and Liou, K.-N.: Influence of ice particle surface roughening on the global cloud radiative effect, *J. Atmos. Sci.*, 70, 2794–2807, 2013.
- Zoll, Y.: Bestimmung des Flüssigwasserpfades aus Mikrowellenradiometer- und Wolkenkammermessungen, Master's thesis, Leibniz Institut für Meereswissenschaften IFM-GEOMAR, Kiel, Germany, 2008.
- Zoll, Y.: Bestimmung des Flüssigwasserpfades auf See mit Hilfe der passive Mikrowellenradiometrie, Ph.D. thesis, Christian-Albrechts-University of Kiel, 2012.

List of Symbols

α	rad or $^{\circ}$	Roll angle
$\alpha_{\lambda}^{\text{par}}$	km^{-1}	Particle extinction coefficient
β	rad or $^{\circ}$	Pitch angle
$\beta_{\lambda}^{\text{par}}$	$\text{km}^{-1} \text{sr}^{-1}$	Particle backscatter coefficient
θ	rad or $^{\circ}$	Atmospheric zenith angle
θ_0	rad or $^{\circ}$	Solar zenith angle
θ'_0	rad or $^{\circ}$	Ship solar zenith angle
ϑ	rad or $^{\circ}$	Scattering angle
λ	nm or μm	Wavelength
μ	1	Cosine of the zenith angle θ
μ_0	1	Cosine of the solar zenith angle θ_0
μ_i	1	Cosine of the incident zenith angle θ_i
ρ_w	g m^{-3}	Density of liquid water
σ	variable	Standard deviation
τ	1	Cloud optical thickness
τ_c	1	Total (cloud) optical thickness
τ_{ci}	1	Cirrus optical thickness
τ_{retr}	1	Retrieved cloud optical thickness
φ	rad or $^{\circ}$	Atmospheric azimuth angle
φ_0	rad or $^{\circ}$	Solar azimuth angle
φ_i	rad or $^{\circ}$	Azimuth angle, incident direction
$\tilde{\omega}$	1	Single-scattering albedo
$\tilde{\omega}'$	1	Delta-scaled single-scattering albedo
$\langle \tilde{\omega} \rangle$	1	Volumetric single-scattering albedo
Δ	rad or $^{\circ}$	Opening angle of radiance inlet
$\Delta\alpha$	rad or $^{\circ}$	Offset roll angle
$\Delta\beta$	rad or $^{\circ}$	Offset pitch angle
$\Delta\theta$	rad or $^{\circ}$	Horizontal misalignment
Λ	1	Truncation order
Φ_{λ}	W nm^{-1}	Spectral radiant energy flux
$d^2\Omega$	sr	Differential solid angle
$\langle b_{\text{ext}}(\lambda) \rangle$	m^{-1}	Volumetric extinction coefficient
$\langle b_{\text{sca}}(\lambda) \rangle$	m^{-1}	Volumetric scattering coefficient
d_a	m	Along-track footprint

d_c	m	Cross-track footprint
f_{tr}	1	Fraction of truncated energy
g	1	Asymmetry factor
g_{corr}	rad or $^\circ$	Horizontal alignment correction factor
h	rad or $^\circ$	Heading of the ship
h_0	rad or $^\circ$	Solar altitude
h_c	m	Cloud altitude
h_{tr}	1	Truncation function
l	cm	Distance between lamp and reflectance panel
l_0	cm	Certified distance between lamp and reflectance panel
n	1	Order of the Legendre polynomials and coefficients
\tilde{n}	1	Complex index of refraction
\tilde{n}_i	1	Imaginary part of index of refraction
\hat{n}	1	Surface orientation of d^2A
\hat{n}_\perp	1	Surface orientation of d^2A_\perp
$\langle p \rangle$	sr^{-1}	Volumetric phase function
p_τ	%	Percentage increase in τ -sensitivity
$p_{r_{\text{eff}}}$	%	Percentage increase in r_{eff} -sensitivity
r_{eff}	μm	Droplet effective radius
$r_{\text{eff, retr}}$	μm	Retrieved effective radius
s	1	Spectral slope
\hat{s}	1	Direction of propagation
t	s	Time
t_{int}	s	Integration time
v	m s^{-1}	Horizontal wind velocity
z	m	Geometrical thickness of a cloud
z_{base}	m	Cloud base height
z_{top}	m	Cloud top height
A	m^2	Particle cross section
d^2A	m^2	Infinitesimal area element
d^2A_\perp	m^2	Infinitesimal area element perpendicular to \hat{s}
$C_{\lambda, \text{P}}$	$\text{W m}^{-2} \text{nm}^{-1} \text{sr}^{-1}$	Spectral absolute calibration factor (Panel)
$C_{\lambda, \text{S}}$	$\text{W m}^{-2} \text{nm}^{-1} \text{sr}^{-1}$	Spectral absolute calibration factor (Sphere)
$C_{\lambda, \text{T}}$	$\text{W m}^{-2} \text{nm}^{-1} \text{sr}^{-1}$	Spectral transfer calibration factor
C_n	1	Legendre coefficients
C'_n	1	Delta-scaled Legendre coefficients
C_s	W m^{-2}	Solar cloud forcing
C_t	W m^{-2}	Terrestrial cloud forcing
C_{abs}	m^2	Absorption cross section
C_{ext}	m^2	Extinction cross section
C_{sca}	m^2	Scattering cross section
C'_{abs}	m^2	Delta-scaled absorption cross section
C'_{ext}	m^2	Delta-scaled extinction cross section

C'_{sca}	m^2	Delta-scaled scattering cross section
D	m	Particle diameter
D_n	1	Legendre coefficients of truncated function h_{tr}
E_{rad}	J	Radiant energy
F_{λ}	$\text{W m}^{-2} \text{nm}^{-1}$	Spectral irradiance
$F_{\lambda,\text{iso}}$	$\text{W m}^{-2} \text{nm}^{-1}$	Isotropic spectral irradiance
$F_{\lambda,\text{L}}$	$\text{W m}^{-2} \text{nm}^{-1}$	Spectral irradiance calibration lamp
F_{λ}^{\downarrow}	$\text{W m}^{-2} \text{nm}^{-1}$	Downward spectral irradiance
F_{λ}^{\uparrow}	$\text{W m}^{-2} \text{nm}^{-1}$	Upward spectral irradiance
G	1	Digital Signal
I_{λ}	$\text{W m}^{-2} \text{nm}^{-1} \text{sr}^{-1}$	Spectral radiance
I_{λ}^{\downarrow}	$\text{W m}^{-2} \text{nm}^{-1} \text{sr}^{-1}$	Downward (zenith) spectral radiance
I_{λ}^{\uparrow}	$\text{W m}^{-2} \text{nm}^{-1} \text{sr}^{-1}$	Upward spectral radiance
$I_{\lambda,\text{S}}$	$\text{W m}^{-2} \text{nm}^{-1} \text{sr}^{-1}$	Spectral radiance of integrating sphere
$I_{\lambda,\text{iso}}$	$\text{W m}^{-2} \text{nm}^{-1} \text{sr}^{-1}$	Isotropic spectral radiance
I_{diff}	$\text{W m}^{-2} \text{nm}^{-1} \text{sr}^{-1}$	Diffuse solar radiance
I_{dir}	$\text{W m}^{-2} \text{nm}^{-1} \text{sr}^{-1}$	Direct solar radiance
J_{diff}	$\text{W m}^{-2} \text{nm}^{-1} \text{sr}^{-1}$	Multiple-scattering term
J_{dir}	$\text{W m}^{-2} \text{nm}^{-1} \text{sr}^{-1}$	Single-scattering term
$\frac{dN}{d \log D}$	m^{-1}	Particle number size distribution
P_n	1	Legendre polynomials
P_{10}	variable	10th percentile
P_{25}	variable	25th percentile
P_{75}	variable	75th percentile
P_{90}	variable	90th percentile
R_{λ}	1	Spectral reflectivity
R_{P}	1	Panel reflectivity
S_0	$\text{W m}^{-2} \text{nm}^{-1}$	Extraterrestrial irradiance
S^{mol}	sr^{-1}	Molecular lidar ratio
S_{λ}^{par}	sr^{-1}	Particle lidar ratio
T_{λ}	1	Spectral transmissivity
V	m^3	Particle volume
\mathcal{P}	1	Scattering phase function
\mathcal{P}^*	1	Recalculated scattering phase function
\mathcal{P}_{tr}	1	Delta-scaled scattering phase function
\mathcal{T}	1	Transmissivity ratio
$BRDF$	sr^{-1}	Bidirectional reflectance distribution function
CRF	W m^{-2}	Cloud radiative forcing
Fr	1	Subadiabatic fraction
$FWHM$	nm	Full width at half maximum
IQR	variable	Interquartile range
IWC	g m^{-3}	Ice water content

<i>IWV</i>	kg m^{-2}	Integrated water vapor
<i>LWC</i>	g m^{-3}	Liquid Water Content
<i>LWP</i>	g m^{-2}	Liquid water path
<i>PR</i>	variable	Percentile range

List of Abbreviations

1D	one-dimensional
2-WL	two-wavelength
3D	three-dimensional
AERONET	AERosol RObotic NETwork
AOD	Aerosol Optical Depth
ARC	Arctic/Antarctic Research Classification
AWI	Alfred-Wegener-Institute for Polar and Marine Research
BK	Borosilikat-Kronglas (Borosilicate crown glass)
BT	Brightness Temperature
CCD	Charge-Couplet Device
CERES	Clouds and the Earth's Radiant Energy System
<i>CloudSat</i>	Cloud Satellite-based experiment
CM SAF	Climate Monitoring of Satellite Application Facility
CORAS	COmpact RAdiation measurement System
DIN	Deutsches Institut für Normung
DISORT	Discrete Ordinate Radiative Transfer Solver
DKD	Deutscher Kalibrierdienst (German Calibration Service)
DWD	Deutscher Wetterdienst (German Weather Service)
EM	Electromagnetic
ERBE	Earth Radiation Budget Experiment
GCM	General Circulation Model
GEOMAR	Helmholtz Centre for Ocean Research Kiel
HATPRO	Humidity And Temperature PROfiler
INS	Inertial navigation System
ISCCP	International Satellite Cloud Climatology Project
ISO	International Organization for Standardization
ITCZ	Inter Tropical Convergence Zone
<i>libRadtran</i>	library for radiative transfer
LiDAR	Light Detection And Ranging
LOWTRAN	Low-Resolution Spectral Transmission
LUT	Lookup Table
MAN	Maritime Aerosol Network
MBL	Marine Boundary Layer
MCS	Multi Channel Spectrometers
MINS	Marine Inertial Navigation System
MODIS	Moderate Resolution Imaging Spectroradiometer

NH	Northern Hemisphere
NIR	Near-infrared wavelength region (here, 700–3000 nm)
NIST	National Institute of Standards and Technology
NOAA	National Oceanic and Atmosphere Administration
OCEANET	Autonomous measurement platforms for material and energy exchange between ocean and atmosphere (artificial word)
PC	Personal Computer
PDA	Photo-Diode Array
PGS	Plane-Grating Spectrometers
Polly ^{XT}	Portable multi-wavelength Raman and polarization lidar (extended version)
RTE	Radiative Transfer Equation
RV	Research Vessel
SBDART	Santa Barbara DISORT Atmospheric Radiative Transfer
Sc	Stratocumulus
SCAWS	Scalable Automatic Weather Station
SDR	Solar Downward Radiation
SMART	Spectral Modular Airborne Radiation measurement sysTem
SOG	Speed Over Ground
SWIR	Spectrometer covering the wavelength region 900–2200 nm
TDR	Terrestrial Downward Radiation
TOA	Top Of Atmosphere
TROPOS	Institute for Tropospheric Research
USA	Ultrasonic-Anemometer
UTC	Coordinated Universal Time
UV	Ultra-Violet wavelength region (here, 100–380 nm)
VIS	Visible wavelength region (here, 380–700 nm)
VNIR	Spectrometer covering the wavelength region 290–1000 nm

List of Figures

1.1	Schematic illustration cloud regimes	2
1.2	Annual distribution of clouds	3
2.1	Geometry defining radiation quantities	9
2.2	Spectral single-scattering albedo of cloud particles	12
2.3	Scattering phase function of individual cloud particles	13
3.1	Cruise plots	18
3.2	Sahara dust	19
3.3	CORAS dust spectrum	20
3.4	CORAS basic setup	21
3.5	Optical inlets	22
3.6	Footprint geometry	24
3.7	Calibration setup for radiance	25
3.8	Absolute radiance calibration factors	26
3.9	Transfer radiance calibration factors	27
3.10	Geometry for roll/pitch/heading angles	30
3.11	OCEANET-Atmosphere container	31
3.12	HATRPO	33
3.13	Extinction coefficients over microwave region	35
4.1	Measured ship INS angles	38
4.2	Modeled zenith radiance	39
4.3	Modeled spectral transmissivity	40
4.4	LUTs 2-WL method	42
4.5	Spectral shape of basic optical properties	43
4.6	Normalized NIR transmissivity	44
4.7	LUT slope method	45
4.8	Percentage increase of ratio sensitivity	47
4.9	Ratio wavelengths	48
4.10	LUT multi-wavelength method	50
5.1	Cruise plots with case study coordinates	52
5.2	Retrieval results homogeneous liquid water cloud	53
5.3	<i>LWP</i> -comparison homogeneous liquid water cloud	55
5.4	<i>LWP</i> -comparison inhomogeneous liquid water cloud	56
5.5	Retrieval results scattered clouds	57
5.6	Observed transmissivity spectra of scattered clouds	58

5.7	Retrieval results cirrus	60
5.8	Sky images cirrus – Case study	61
5.9	Range corrected lidar plot	62
5.10	Cirrus optical thickness time series	62
5.11	Comparison slope and multi-wavelength retrieval	64
5.12	Comparison slope and multi-wavelength retrieval uncertainties	66
6.1	Cloud properties along the ship track	69
6.2	Meridional distribution of liquid water cloud properties – All cruises	71
6.3	Photos of cloud classes	72
6.4	Histogram of cloud classes	73
6.5	Histograms of cloud properties – all cruises	75
6.6	Histograms of cloud class properties – all cruises	75
6.7	Schematic illustration cloud step filter	77
6.8	Histograms of cloud step filtered cloud properties – all cruises	78
6.9	Histograms of cloud step filtered cloud class properties – all cruises	79
6.10	Sky images cirrus – Cloud analysis	80
6.11	Meridional distribution of cirrus cloud properties – CORAS	81
6.12	Histograms of cirrus cloud properties – all cruises	82
6.13	Geographic sections for comparison	83
6.14	Comparison meridional distribution – ANT-XXIX/1	85
6.15	Histograms of cloud properties from CORAS and MODIS	85
6.16	MODIS meridional monthly means of cloud properties	86
A.1	Cloud properties along the ship track – ANT-XXVII/4	94
A.2	Cloud properties along the ship track – ANT-XXVIII/5	95
A.3	Meridional distribution of liquid water cloud properties – ANT-XXVII/4	96
A.4	Meridional distribution of liquid water cloud properties – ANT-XXVIII/5	96
A.5	Meridional distribution of liquid water cloud properties – ANT-XXIX/1	97
A.6	Comparison meridional distribution – ANT-XXVII/4	97
A.7	Comparison meridional distribution – ANT-XXVIII/5	98
B.1	Histograms of cloud class properties – ANT-XXVII/4	99
B.2	Histograms of cloud class properties – ANT-XXVIII/5	100
B.3	Histograms of cloud class properties – ANT-XXIX/1	101

List of Tables

3.1	Cruise details	18
3.2	Noble-gas emission lines	24
3.3	Spectral measurement uncertainties	28
3.4	Sensor offset angles	31
4.1	Retrieval uncertainties 2-WL method	43
4.2	Retrieval uncertainties slope method	45
4.3	Retrieval uncertainties liquid water cloud	51
4.4	Retrieval uncertainties ice cloud	51
5.1	Comparison optical thickness retrieval CORAS-lidar	63
6.1	Cloud classification for liquid water clouds	72
6.2	Overview liquid water cloud data	73
6.3	Statistic liquid water clouds – all cruises	76
6.4	Statistic cloud step filtered liquid water clouds – all cruises	78
6.5	Overview cirrus cloud data	80
B.1	Statistic liquid water clouds – ANT-XXVII/4	100
B.2	Statistic liquid water clouds – ANT-XXVIII/5	101
B.3	Statistic liquid water clouds – ANT-XXIX/1	102

Acknowledgements

This work was performed at the Leibniz–Institute for Tropospheric Research in cooperation with the University of Leipzig. It was funded by the Leibniz–network as part of the OCEANET–project.

I would like to thank many people who have supported me during my PhD, it is with expertise or words of encouragement. First of all, I would like to thank my supervisor Manfred Wendisch for his continuous support, constitutive ideas and guidance during the last four years. Special thanks go to Andreas Macke who has given me the unique possibility to take part in three research cruises. My colleagues André Ehrlich, Frank Werner and Evi Jäkel which have contributed always helpful ideas and discussions and have supported me in technical issues. Thanks to Bernhard Pospichal for providing the HATPRO data. Besides all group members, I would like to thank my office colleagues, first Micha Wilsdorf and later Andi Foth and Frank Werner. Together we had lots of fun, so that even frustrating phases were always cheered up with laughs. Thanks to Fanny and Evi for proofreading.

Quite a big thank–you goes to the whole *Polarstern* crew and the colleagues of TROPOS during three OCEANET–cruises. I have got to know so many nice people who gave me with their natural help and exciting stories a feeling of home even if one is somewhere in the wide of the ocean. After a day of hard work, we really have earned our sunset beer.

Above all I would like to thank my family and my friends who supported me and have always encouraged me to keep on going my way. Even when things just didn't run as they should be, you have always listened to me and found the right words.

There are not enough words to thank my boyfriend Micha. He is always there for me. Without his help, this work wouldn't be what it is now.

Curriculum vitae

Name Marlen Brückner
Date of birth 5 July 1985
Place of birth Schlema, Sachsen
Citizenship German
Current address Graßdorfer Str. 13
04315 Leipzig, Germany
Email: marlen.brueckner (at) gmail.com

Education

08/1992 – 06/1996 Primary School Johann Wolfgang von Goethe, Zwönitz, Germany
07/1996 – 07/2004 High School Matthes–Enderlein–Gymnasium, Zwönitz, Germany
Degree: Abitur
10/2004 – 07/2010 Student of Meteorology at the University of Leipzig, Germany
Degree: Diploma
09/2010 – present PhD student at Leibniz–Institute for Tropospheric Research
Leipzig, Germany in cooperation with the University of Leipzig,
Germany

Employments

07/2009 – 08/2009 Student assistant of Prof. Dr. M. Wendisch
at University of Leipzig, Germany
07/2010 – 08/2010 Student assistant of Prof. Dr. M. Wendisch
at University of Leipzig, Germany
2010 – present Scientific employee at Leibniz–Institute for Tropospheric
Research Leipzig, Germany